Wave-supported gravity currents in continental shelves

Abbas Hooshmand Salemian

A dissertation
submitted in partial fulfillment of the
requirements for the degree of

Doctor of Philosophy

University of Washington

2015

Reading Committee:

Alexander R. Horner-Devine, Chair

Andrea S. Ogston

Christopher Chickadel

Program Authorized to Offer Degree:
Civil and Environmental Engineering

University of Washington

Abstract

Wave-supported gravity currents in continental shelves

Abbas Hooshmand Salemian

Chair of the Supervisory Committee:
Associate Professor Alexander R. Horner-Devine
Civil and Environmental Engineering

Wave-supported gravity currents (WSGC) are one of the most important processes causing cross shelf sediment transport. This dissertation studies the physics behind WSGC in continental shelves using experimental observations. An analytical model for predicting sediment transport due to these events on the shelf is proposed and validated.

First, the presence of the sediment bed and its effects on the flow structure is investigated in detail. The presence of sediment on the bed significantly alters the structure of the wave boundary layer relative to that observed in the absence of sediment, increasing the turbulent kinetic energy (TKE) by more than a factor of three at low wave orbital velocities and suppressing it at the highest velocities. In the low velocity regime, the flow is significantly influenced by the formation of ripples, which enhances the TKE and Reynolds stress and increases the wave boundary layer thickness. In the high velocity regime, the ripples are significantly smaller, the near-bed suspended sediment concentrations are significantly higher and density stratification due to suspended sediment concentration becomes important. In this regime, the TKE and Reynolds stress are lower in the sediment bed runs than in comparable runs with

no sediment. The transition between regimes appears to result from washout of the ripples and increased concentrations of fine sand suspended in the boundary layer, which increases the settling flux and stratification near the bed.

Second, experimental results for bulk, gradient and flux Richardson numbers are shown and proper scaling is proposed. It is shown that a bulk Richardson number using the maximum buoyancy frequency has a critical value of $\frac{1}{4}$, which is the value theoretically predicted. However, a bulk Richardson number using the average buoyancy frequency and a prescribed sediment concentration profile has a critical value of $Ri_{cr} \approx 0.03$. This value is nearly one order of magnitude smaller than the assumed critical number of $\frac{1}{4}$ from steady tidally driven currents.

Third, WSGCs are modeled using an analytical solution to the Navier-Stokes equations, and validated using experimental results. The velocity field is solved for zero slope condition and a down-slope velocity due to gravity is added for slope conditions. The final velocity profiles agrees very well with experimental down-slope velocities. The solution of the model is provided for laminar and turbulent conditions, and for exponential and a constant suspended sediment concentration profiles in the mud layer. Additionally, the criteria for laminar or turbulent regimes are proposed based on the Reynolds number of surface waves.

Finally, experimental results for suspended sediment concentration profiles, velocity, turbulence and wave boundary layer are compared to field observation and numerical simulations of WSGCs. The predicted down-slope velocity of a layer suspended and moved by surfaces waves is 1-2 orders of magnitude smaller than that observed in the field correlated with similar wave conditions.

TABLE OF CONTENTS

Page

List of Figures iii

List of Tables v

Chapter 1: Introduction 1
1.1 Motivation 1
1.2 Background 2
1.3 Overview 6

Chapter 2: Experimental setup and measurements 7
2.1 Wave flume 7
2.2 Instrumentation 9
2.3 Turbulence measurements and analysis 12

Chapter 3: Ripple effect and density stratification 16
3.1 Introduction 16
3.2 The structure of the wave boundary layer 17
3.3 Bed response and sediment profile 24
3.4 Turbulence in the wave boundary layer 32
3.5 Discussion 38
3.6 Summary and conclusions 52

Chapter 4: Richardson number 54
4.1 Introduction 54
4.2 Concentration and velocity profiles 55
4.3 Scaling for Richardson numbers 56
4.4 Vertical structure of Richardson numbers 60

4.5 Comparison and discussion 63

Chapter 5: Modeling wave-supported gravity currents 65
5.1 Theoretical development 66
5.2 Experiments 72
5.3 Experimental results 72
5.4 Comparison to models 78
5.5 Discussion 81
5.6 Summary and conclusions 86

Chapter 6: Comparison with previous studies 87
6.1 Introduction 87
6.2 Velocity profiles 87
6.3 Reynolds stress and shear velocity 90
6.4 Concentration profiles 92
6.5 Comparison of the current models 95
6.6 Conclusions 98

Chapter 7: Summary and Outlook 100
7.1 Summary 100
7.2 Outlook 102

Bibliography 103

LIST OF FIGURES

Figure Number		Page
2.1	schematic of wave-sediment U-tube tank.	8
3.1	Velocity profile at maximum velocity phase.	18
3.2	Wave boundary layer growth.	19
3.3	Wave boundary layer height (δ) for RW and SB experiments.	21
3.4	Phase lead and Velocity defect for RW and SB experiments.	23
3.5	Ripple steepness versus non-dimensional orbital diameter for sediment bed experiments.	26
3.6	Variation of ripple steepness with Reynolds number.	27
3.7	Suspended sediment concentration profiles for SX experiments	29
3.8	High concentration mud-layer (a) thickness, h (b) near-bed concentration, C_a, and (c) concentration gradient for SB experiments.	31
3.9	Reynolds stress pcolor for a RW experiment.	33
3.10	Reynolds stress for the rough wall (left panels) and the sediment bed (right panels) runs.	35
3.11	Comparison of shear velocity for rough wall (gray) and sediment bed (black) runs.	37
3.12	Average TKE and production within the WBL for RW and SB experiments.	39
3.13	Schematic for ripple steepness, buoyancy and average turbulent kinetic energy underneath the wave boundary layer.	43
3.14	The effects of ripples, stratification and sand fraction on turbulence	46
4.1	Parameter M for SB experiments.	58
4.2	Vertical structure of Richardson numbers.	62
5.1	SSC profiles for four experiments	74
5.2	u_g, SSC & Reynolds stress profiles	76
5.3	Average Reynolds stress, SSC & u_g in the mud layer	77

5.4 Net transport velocity profile in the mud layer 79
5.5 Average u_g in the lutocline for model and experiments 80
5.6 Non-dimensionalized across shelf velocity for different slopes 81
5.7 Eddy viscosity models comparison 83
5.8 Schematic for wave down slope velocity (laminar and turbulent) . . . 85

6.1 Non-dimensionalized velocity profiles 89
6.2 Field and experiments across shelf velocity 90
6.3 SSC profiles from ABS data in Waipaoa River Shelf in New Zealand . 94
6.4 SSC profiles for this study and field 95
6.5 Contours for u_g for different C_D and Ri_b 98

LIST OF TABLES

Table Number Page

2.1 Rough wall experiments parameters 9
2.2 Sediment bed experiments parameters 10
5.1 Experiments parameters 73
6.1 Shear velocity from experiments and the field 92

ACKNOWLEDGMENTS

Firstly, I'd like to thank my advisor, Alexander Horner-Devine. I have been amazingly fortunate to have an advisor who gave me the freedom to explore on my own, and at the same time the guidance to recover when my steps faltered. Alex's patience and support helped me overcome many crisis situations and finish this dissertation and his advice and enthusiasm for science provided me with the motivation to complete this dissertation. I could not have possibly imagined having a better advisor and mentor for my graduate study.

My committee members Chris Chickadel, Alexander Horner-Devine, Charles Nittrouer, Andrea Ogston and James Riley provided excellent insight and commentary on my approach and results.

I've appreciated the support from the other graduate students and postdocs from the Environmental Fluid Mechanics (EFM) group at UW through years. Many thanks to Maggie Averner, Chris Bassett, Roxanne Carini, Dan Nowacki, Mike Schwendeman, Stefan Talke and Seth Zippel. I appreciate the help I received from Adam Price who was involved in the project the first few months I was here. Special thanks to J.Paul Rinehimer, the encyclopedia of EFM group, who has been always the person to go to for questions about Matlab, LaTeX, numerical modeling, math questions and purely random things such as the latest report on Iran's income on exporting pistachio. Special thanks to my lab mates for putting up with me and trying their best to

understand my accent : Maggie McKeon, Anthony Poggioli and Yeping Yuan.

Im also grateful for the friendships I've made outside of the lab. Amir Seifi and Mohsen Sharifani have helped to keep me sane, and remember that there is life outside of science. Special thanks to Brian Crosier, Shamai Larsen, Chris Mac, Irena McQuarrie and Jason McWalter who ensured I spent enough time running barefoot and drank sufficient amount of Kombucha.

None of the experimental work could have been accomplished without support of Jeffery Parsons in letting us use his experimental facility. I'd like to thank Jim Thomson for lending me his measuring instruments through the course of my graduate studies and helping me out in installing them. I'd like to thank Tor BJorklund, Randy Fabro and Rex Johnson for building the wave tank in the first place, moving it to Harris Lab and helping with tank maintenance during the project.

During the course of my study I was supported by the National Science Foundation grant OCE-000488762, for which I am very grateful.

The support of my parents, Javad and Lagha Hooshmand, has been instrumental in my success throughout my life. I'd especially like to thank my brothers and sister, Nader, Amir and Nahid Hooshmand who supported me from several thousands miles away.

DEDICATION

To my parents, who laid the foundation for my passion for math and science.

Chapter 1

INTRODUCTION[1]

1.1 Motivation

Wave-supported gravity currents (WSGC) are considered to be one of the primary mechanisms for cross-shelf sediment transport on continental shelves (Wright and Friedrichs, 2006). These currents are formed as the surface waves penetrate to the shelf bottom in shallow regions of continental shelves. The shear stress applied on the sediment bed suspends the unconsolidated sediment particles and keeps them in suspension while there is enough turbulence. Many field observations show the importance of these events (Ogston et al., 2000; Traykovski et al., 2000) and a number of models have been developed based on available field data (Wright et al., 2001; Scully et al., 2002; Traykovski et al., 2007; Falcini et al., 2012). However, field observations generally cannot resolve the structure of WSGCs in sufficient detail to fully describe their dynamics or test model assumptions. On the other hands, numerical models can resolve the structure of these currents in great details (e.g. Colney et al., 2008; Ozdemir et al., 2010a).

Laboratory experiments can bridge between field observations and numerical models and give the appropriate framework for both of them. There have been several experimental works on WSGCs that have investigated velocity, turbulence and suspended sediment concentration (SSC) in these currents (e.g. Lamb et al., 2004; Lamb and Parsons, 2005; Liang et al., 2007; Yan et al., 2010). However, there is no experi-

mental work on the effects of slope on these currents. A complete experimental data set with detailed measurements of turbulence, velocity and SSC with different slopes will be useful to evaluate numerical and analytical models that are currently used for predicting WSGCs

1.2 Background

Rivers carry large volumes of terrestrially derived sediments to the coast and discharge them onto the continental shelf (Milliman and Meade, 1983), where they are dispersed by shelf processes (Nittrouer and Wright, 1994; Wheatcroft et al., 2007). These processes determine how sediment is redistributed on the shelf (Wright et al., 1997, 1999, 2001) and whether it is transported off the shelf into the abyssal ocean. This latter outcome is of particular importance because it represents a flux of sediment, carbon and nutrients out of the shelf system where it is no longer available to the coastal ecosystem.

Once they have been discharged into shelf waters, river-borne sediment may settle near the river mouth or further (Geyer et al., 2000; McPhee-Shaw et al., 2007; Walsh et al., 2004). The sediment deposition depends on the ratio of sediment to freshwater discharge (Wright and Friedrichs, 2006), flocculation (Safak et al., 2013) and other processes such as convective instabilities due to particle settling in the plume (Parsons et al., 2001) that affect their removal from the plume. Once they have been deposited on the shelf, they may be moved across the shelf as turbidity currents if the shelf is steep (Hamblin and Walker, 1979; Ma et al., 2008). However, most shelves are not sufficiently steep to support seaward transport of sediment due to gravity alone (Wright and Friedrichs, 2006). On gently sloping shelves additional shear from shelf currents or surface waves is required to generate sufficient sediment suspension and

maintain cross-shelf sediment transport. This study focuses solely on wave-generated suspensions.

Surface waves can generate significant bottom stresses on the shelf, though the stresses are strongest in shallower regions and only felt in deeper regions in storm conditions. When wave action and sediment supply are sufficient, this process generates thin, $\mathcal{O}(10\,\mathrm{cm})$, high concentration, $\mathcal{O}(50\,\mathrm{g\,l^{-1}})$ sediment layers that move downslope across the shelf due to gravity and are referred to as WSGC (Wright and Friedrichs, 2006). WSGCs have been observed on continental shelves near many river mouths, such as the Eel River (Ogston et al., 2000; Traykovski et al., 2000), Waiapu River (Ma et al., 2008), Po River (Traykovski et al., 2007), Atchafalaya River (Jaramillo et al., 2009) and Waipaoa River (Hale et al., 2014). WSGCs can transport sediment seaward until the shelf is so deep that the waves do not penetrate to the bottom and shear stress becomes small. At this point, the current may continue if the shelf is sufficiently steep, or it will die out and the sediment will be deposited (Traykovski et al., 2000; Wright and Friedrichs, 2006).

In the late 1990s, several field observations from the STRATAFORM program played a major role in improving our understanding of sediment transport across continental shelves (Nittrouer, 1999; Ogston et al., 2000; Geyer et al., 2000). Observations from the Eel River margin emphasized the important role of surface waves in cross-shelf sediment flux, and showed that a few significant storm events contributed most of the flux (Ogston et al., 2000; Puig et al., 2003). Traykovski et al. (2000) examined the velocity and sediment concentration profiles during a number of wave-induced transport events, showing that fluid mud is trapped in a thin layer whose thickness is similar to the wave boundary layer. Although velocity measurements were not possi-

ble within the mud layer, they observed enhancement of the velocity 0.5 meters above the bed (mab) relative to 1 mab and 2 mab during at least one major wave resuspension event and concluded that this is evidence of downslope gravitational transport. Based on the expected wave penetration, bottom slope and depth, Traykovski et al. (2000) concluded that this mud layer loses energy and is deposited at a depth of $90 - 110$ m. A series of models have been developed to predict the cross-shelf flux of sediment in WSGCs, primarily based on a linearized form of the Chezy equation (Wright et al., 2001; Scully et al., 2002; Traykovski et al., 2007). Wright et al. (2001) and Scully et al. (2002) relate sediment concentration to wave stress assuming a critical value of the bulk Richardson number Ri_b of 0.25. However, estimates from prior laboratory experiments find that Ri_b is approximately an order of magnitude smaller than this assumed value (Lamb et al., 2004), motivating a clearer understanding of the underlying dynamics in these flows.

A number of studies have used high resolution numerical models to better understand the dynamics of wave-generated high concentration mud layers and to address the measurement limitations in the field (Hsu et al., 2009; Ozdemir et al., 2010a, 2011). In agreement with the laboratory results, Hsu et al. (2009) found that Ri_b is smaller than 0.25, due to either a limited supply of unconsolidated fine sediment or a structural difference between tidal currents and wave-driven mud flows. Later, Ozdemir et al. (2010b) used a numerical simulation in an Eulerian-Eulerian framework for low concentration settings and concluded that fine sediments are well-mixed in all phases of the wave, though turbulence is not modulated for such dilute concentration settings. Ozdemir et al. (2010a) used the same model for a wide range of suspended sediment concentration (SSC) profiles with fixed wave orbital velocity. They observed

a number of different regimes, including: no turbulence for very dilute conditions, formation of a lutocline and finally, complete laminarization due to particle-induced stable density stratification for high sediment concentrations. Ozdemir et al. (2011) later investigated the effects of settling velocities, while maintaining constant SSC using the same numerical model. They concluded that larger settling velocities can decrease the thickness of the high concentration mud layer and eventually cause the flow to laminarize.

In a series of previous laboratory experiments Lamb et al. (2004), investigated the dynamics of high concentration sediment suspensions with zero slope. Their study (see also Lamb and Parsons, 2005; Liang et al., 2007; Yan et al., 2010) consisted of two series of experiments; one with a rough bed without sediment and one with a sediment bed with mostly silt-size particles, representative of a continental shelf seafloor. They found that sediment reduced the thickness of the wave boundary layers substantially, but that the flows were still able to support high-density suspensions thicker than the boundary layer due to upward transport of turbulent energy from this thin region. They also suggest that the sediment concentration in the high concentration layer is sufficient to generate density stratification that may influence the flow dynamics. In their experiments, Lamb et al. (2004) and Lamb and Parsons (2005) show that waves increase the sand fraction of the near-surface bed layer through winnowing. The coarsened bed surface resulted in significant bedload and the generation of ripples.

Such laboratory investigations of wave-supported gravity currents can bridge between simplified models based on field observations and very detailed numerical models that have not been verified with field measurements. Numerical models still struggle to capture some of the physical processes that are likely to be important in WSGCs

(Hsu et al., 2009). In particular, we expect that the range of particle sizes observed in naturally occurring flows contribute to the dynamics of the currents, through the formation of ripples, the generation of density stratification, and the possible interaction of these processes. Numerous studies with sand beds show that turbulence is enhanced due to ripples (Doering and Baryla, 2002; Hare et al., 2014). On the other hand, work in exclusively muddy flows shows that suspended sediment can suppress turbulence (Winterwerp, 2006).

1.3 Overview

This dissertation shows results of new laboratory experiments that investigate the generation and turbulent structure of high-density sediment suspensions over a sediment bed similar to those observed on the continental shelf. In this work, it is shown how ripples and stratification affect the turbulence level in the wave boundary layer and determine the wave conditions in which each of them is dominant. The experiments use new instrumentation that resolves the temporal and vertical structure of the sediment and turbulent velocity fields in sufficient detail to determine the underlying physical relationships in WSGCs. Moreover, an analytical model is proposed and validated against experimental results for predicting sediment transport due to wave-supported gravity currents. Finally, these experimental results are compared to field observations of WSGCs.

Chapter 2

EXPERIMENTAL SETUP AND MEASUREMENTS

The present experiments were carried out in a purpose-built, wave-sediment U-tube tank equipped to make high resolution measurements of velocity, turbulence and suspended sediment concentration. The experimental facility is the same as the facility used by Lamb et al. (2004), with two important modifications. First, it has been modified to extend the upper range of wave periods from 8 s to 12 s in order to better simulate waves typically observed on the continental shelf. Second, we use new instrumentation for measuring velocity and sediment concentration that makes high frequency profile measurements, rather than point measurements, enabling us to better resolve the turbulent wave boundary layer structure.

In order to investigate the relationship between turbulence and suspended sediment in WSGCs we carry out two parallel sets of experiments, one with an active sediment bed and one with a roughened bottom and no sediment. We compare the structure of the turbulence and sediment concentration profiles in the wave-boundary layer in both cases.

2.1 Wave flume

The U-tube wave facility has a sealed 5 m long, 1 m high and 0.2 m wide test section (Figure 2.1). Approximately sinusoidal oscillatory flows in the test section are driven

[1]Portions of this chapter and chapter 3 submitted as: Hooshmand, Abbas, Alexander R. Horner_Devine, and Michael P. Lamb. Structure of turbulence and sediment stratification in wave supported mud layers. Journal of Geophysical Research: Oceans 120.4 (2015): 2430-2448

by a moving piston that produces waves with periods of $4 - 12\,\mathrm{s}$ and orbital velocities of $20 - 70\,\mathrm{cm\,s^{-1}}$. Rather than wave orbitals, the U-tube facility produces purely horizontal oscillatory mean flows, characteristic of the one-dimensional velocity fields observed near the seabed on the continental shelf due to surface gravity waves. The top and side walls of the test section are made of smooth plexiglass.

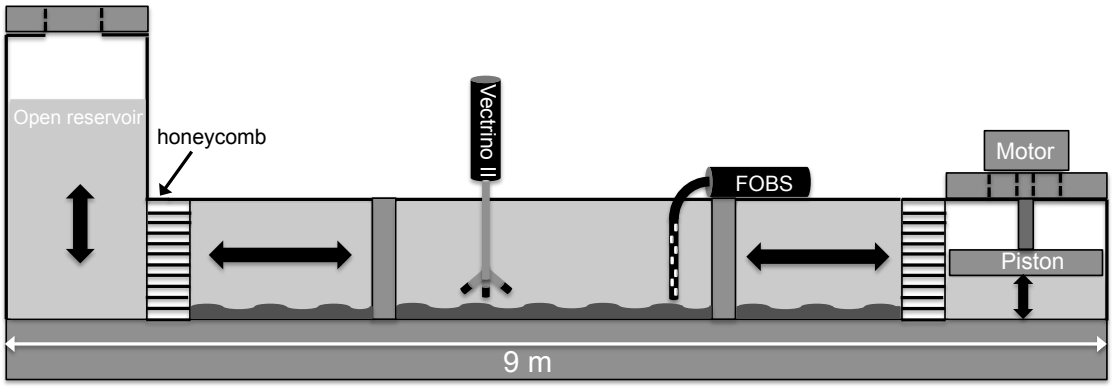

Figure 2.1 Side-view schematic of wave-sediment U-tube tank. Motion is driven by the piston on the right and return flow from the open reservoir on the left, generating horizontal oscillatory motion in the 0.2 m wide test section.

2.1.1 Rough wall experiments

For the rough wall (RW) experiments, sand particles ($D_{50} = 750\,\mu m$) were glued to a false floor, which was placed on the bottom of the tank. Clear tap water was used in these experiments, to characterize the turbulent wave boundary layer flow in the absence of sediment. Overall, 20 experiments were performed in this mode, which included a range of wave periods ($5 < T < 12\,\mathrm{s}$) and wave orbital velocities ($20 < U_{orb} < 65\,\mathrm{cm\,s^{-1}}$). Table 2.1 shows a summary of the rough wall experiments.

Table 2.1 Rough wall experiments parameters

	Rough wall experiments																			
Test #	1	2	3	4	5	6	7	8	9	10	11	12	13	14	15	16	17	18	19	20
$U_{orb}(\mathrm{cm\,s^{-1}})$	35	16	26	30	38	16	19	19	27	35	43	53	19	27	35	44	33	45	57	68
T(s)	4.6	9.4	5.9	5.2	4.3	10	7.8	11.6	7.9	6.3	5.2	4.3	14.6	10	7.7	6.3	10.1	7.4	5.9	5.1
$u_*(\mathrm{cm\,s^{-1}})$	0.6	0.2	0.4	0.9	0.9	0.2	0.3	0.2	0.4	0.7	1	1.3	0.2	0.4	0.8	1.3	0.8	1.1	1.4	1.7
δ(cm)	1.1	0.7	1	0.9	1.1	0.6	0.6	1.3	1.5	1.5	1.5	1.4	1.5	1.5	1.6	1.9	2.4	2.2	2.2	2.2

2.1.2 Sediment bed experiments

For the sediment bed (SB) experiments, the false floor was replaced with a 10cm thick sediment bed. The sediment bed (Sil-co-Sil 106 by U.S. silica) is primarily silt, with clay:silt:sand fractions of 0.10, 0.77 and 0.13, respectively. The sand fraction consists primarily of very fine sand. This distribution is similar to field observations from (Ogston et al., 2000), who report size fractions of 0.85 clay and silt and 0.15 sand on the northern California continental shelf. A layer of new sediment was added for each run, and the experiment was performed two days later to ensure that the degree of consolidation was the same for all experiments. The wave settings covered the same ranges as rough wall experiments. Table 2.2 shows a summary of the sediment bed experiments.

2.2 Instrumentation

Measurements of the vertical profile of velocity, turbulence and sediment concentration were made using instrumentation placed in the middle of the test section.

Table 2.2 Sediment bed experiments parameters

	Sediment bed experiments																						
Test #	1	2	3	4	5	6	7	8	9	10	11	12	13	14	15	16	17	18	19	20	21	22	23
$U_{orb}(\frac{\text{cm}}{\text{s}})$	37	34	42	57	46	26	30	45	29	42	54	40	15	19	25	32	20	35	23	39	18	26	31
T(s)	8.9	9.6	7.7	5.8	7.1	8.2	7.8	5.2	10.8	7.7	5.9	7.8	10.5	8.6	6.6	5.1	7.9	4.8	7.1	4.4	14.2	9.3	8
$u_*(\frac{\text{cm}}{\text{s}})$	1.1	1.1	1.1	0.8	1.4	1	1.1	0.9	1.2	1.2	0.8	1.3	0.6	0.8	1	1.4	0.8	1.2	1.3	1.2	0.9	1.3	1.6
δ(cm)	3.3	3.3	2.9	0.9	3.2	2.5	3	3.4	3.5	3.1	2.7	2.5	1.7	3.6	3.6	1.5	3.6	3.6	3.2	4.6	3	3.4	3.6
Test #	24	25	26	27	28	29	30	31	32	33	34	35	36	37	38	39	40	41	42	43	44	45	46
$U_{orb}(\frac{\text{cm}}{\text{s}})$	35	39	30	23	34	40	44	50	47	51	26	27	26	25	24	25	24	32	33	32	31	42	42
T(s)	7.3	6.2	10.4	13.7	9.3	7.9	7.1	6.2	6.4	5.6	11.6	11.5	11.6	12.5	12.5	12.4	12.6	9.9	9.8	9.8	9.7	7.7	7.6
$u_*(\frac{\text{cm}}{\text{s}})$	1.2	1.3	1.2	0.8	1.3	1.1	1.4	1.2	1.4	1.4	1.1	1.6	0.9	0.8	0.9	0.8	1.1	1.1	1.1	1	1.2	1	1.1
δ(cm)	2.5	3.3	3.2	4.8	3.3	3.1	2.5	2.8	2.8	2.7	3.3	3.9	4.2	3.4	4.2	5.2	4.6	3.4	2.8	3.4	2.5	3.3	2.8
Test #	47	48	49	50	51	52	53	54	55	56	57	58	59	60	61	62	63	64	65	66	67	68	
$U_{orb}(\frac{\text{cm}}{\text{s}})$	40	29	29	29	29	37	37	37	37	37	36	35	36	36	37	36	36	41	44	44	45	44	
T(s)	7.8	10.8	10.8	10.9	10.8	8.4	8.4	8.4	8.4	8.4	8.5	8.5	8.4	8.4	8.4	8.5	8.5	7.4	6.6	6.6	6.6	6.7	
$u_*(\frac{\text{cm}}{\text{s}})$	1.1	1	1.1	1	1.2	1.2	0.9	1.1	1.1	1.5	1.8	1.1	1	1	1.1	1	1.2	1.3	1.1	0.9	1	0.8	
δ(cm)	3.7	3.4	3.1	2.8	3.3	2.5	2.5	2.3	2.5	2.1	2.6	3	2.8	2.4	2.3	2.2	2.6	2.9	1.5	1.5	1.9	2.8	

2.2.1 Velocity

Two acoustics doppler velocimeters (ADV) were used in our experiments. The velocities near the bottom were measured with a profiling ADV (Nortek Vectrino II) which measures three components of velocity (U, V, W) with a resolution of 1 mm and sampling rate up of 100 Hz. The Vectrino II has a sampling profile of 35 mm (35 bins); however, we use only the middle bins (11-30) due to higher noise near the top and bottom of the ADV profile that affect the turbulence measurements. The other ADV (Nortek Vectrino) was positioned 70 cm from the bottom in the free-stream flow and synced with the Vectrino II in order to detect wave velocity phasing independently of the boundary layer measurements. In each experiment six vertically stacked profiles were acquired with the Vectrino II. These were combined using the wave phase information from the Vectrino in order to generate a 8 cm velocity profile $u(z, t)$.

2.2.2 Sediment concentration measurement

The concentration measurement was performed with a fiber optic backscattering sensor (FOBS) and an 11-port vertical sediment siphon rake. The FOBS has 20 bins extending from the bed to 50 cm above the bed, with 1 cm spacing in the lowermost 10 cm and coarser spacing above. The sampling volume is a function of concentration and particle size distribution and varies depending on the SSC in the mud layer. A mixing tank calibration using Sil-co-Sil 106 showed that the FOBS response was linear for concentrations below $80\,\mathrm{g\,l^{-1}}$, which represents the upper limit of concentrations observed in our experiments based on the sediment siphon data. However, since optical backscatter is very sensitive to the particle size of the suspended sediments (Downing, 2006), we also made siphon measurements for many of the experiments.

Water and sediment samples were acquired over a two minute period following the procedure outlined in Lamb et al. (2004) and Hooshmand et al. (2015). The siphon data provided a redundant measure of the time-averaged concentration profile and were used to calibrate the FOBS output.

2.3 Turbulence measurements and analysis

We used the free-stream ADV as a reference to calculate phase-averaged parameters. These parameters were averaged over $20 - 50$ wave periods giving us phase averaged data with $\frac{2\pi}{400}$ resolution on the wave period and 1 mm vertical resolution. Phase averaging was done for all parameters, including velocity, production and Reynolds stress. Wave orbital velocity was calculated according to $U_{orb} = \sqrt{2}U_{rms}$ in which U_{rms} is the root mean square of the velocity +10 cm from the bottom. Wave period (T) was calculated using the average value of time differences of occurrence of zero velocities in the velocity time-series. Orbital diameter is then defined as the ratio of wave orbital velocity and wave orbital frequency ($\omega = \frac{2\pi}{T}$)

There are two primary independent parameters in our experiments, wave orbital velocity and wave period. Two Reynolds numbers are used to group these two parameters in wave-supported gravity currents, one based on the wave excursion amplitude and the other based on the Stokes boundary layer thickness (Ozdemir et al., 2010a). In this study, we use the latter Reynolds number as our independent parameter since it provides a more convenient length-scale for our experiments:

$$Re_{\Delta} = \frac{U_{orb}\tilde{\Delta}}{\nu} \tag{2.1}$$

Here, $\tilde{\Delta}$ is the Stokes boundary layer thickness defined as $\tilde{\Delta} = \sqrt{2\nu/\omega}$ and ν is the viscosity.

2.3.1 ADV post-processing

The raw ADV results were quality controlled and the ADV data was despiked using the three-dimensional phase space algorithm developed by Goring and Nikora (2002) and Mori et al. (2007). The along-channel, transverse and vertical velocities were decomposed into wave components ($\overline{u}\,\overline{v}\,\overline{w}$) and turbulent fluctuation components ($u'\,v'\,w'$). The vertical and transverse wave components ($\overline{v}\,\overline{w}$) may be non-zero in the presence of ripples with cross-channel variability. The wave components were separated from the turbulent fluctuation components using a tenth-order Butterworth filter with a cutoff frequency of 1.25 Hz following Lamb et al. (2004).

2.3.2 Turbulent parameters

The variability and dynamics of the turbulence in the wave-boundary layer are quantified in terms of the Turbulent Kinetic Energy per unit mass (TKE):

$$\mathrm{TKE} = \frac{1}{2}(\overline{u'^2} + \overline{v'^2} + \overline{w'^2}). \tag{2.2}$$

and the TKE evolution equation

$$\mathrm{D(TKE)}/\mathrm{D}t = P + T - B - \epsilon. \tag{2.3}$$

Equation 2.3 shows that the rate of change of TKE, $\mathrm{D}(TKE)/\mathrm{D}t$, is determined by the rates of TKE production (P), dissipation (ϵ), transport (T), and the buoyancy flux (B). For uniform steady unstratified currents, $\mathrm{D}(TKE)/\mathrm{D}t$ and B are zero. The integrated TKE transport is often assumed to be negligible, resulting in a balance between P and ϵ. However, there is a phase difference between P and ϵ and these terms do not necessarily balance instantaneously. In fact, the rate of change of TKE

can vary by up to 50% of P in low Re_Δ flows due to intermittency in turbulence and transitional flow (Ozdemir et al., 2014). Furthermore, Lamb et al. (2004) suggests that the transport term may be important; it may help to maintain elevated suspended sediment concentration above the defined wave boundary layer. The profiling ADV presents an opportunity to estimate key components of the transport term directly. However, the measurements of the fluctuating velocity gradient were too noisy to reliably resolve this term in our experiments.

We account for noise in the ADV measurements by taking advantage of the redundant vertical velocity measurement on the Vectrino instruments. The noise is much lower in the vertical components compared with the horizontal components due to the geometry of the instrument head. Because of the fourth receiver, the Vectrino II gives us two independent measurements of vertical velocity. We use co-spectral analysis of these two measurements to find the variance of the noise in the vertical component and the ADV transformation matrix to determine the noise in the horizontal components. The noise is then subtracted from variance of fluctuation velocity in each component to get the noise free estimates of $(u'\,v'\,w')$ and TKE (Hurther and Lemmin, 2001).

The Reynolds stress per unit mass $u'w'$ was calculated from the ADV measurements of u' and w', and phased averaged as described above. The Reynolds stress estimate is inherently noise free, assuming that the noise in the horizontal and vertical velocity components are uncorrelated (Hurther and Lemmin, 2001).

The shear velocity $u_* = (\tau_o/\rho)^{1/2}$ (τ_o is the shear stress at the bed) is often estimated based on the law of the wall, $\frac{\partial u}{\partial z} = \frac{u_*}{\kappa z}$. However, applicability of the law of the wall is limited to flows in which the roughness length scale (z_0) is small relative to

the wave boundary layer thickness (δ), i.e. $z_0 << z << \delta$ (Grant and Madsen, 1986) and in which density stratification is minimal. Neither of these criteria are satisfied in the present experiments since the flow was not fully turbulent (Ozdemir et al., 2014). For this reason, we estimate shear velocity based on the Reynolds stress averaged over the wave boundary layer and wave period.

TKE production is calculated using the measured Reynolds stress and vertical velocity gradient according to

$$P \simeq -\overline{u'w'}\frac{\partial U}{\partial z} \tag{2.4}$$

where U is the phase-averaged horizontal velocity.

Chapter 3

RIPPLE EFFECT AND DENSITY STRATIFICATION

3.1 Introduction

Continental shelves typically have mostly mud beds (Sternberg and Cacchione, 1996; Wright et al., 1997; Kineke et al., 2000; Walsh et al., 2004) but may include a sand component (0-10%), and both ripples and dense suspensions have been observed (Ogston and Sternberg, 1999; Traykovski et al., 2007). The competing effects of ripples and density stratification can enhance or suppress turbulence in the water column. However, it is not known under what conditions bedforms and density stratification will be important in the sediment mixtures typical of WSGCs, whether they will co-exist and under which conditions each will dominate.

The formation of ripples due to waves can enhance the turbulence near the sediment bed and maintain the sediment particles in suspension. In addition, ripples can influence the velocity field and increase the wave boundary layer height (Doering and Baryla, 2002). On the other hand, density stratification associated with high near-bed sediment concentrations damps the turbulence in highly stratified flows (Winterwerp, 2006) and may decrease the wave boundary layer heights. As a result, it is important to know that formation of ripples and density stratification due to formation of mud layers occur in which wave conditions. In addition, it will be useful to know whether

[1]Parts of this chapter was published as: Hooshmand, Abbas, Alexander R. Horner_Devine, and Michael P. Lamb. Structure of turbulence and sediment stratification in wave supported mud layers. Journal of Geophysical Research: Oceans 120.4 (2015): 2430-2448

ripples and density stratified flows can coexist and what happens to the turbulence field in that condition.

In this chapter, high resolution measurements of velocity, turbulence and suspended sediment concentration in a wave flume is shown in order to describe the physical processes that control the formation of wave-supported high concentration mud layers and associated gravitational transport on the continental shelf. These laboratory experiments simulate the conditions under which wave-supported mud flows occur on the continental shelf. The effects of ripple and density stratification on velocity, turbulence structure inside and outside of the wave boundary layer and suspended sediment concentration is investigated in detail. Finally, the condition where ripples and density stratification have significance is determined from our experimental results.

3.2 The structure of the wave boundary layer

In this section we investigate the overall structure of the wave boundary layer, and the impact of suspended sediment on its structure.

3.2.1 Velocity profiles and wave boundary layers

The vertical structure of the velocity profiles in oscillatory flows consists of three distinctive zones: the wave boundary layer zone ($\partial u/\partial z > 0$), the overshoot zone ($\partial u/\partial z < 0$)and the free stream zone ($\partial u/\partial z \approx 0$) (Nielsen, 1992; Lamb et al., 2004). These three zones are shown for the velocity profile during the maximum velocity phase in Figure 3.1. The wave boundary layer (δ) is the point on the border of the wave boundary layer and overshoot zones where the maximum velocity occurs.

The three zones are maintained through each wave phase, but the structure and

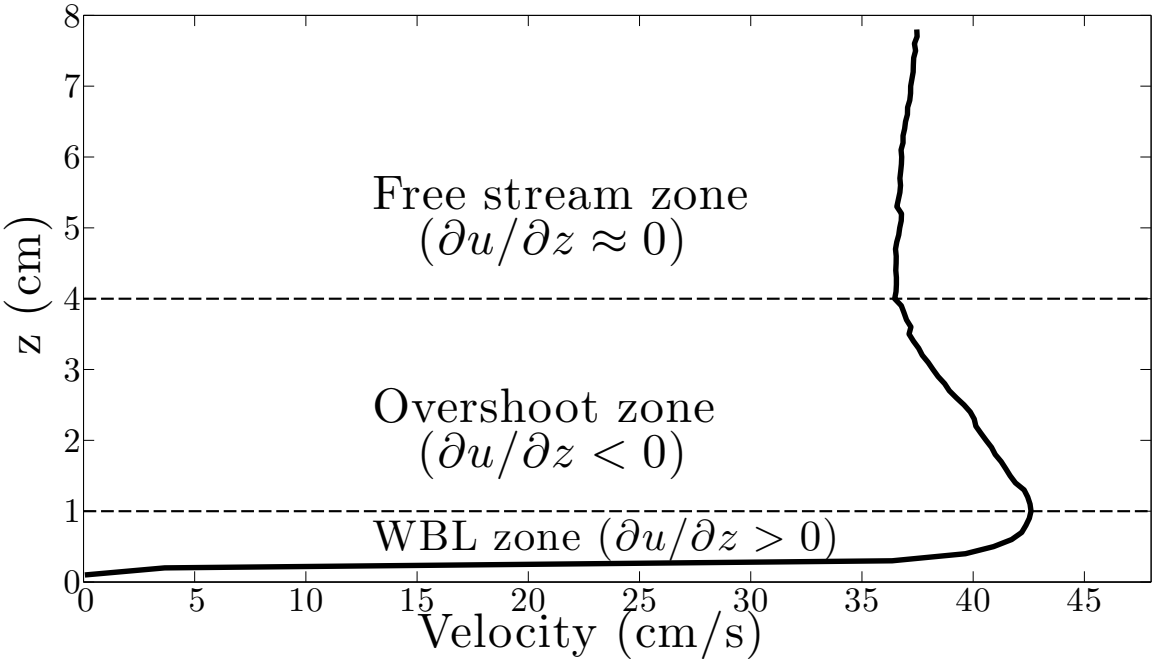

Figure 3.1 Velocity profile at maximum velocity phase for a rough wall experiment with $U_{orb} = 45$ cm/s and $T = 7.4$ s. The velocity profile contains three regions : wave boundary layer, overshoot and free stream.

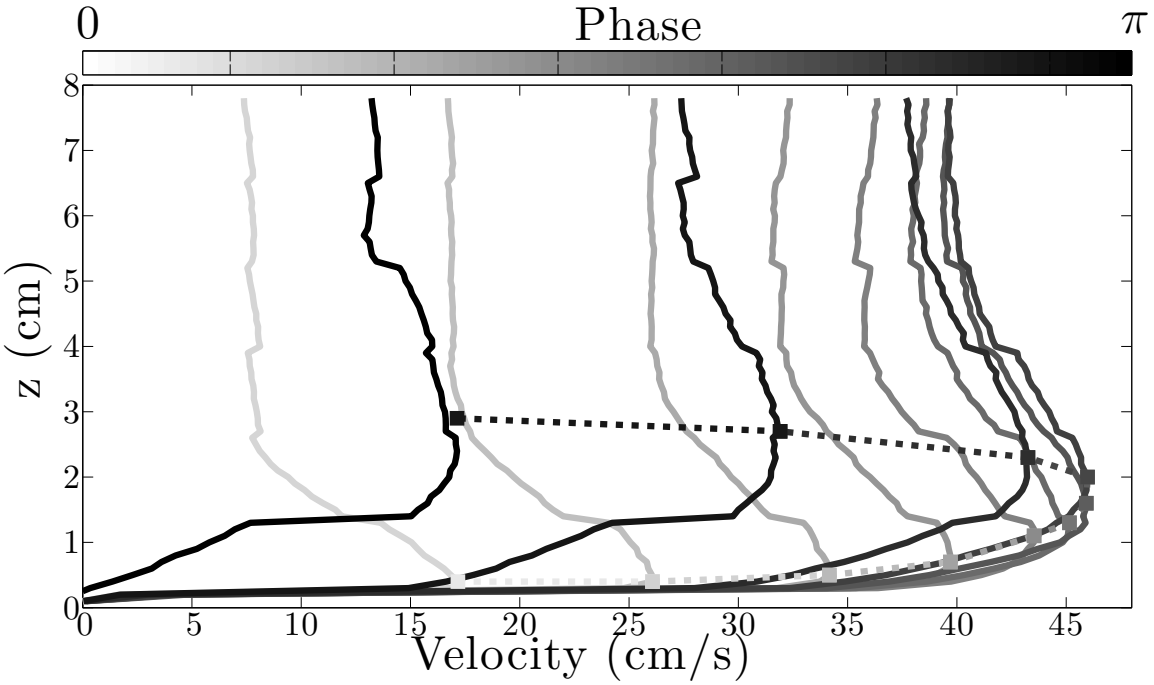

Figure 3.2 Wave boundary layer (WBL) growth over a half phase for a rough wall experiment with $U_{orb} = 45$ cm/s and $T = 7.4$ s. The dashed line marks the wave boundary layer height progression and the colors represent the phasing (white corresponds to $t = 0$, when the velocity is zero, and black corresponds to $t = T/2$, when flow reversal occurs).

shear within the boundary layer and overshoot zones are strongly modified. The modification of the wave boundary layer structure within the first half wave period is shown in Figure 3.2. The thickness of the wave boundary layer changes dramatically from 0.3 to 3 cm from the beginning of the wave period until it reaches maximum thickness at flow reversal when a new boundary layer develops. Variations in the maximum velocity and boundary layer thickness result in a peak boundary layer shear that occurs at $t = \frac{T}{8}$.

The wave boundary layer thickness is strongly influenced by bed forms and the turbulence level. In Figure 3.3, δ, estimated based on the velocity and Reynolds

stress profiles, is shown for the rough wall and sediment bed runs. The Reynolds stress generally switches sign at the top of the boundary layer because the sign of the shear also changes; thus, δ can also be estimated based on the zero crossing in the Reynolds stress profile. Wave boundary layer height scales with the ratio of shear velocity and wave frequency ($\delta \propto \frac{u_*}{\omega}$) (Hsu and Jan, 1998). In the rough wall experiments, δ increases as U_{orb} increases since u_* increases monotonically as U_{orb} increases. This is consistent with theoretical predictions for wave boundary layer thickness (Wiberg and Smith, 1983). In Figure 3.3 and subsequent figures, we use Re_Δ, defined in Equation 2.1, as the independent variable because it captures variations in U_{orb} and T; however, variation in Re_Δ primarily reflect variations in U_{orb} because of the stronger functional dependence on velocity and because U_{orb} was varied over a larger range than T. For all but the lowest Re_Δ, the observed boundary layer thicknesses are significantly greater than the analytical solution of the laminar boundary layer thickness ($\delta_{lam} \approx 3.75\sqrt{\frac{2\nu}{\omega}}$).

The boundary layer behaves very differently in the sediment bed experiments compared with the rough wall runs (Figure 3.3), in part because shear velocity does not increase as U_{orb} increases. For low Re_Δ, δ is 2-4 times greater than in the rough wall runs. As Re_Δ increases above 400-500, however, δ decreases significantly. As will be discussed later, the elevated values of δ for low Re_Δ are attributed to the presence of ripples in this regime and the reduction of δ is attributed to increased density stratification at high Re_Δ, in addition to a decrease in ripple steepness. Lamb et al. (2004) and Ozdemir et al. (2010a) both observed similar reductions in wave boundary layer thickness, and concluded that it was due to stratification. In their DNS runs, Ozdemir et al. (2010a) further show that the boundary layer can be laminarized,

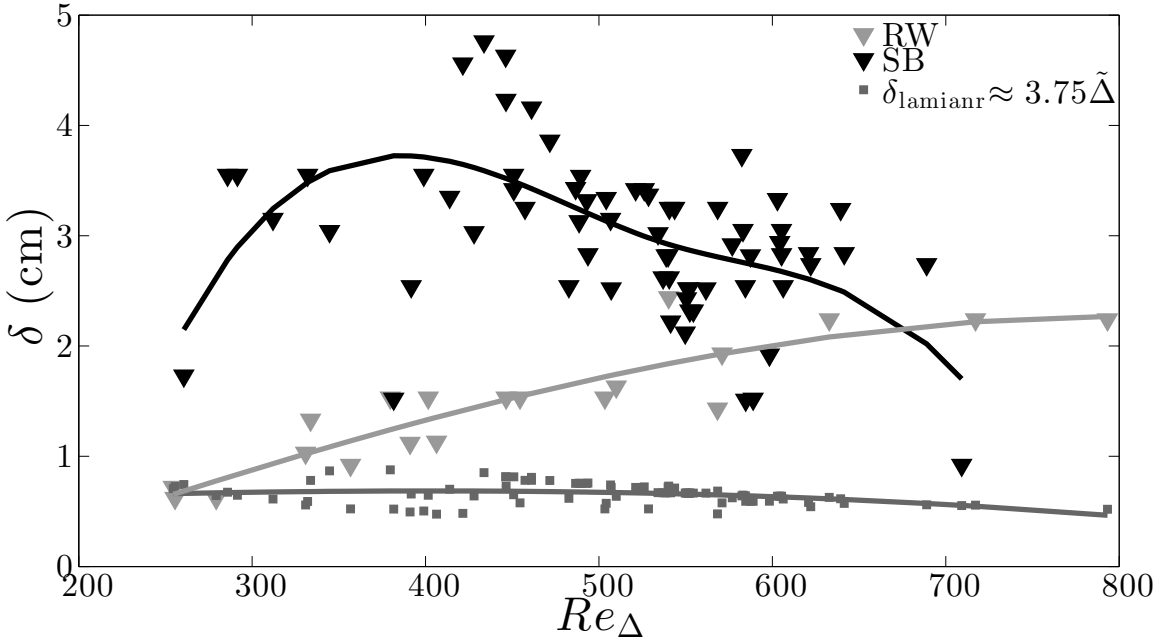

Figure 3.3 Wave boundary layer height (δ) for rough wall (gray) and sediment bed (black) experiments. Squares and triangles indicate measurements of δ based on the velocity and Reynolds stress profiles, respectively, as described in the text. The thick line is the mean value. The dark gray squares and fit to those data are an estimate of the laminar boundary layer thickness for each experiment.

however this is not observed in our experiments.

3.2.2 Phase lead and velocity ratio function

We use the the phase lead and velocity ratio functions (e.g. Sleath, 1970) to investigate whether there are systematic differences in the structure and phase of the mean velocity profile between the rough wall and sediment runs. The velocity field is modeled as

$$u(z,t) = U_{orb} f(z) \sin(\omega t + \phi(z)) \tag{3.1}$$

in which $f(z)$ and $\phi(z)$ are the velocity ratio and phase lead functions.

The velocity ratio function for each experiment was calculated by dividing the maximum velocity observed within the wave period at each height by the wave orbital velocity (Figure 3.4). The phase lead function was calculated by subtracting the phase of the maximum velocity occurrence at each height from the maximum velocity phase in the free stream zone. The velocity ratio and phase lead are plotted as a function of non-dimensional distance from the bed $a = z/l$, where $l = u_*/\omega$. The resulting profiles for all the rough wall and sediment bed runs were robust averaged to compare the boundary layer structure between these two cases.

The velocity ratio functions for both the rough wall and sediment bed runs display a similar structure (Figure 3.4-a). Both start from zero at the bed, increase to a maximum value at approximately $a = 1$, and then decrease to the free stream value near $a = 2$. The phase lead functions show some differences between the rough wall and sediment bed runs (Figure 3.4-b). Both profiles have maxima at the bottom and negative phase leads near the top of the boundary layer. The phase lead in the rough wall experiments is approximately 30°. This value is consistent with the results reported in prior studies (Ruessink et al., 2011; Lambrakos, 1982; Myrhaug et al., 1992), and is low compared with the 45° phase lead predicted for laminar boundary layers. The phase lead in the sediment bed runs differs from the rough wall runs; it is approximately 10° larger throughout the most of wave boundary layer and is less negative in the overshoot region. The modification of the phase lead profile is likely the result of sediment induced stratification, which can suppress turbulence in the boundary layer, as will be discussed in Section 3.4.

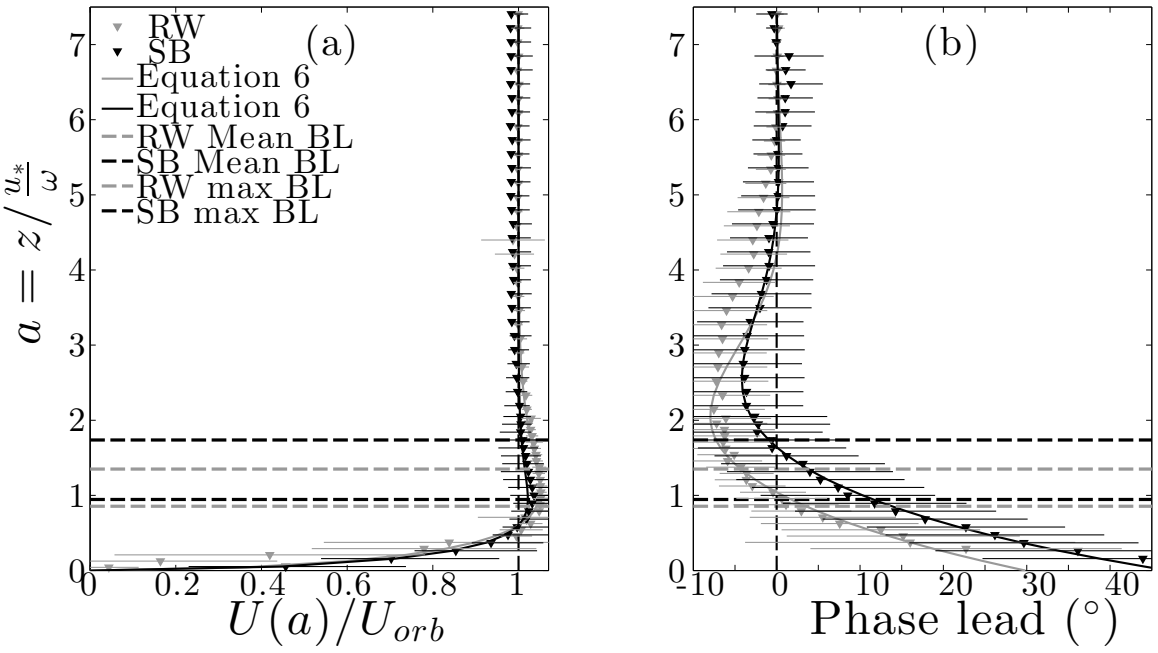

Figure 3.4 a) Velocity ratio ($f(z)$) b) phase lead $\phi(z)$ for rough wall (gray) and sediment bed (black) experiments. The vertical coordinate in the y-axis is non-dimensionalized according to $a = \frac{z}{\omega/u_*}$. The lines are fitted values based on a modified version of damped oscillator model formula by Sleath (1970) and Lambrakos (1982). The solid horizontal lines show the standard deviation from the mean value for each height. The dashed horizontal lines show the non-dimensionalized mean wave boundary layer height in for rough wall (gray) and sediment bed (black) run

3.3 Bed response and sediment profile

The addition of an active sediment bed adds two primary components to the wave boundary layer. First, the mobile bed can form ripples and bedforms that increase the roughness of the bed and modify the turbulence in the wave boundary layer. Second, sediment is suspended in and above the wave boundary layer, where it can modify the effective density of the fluid and exert an influence on the turbulence via density stratification. In addition, the high concentration suspended sediment layer that is generated by the turbulent flow is available to be transported due to its negative buoyancy when the bed is sloped. Here we report the variations in bedforms and the suspended sediment concentration profiles.

3.3.1 Bedforms

Bedforms play an important role in initiation of sediment suspension, governing the bed shear stress and intensifying near-bed turbulence. They appear in many natural environments and have different shapes and patterns depending on the flow structure and the particle size distribution of the bed. In shallow regions of the inner continental shelf, the dominant bedforms are ripples (Hanes et al., 2001). These ripples typically have irregular two-dimensional forms, similar to those observed in the present laboratory experiments. A few non-dimensional numbers have been proposed to determine the criteria for existence of ripples and their steepness, wave length and height.

Grant and Madsen (1982) determined ripple type based on the bed shear stress non-dimensionalized by the critical shear stress. Nielsen (1981) and Van Rijn (1993) used the mobility number defined as $\psi = \frac{U_{orb}^2}{sgD_{50}}$ where $s = 1.65$ is the submerged weight

of sediment relative to water and D_{50} is the median size for sediment particles. Wiberg and Harris (1994) used near-bed orbital diameter ($d_0 = \frac{2U_{orb}}{\omega}$) non-dimensionalized by the ripple height ($\frac{d_0}{\eta}$) where η is ripple height.

Ripples are observed in almost all of our sediment bed experiments, and their morphology changes as the flow forcing is varied. We interpret these changes following Wiberg and Harris (1994), who suggested that ripples be classified into three types based on the dimensionless orbital diameter d_0/η. Here, $d_0 = \frac{2U_{orb}}{\omega}$ is the orbital diameter and η is the ripple height. According to the Wiberg and Harris (1994)'s classification scheme, orbital ripples are observed when $d_0/\eta < 20$ and have wavelengths proportional to the wave orbital diameter. Anorbital ripples are observed when $d_0/\eta > 100$ and have wave-lengths proportional to the grain size and independent of orbital diameter. Finally, suborbital ripples are observed when $20 < d_0/\eta < 100$ and have wavelengths that are not proportional to the orbital diameter or grain size.

The ripple height and wavelength λ in our experiments were estimated from multiple photographs taken through the tank wall during each experiment. The ripple steepness η/λ was then calculated and averaged over the experiment period. Almost all of the ripples observed in our experiments were in the anorbital range (Figure 3.5). The curve suggested by Wiberg and Harris (1994) captures our data relatively well; however, it overestimates the ripples steepness for high d_0/η. Note that, while the sediment that was used in the sediment bed runs was mostly fine silt ($D_{50} = 23\,\mu\,m$), Lamb and Parsons (2005) showed that the sediment in the ripples consist primarily of sands ($D = 70\,\mu\,m$) as a result of sediment bed coarsening. Lamb and Parsons (2005) used similar sediment and the same flow facility for their experiments.

We observe that ripple steepness decreases with increasing wave forcing (Re_Δ),

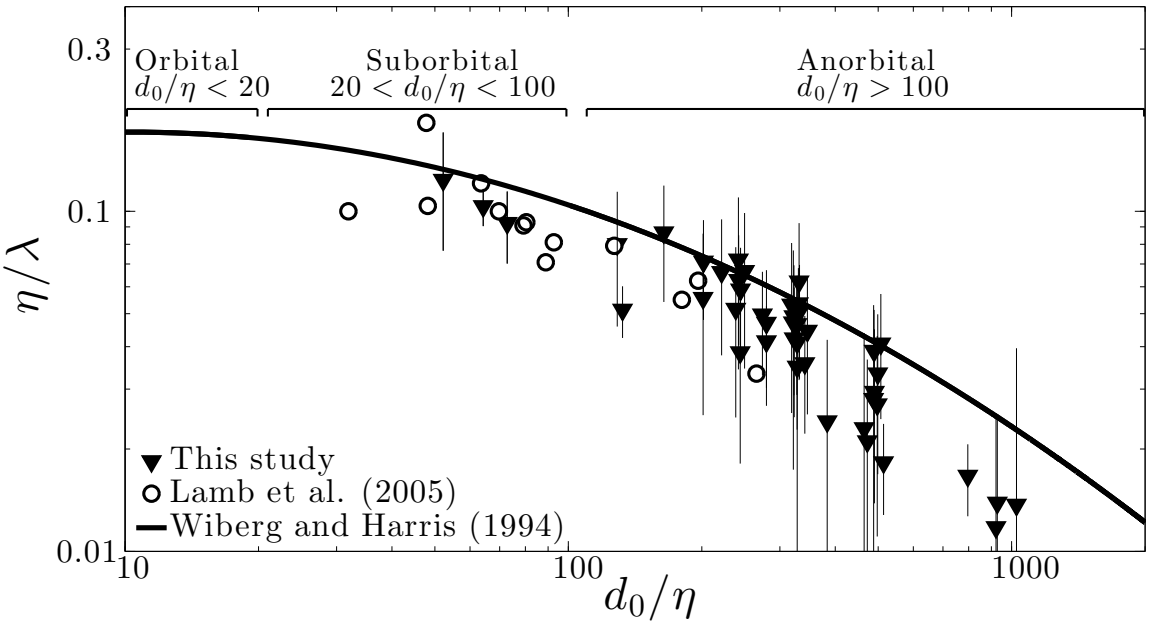

Figure 3.5 Ripple steepness versus non-dimensional orbital diameter for sediment bed experiments. The vertical and horizontal lines are the standard deviations based on the variability within each experiment. The three ripple classifications and the predictive model developed by Wiberg and Harris (1994) are shown with over brackets and the black line, respectively.

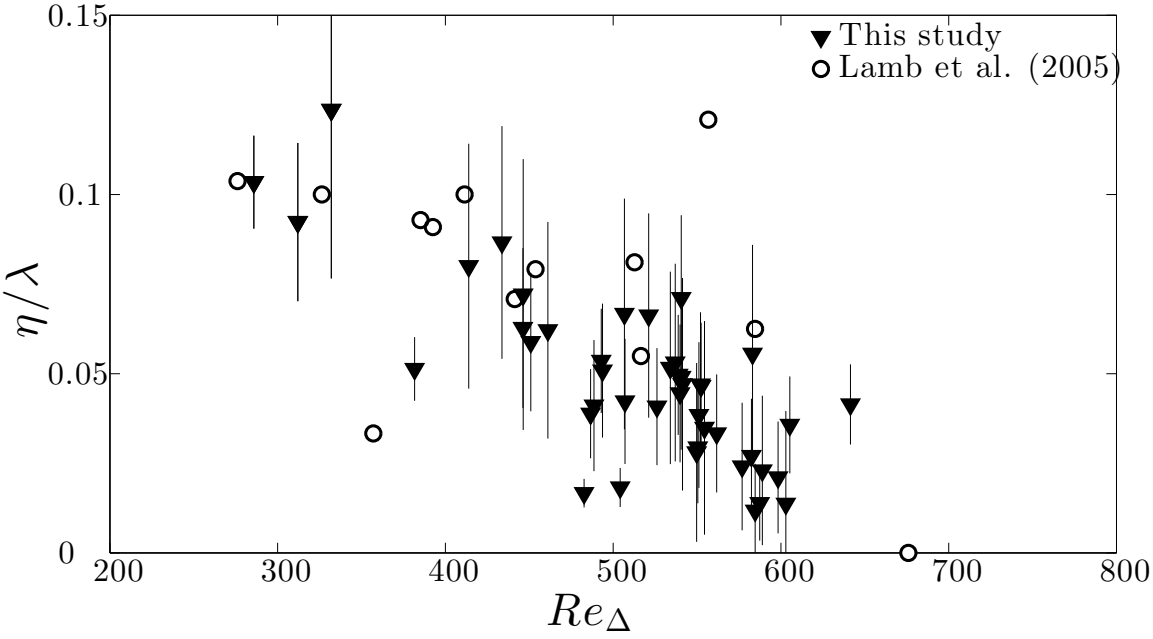

Figure 3.6 Variation of ripple steepness with Reynolds number. Error bars are based on the range of ripple steepness observed within each run.

consistent with the findings of Wiberg and Harris (1994) (Figure 3.6). Higher wave orbital velocities suspend more sediment and this higher proportion of sediments in suspension is associated with a decrease in ripple steepness (Wiberg and Harris, 1994). The range of ripple heights, from 1 to 10 mm, is well below the wave boundary layer height ($\eta/\delta_w < 0.25$), consistent with the characterization of the bedforms as anorbital ripples; orbital ripple heights are larger than the wave boundary layer ($\eta/\delta_w > 2$) (Wiberg and Harris, 1994). The ripple height, wavelength and steepness observed in our experiments are in the same range as those reported in previous experiments (Lamb and Parsons, 2005; Van Rijn, 2007; O'Donoghue et al., 2006; Vongvisessomjai, 1984).

3.3.2 Suspended sediment concentration

The observed SSC profiles for the sediment bed experiments decrease approximately exponentially from their peak value at the bed to a constant background value far from the bed, which is due to mixing in the end tanks (Figure 3.7). We designate C_a as the near-bed concentration and C_b as the background concentration. For each experiment, a SSC profile in the form of $c(z) = C_b + C_a e^{-\alpha z/h}$ was fit to the data. In this study, although we see high sediment concentrations similar to those observed in the field, the structure of the near-bed sediment profile does not display the uniform SSC layer below the lutocline observed in some field studies (e.g. Cacchione et al., 1995; Ogston et al., 2000). Instead, the concentration always increases exponentially toward the bed similar to experimental and field observations of Lamb et al. (2004) and Traykovski et al. (2007). Here, we define the lutocline (h) as the point where the SSC is $0.05C_a$. Therefore, α is chosen to be 3 to satisfy this condition. The background concentrations (C_b) in all experiments are subtracted from SSC profiles for further analysis since it is the vertical density gradient, rather than the absolute value, that influences density stratification. Elevated sediment concentrations may influence the effective viscosity of the fluid; however this effect is only significant in the two highest experiments and will be discussed in a future paper. For the low velocity experiments, relatively less sediment is in suspension and the near-bed layer is relatively dilute. As the wave orbital velocity increases, SSC increases and a clear high concentration layer is observed. The dilute and high concentration sediment suspension regimes in wave-supported flows were also observed experimentally by Lamb et al. (2004) and in the field by Traykovski et al. (2007).

In Figure 3.8, the height of the lutocline, near-bed SSC and average SSC gradient

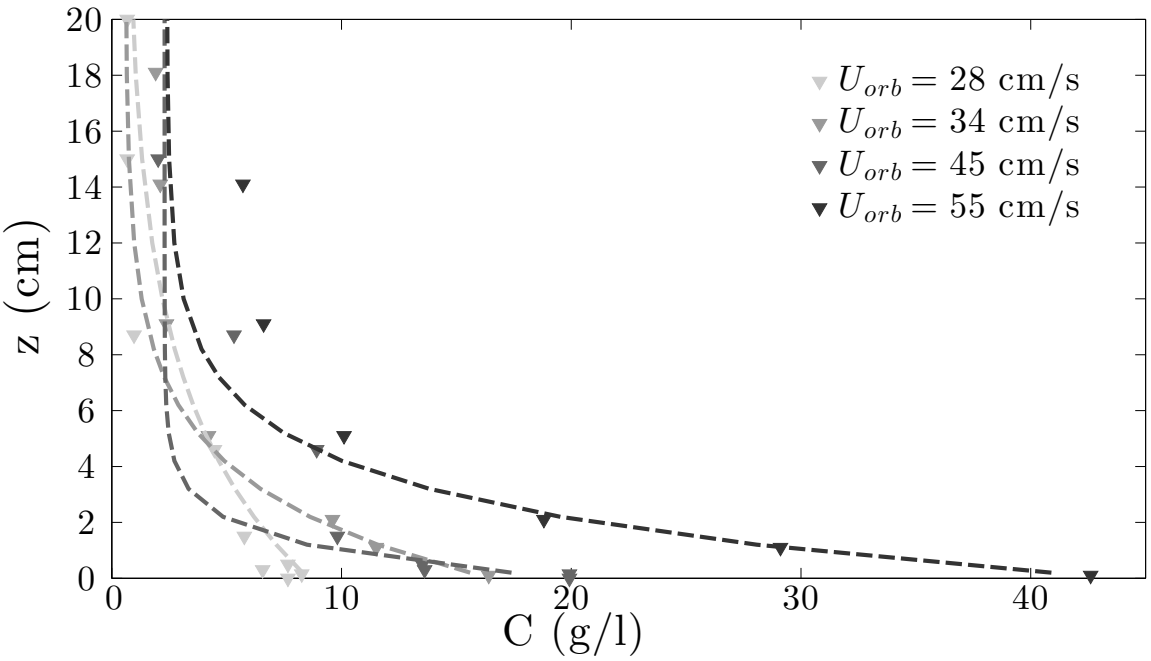

Figure 3.7 Suspended sediment concentration profiles for experiments with different wave orbital velocities. The points show the data from siphon measurements and the lines are the best fit to the data in the form of $c(z) = C_b + C_a e^{-az}$

.

inside the high concentration layer are shown. The height of the lutocline decreases as the wave orbital velocity increases (Figure 3.8-a). Note that there is quite a bit of scatter in the lutocline heights at low Re_Δ because the concentration gradient at the top of the layer is much smaller. In all of our experiments, the lutocline height was greater than the wave boundary layer, which suggests that turbulence may be transported vertically to regions above the wave boundary layer (Lamb et al., 2004). The lutocline heights in our experiments are similar to those observed in the field by Traykovski et al. (2007). For our experiments h/δ was approximately 3.2 ± 1.8. The lutocline height decreases with increasing Re_Δ, consistent with the observed decrease in δ (Figure 3.3). The generation of a high concentration mud layer with increasing wave intensity is clear in Figures 3.8-b and 3.8-c, which show that both near-bed reference SSC (C_a) and sediment concentration gradient increase dramatically when Re_Δ exceeds a critical value of approximately 450. The near-bed SSC and SSC gradient are both constant and small for low Re_Δ and increase when $Re_\Delta > 450$, eventually reaching values 3-4 times greater than those at low Re_Δ. The threshold for the generation of a high concentration mud layer in our experiments corresponds to a wave orbital velocity of approximately $25 - 30\,\mathrm{cm\,s^{-1}}$. This is consistent with the threshold observed by Lamb et al. (2004); they report that no high density suspension layer is generated in their experiments when the wave orbital velocities were smaller than $30.3\,\mathrm{cm\,s^{-1}}$ (run S4 in their paper).

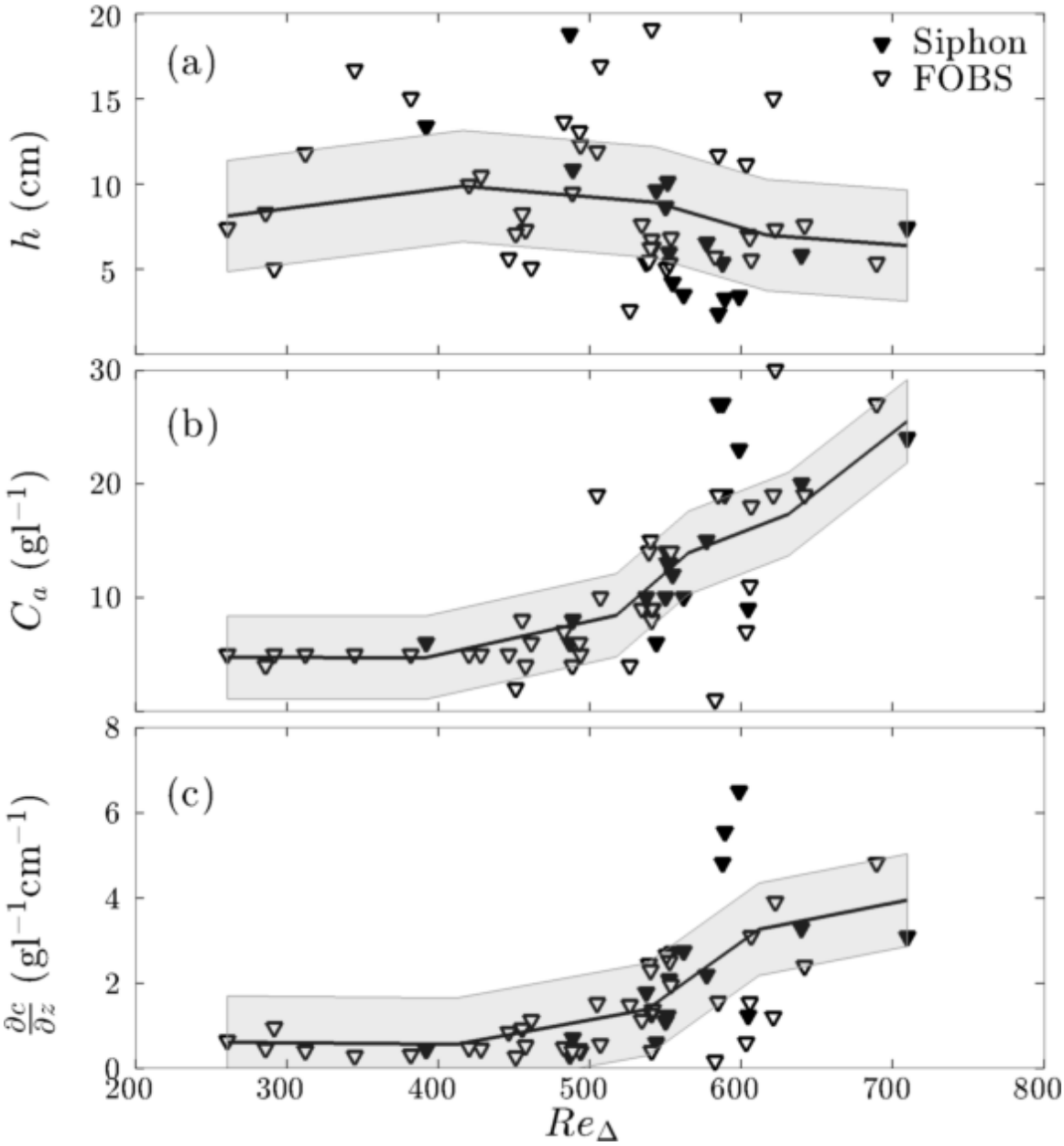

Figure 3.8 High concentration mud-layer (a) thickness, h (b) near-bed concentration, C_a, and (c) concentration gradient. All values are derived from the fit to the concentration profiles using $c(z) = C_b + C_a e^{-3z/h}$. The black and white triangles show measurements using the siphon or FOBS, respectively. The solid lines are the bin-averaged values.

3.4 Turbulence in the wave boundary layer

3.4.1 Reynolds stress

The phase-averaged near-bottom Reynolds stress is shown in Figure 3.9 for an example rough wall run ($U_{orb} = 57\,\mathrm{cm\,s^{-1}}$ and $T = 5.8\,\mathrm{s}$). At flow reversal (zero phase) the Reynolds stress very near the bottom is close to zero. As the wave velocity increases, the magnitude of the opposing near-bottom stress increases, reaching its maximum value at maximum velocity phase. The thickness of the high stress layer increases slowly immediately after flow reversal and then increases more rapidly until the subsequent flow reversal. After flow reversal the very near-bottom stress goes to zero as it switches sign, but significant stress from the preceding wave phase persists as a residual stress. This residual stress has the opposite sign of the very near-bottom stress and continues to penetrate upwards well above the height of the wave-boundary layer. The residual stress generally persists for a half wave period after flow reversal, though low levels of residual stress are sometimes observed after even longer periods (Figure 3.9).

The height of the wave-boundary layer, δ, based on the velocity maximum is shown in Figure 3.9 (black line). It is clear that there is very good correspondence between the observed Reynolds stress profiles and δ; the top of the boundary layer separates the near-bottom boundary layer stress from the residual stress that persists from the previous wave phase. The upward penetration of turbulence may provide a mechanism for transport of sediment from the wave-boundary layer into the overlying fluid. We will see, however, that the residual stress is less intense in the sediment bed runs, especially in runs with a high concentration mud layer.

In Figure 3.10 we present the Reynolds stress for five rough wall runs with increas-

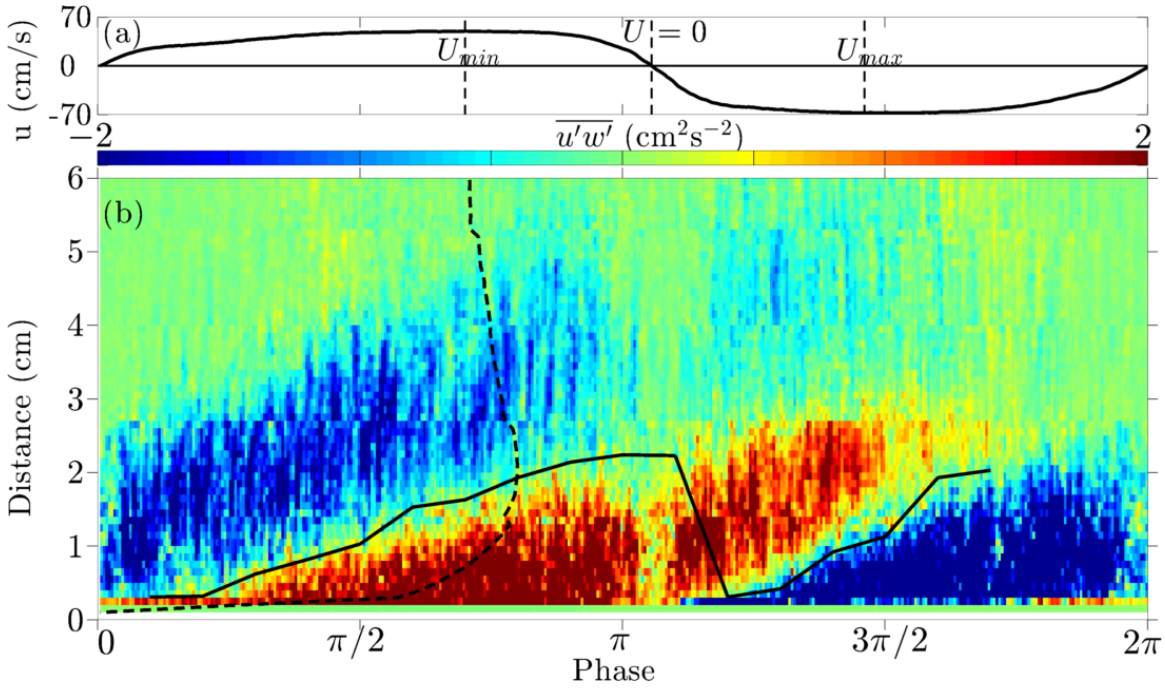

Figure 3.9 Reynolds stress (cm^2/s^2) for a rough wall with U_{orb}=57cmsˆ$^{-2}$ and $T = 5.8$ s. The vertical dashed lines indicate the minimum, zero and maximum velocity phases. The solid lines indicate the boundary layer height derived from the height of the maximum velocity. The curved dashed line shows a sample velocity profile at $3\pi/4$.

ing Re_Δ (increasing U_{orb}) and corresponding sediment bed runs with the same wave settings. For the rough wall runs, the Reynolds stress is very low when Re_Δ is low (Figure 3.10-a) and increases gradually as Re_Δ increases (Figures 3.10b-e). The wave boundary layer also gets thicker as Re_Δ increases and we observe that the transition to a thicker boundary layer occurs earlier as Re_Δ increases.

We observe a very different evolution in the Reynolds stress in the corresponding sediment bed experiments. First, the Reynolds stress is significantly more intense and the wave-boundary layer is thicker in the low Re_Δ sediment bed runs (Figures 3.10-f and 3.10-g) than in the corresponding rough wall runs (Figures 3.10-a and 3.10-b). The elevated stress at low Re_Δ is most likely due to the occurrence of bed forms in this regime, as discussed below. Second, while Reynolds stress and δ increase uniformly with Re_Δ in the rough wall runs, they appear to decrease slightly in the high Re_Δ sediment bed runs (Figures 3.10-h, 3.10-i and 3.10-j). This decrease is observed for runs with $Re_\Delta > 450$ ($U_{orb} > 30\,\mathrm{cm\,s^{-1}}$) when we observe that the high concentration mud layer forms, suggesting that it is associated with turbulence suppression due to stratification. Finally, we observe that the residual Reynolds stress has lost its intensity due to dissipation / diffusion or both earlier in the high Re_Δ sediment bed runs, relative to the rough wall runs. As discussed in Section 3.3.2, the height of the lutocline is typically 3-4 times greater than δ; thus it is likely that the reduction in residual stress in the sediment bed runs is due to the persistence of sediment stratification above the wave boundary layer.

We define the shear velocity $u_* = (\overline{-u'w})^{1/2}$ as the maximum Reynolds stress in the boundary layer (Figure 3.11), which enables us to more easily compare and quantify the differences in behavior between the rough wall and sediment bed runs

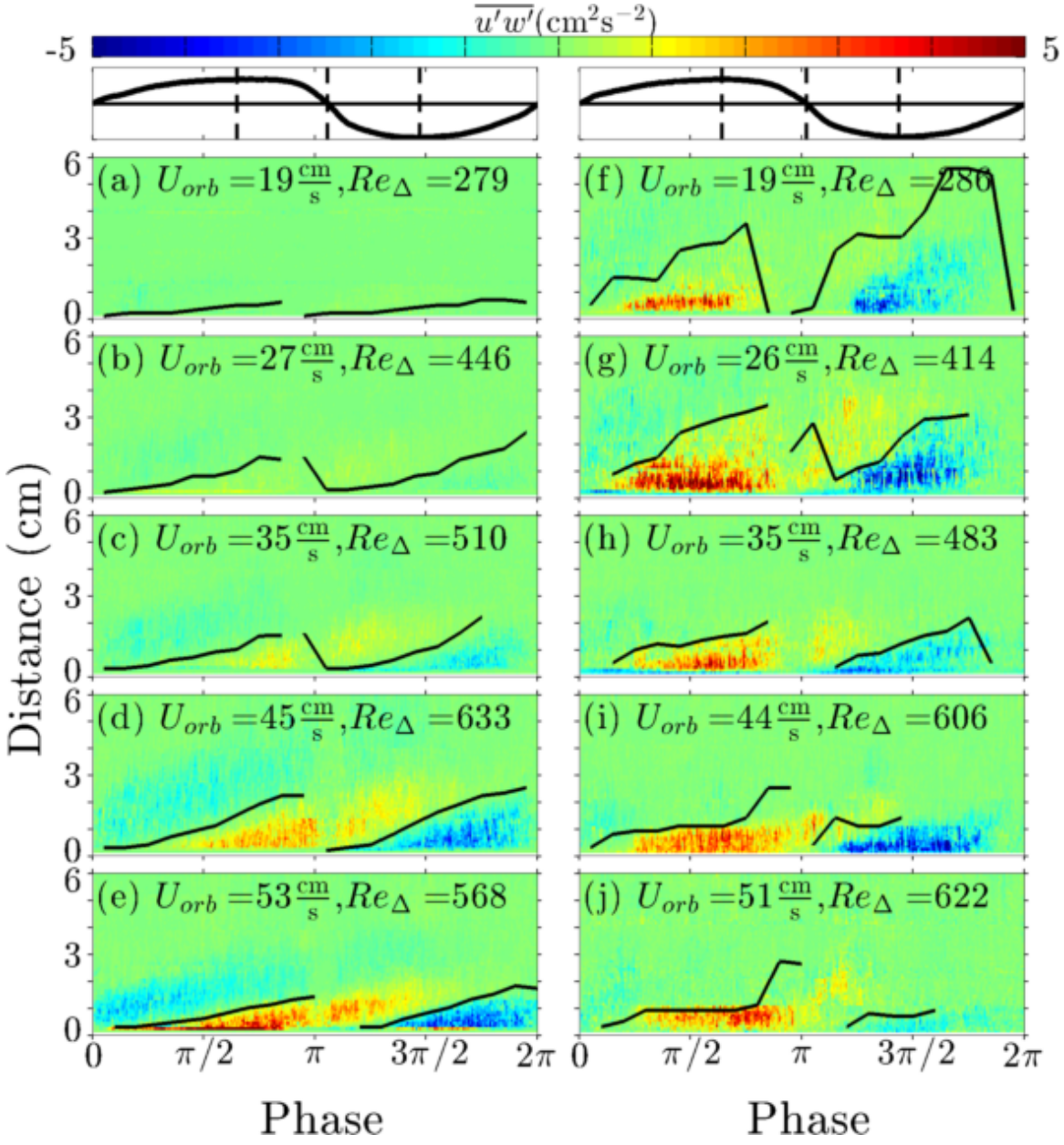

Figure 3.10 Reynolds stress for the rough wall (left panels) and the sediment bed (right panels) runs. The vertical dashed lines show minimum, zero and maximum velocity phases in each panel. The solid lines show boundary layer heights derived from maximum velocity. The colors the negative of measured values so that $-\overline{uw}$*isshown*

observed in Figure 3.10. We calculate u_* based on the vertical mean between the bed and the top of the wave boundary layer and the temporal maximum over a wave period. In the rough wall runs, u_* increases monotonically with Re_Δ, as expected (e.g. Nielsen, 1992). For the sediment bed runs, u_* is initially elevated and then appears to stay constant or decrease as Re_Δ increases. When $Re_\Delta < 450$ ($U_{orb} < 30$ cm s^{-1} for a 8-s wave), the shear velocity is approximately 3-4 times larger in the sediment bed runs than in the rough wall runs. This elevated stress is associated with the presence of larger, steeper ripples in this regime (Figure 3.6). In this regime we also observe an increase in u_* with increasing the wave orbital velocity, which is approximately similar to the rate observed in the corresponding rough wall experiments. When $Re_\Delta > 450$ ($U_{orb} > 30\,\mathrm{cm\,s^{-1}}$ for a 8-s wave), u_* remains constant or decreases as Re_Δ increases, eventually resulting in lower values of u_* in the sediment bed runs relative to the rough wall runs at the highest Re_Δ values. In this range, although small, long-wavelength ripples still exist, turbulence suppression due to vertical density stratification in the sediment bed experiments appears to be sufficient to reduce the shear velocity below that observed in the rough wall experiments.

The temporal variability and magnitude of the shear velocity that we observe in our rough wall runs is consistent with experiments by Hay et al. (2012a). However, the observed magnitudes are smaller than those observed in the field (Traykovski et al., 2007), possibly because we use the maximum depth averaged Reynolds stress in the boundary layer to determine shear velocity instead of law of wall or wave friction coefficient.

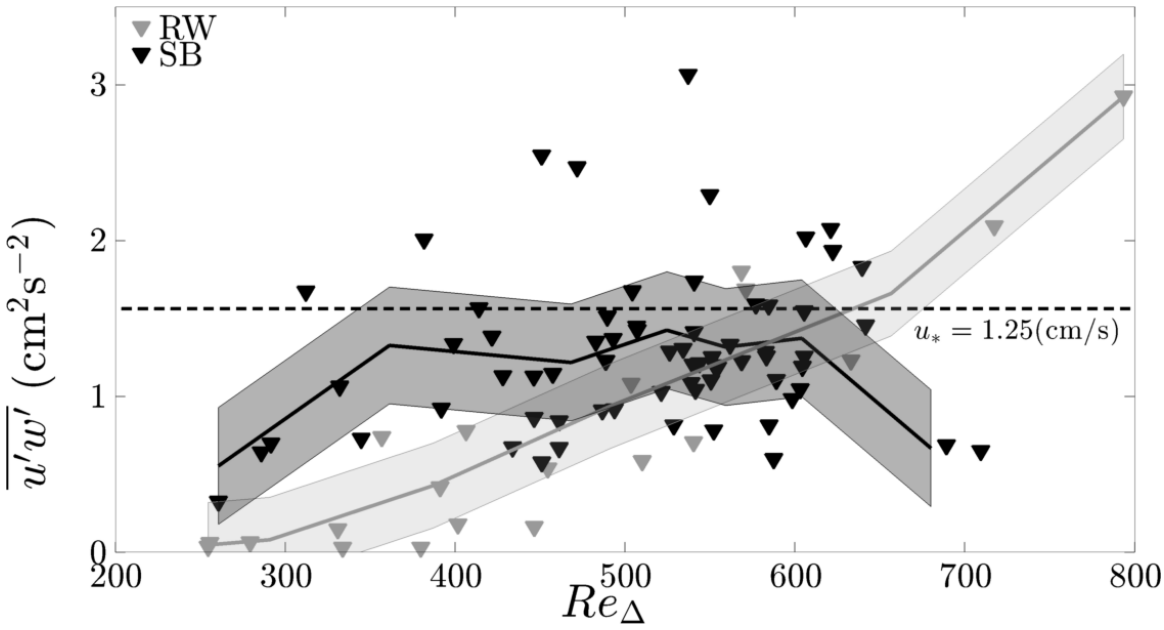

Figure 3.11 Comparison of shear velocity for rough wall (gray) and sediment bed (black) runs. Shear velocity is defined as the average Reynolds stress in the wave boundary layer, as described in the text. The dark gray areas show the 95% confidence interval.

3.4.2 Turbulent Kinetic Energy

The results in Section 3.4.1 describe how the presence of sediment can increase or decrease the turbulent stress and motivate the need for a clear understanding of the turbulent dynamics in high sediment concentration wave boundary layers. The turbulent kinetic energy (TKE) and TKE production rate (P) for the rough wall and sediment bed experiments are shown in Figure 3.12. As with the Reynolds stress, TKE and P are averaged spatially over the height of the boundary layer and temporally over one wave period. The comparison between the rough wall and sediment bed values for both of these parameters is generally similar to the results obtained with Reynolds stress; TKE and P both increase monotonically in the rough wall experiments, whereas they are both elevated in the sediment bed experiments for low Re_Δ and reduced for high Re_Δ, relative to the corresponding rough wall values. Both TKE and P are relatively constant across a wide range in Re_Δ, although P appears to decrease slightly in magnitude. At low Re_Δ, P is approximately one order of magnitude greater in the sediment bed runs than in the corresponding rough wall runs.

3.5 Discussion

Understanding the physical details of wave-supported mud flows is a key step in improving our prediction of sediment transport across the continental shelf. High resolution measurements of the dynamics of these flows are challenging in the field because they have relatively small vertical scales and are very episodic in nature. The present laboratory experiments simulate the conditions under which wave-supported mud flows occur on the continental shelf and use detailed measurements of velocity

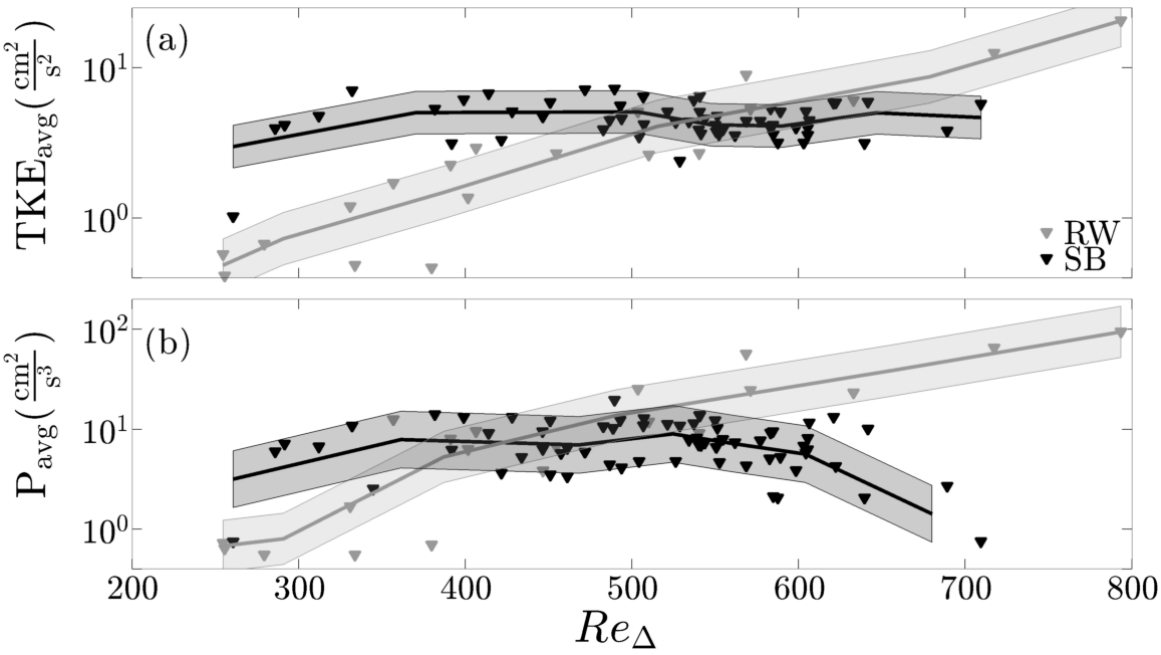

Figure 3.12 Average (a) turbulent kinetic energy and (b) turbulent kinetic energy production within the wave boundary layer for rough wall (gray) and sediment bed (black) runs. The lines are fitted values to the experimental data.

and turbulence with and without sediment to understand the relationship between bed dynamics, suspended sediment and turbulence in the wave boundary layer. Our overall goal is to clarify the processes that determine the vertical profiles of suspended sediment and velocity in wave-supported mud layers in order to improve models of cross-shelf sediment transport.

The qualitative character and the dominant dynamics of the observed flow vary significantly across the parameter space of our experiments and suggest that the flow should be described in two distinct regimes. The regimes are differentiated in terms of the Stokes Reynolds number (Re_Δ) and the primary attributes are summarized schematically in Figure 3.13, which summarizes the key measurements from the present experiments. Regime I occurs when $Re_\Delta < 450$, which corresponds approximately to $U_{orb} < 30\,\mathrm{cm\,s^{-1}}$. The flow in this regime is dominated by the presence of ripples and characterized by a dilute sediment suspension; no high concentration mud layer or distinct lutocline forms (Figures 3.13-a and 3.13-b). The turbulent kinetic energy production is significantly higher in the sediment bed experiments compared with corresponding rough wall experiments as a result of the increased bed roughness associated with ripple formation (Figure 3.13-c). For all experiments in this regime, the near-bed sediment concentration and vertical concentration gradient were low and approximately constant with respect to Re_Δ, suggesting that density stratification effects were minimal (Figure 3.13-b). Regime II occurs when $Re_\Delta > 450$). Flow in this regime is dominated by the formation of a high concentration mud layer and the associated vertical density stratification dominates the dynamics. The ripples are approximately half as steep as they are in Regime I, and their importance to the overall dynamics appears to be small (Figure3.13-a). The magnitude of TKE and P

are smaller in the sediment bed experiments than in the corresponding rough wall experiments (Figure 3.13-c). It is important to note that the ripples do not disappear completely in the high Re_Δ runs and so the bed remains rougher than in the rough wall runs. Thus, the facts that the turbulence levels in the sediment bed experiments do not increase with Re_Δ and remain below the levels of the rough wall experiments cannot be explained by the change in bed roughness alone. Strong density stratification (Figure 3.13-b) appears to be effective at suppressing turbulence in the wave boundary layer and reducing the wave boundary layer thickness. Turbulence near the upper boundary and above the wave boundary layer can be completely suppressed due to this high density stratification.

The present experiments confirm and extend some of the conclusions in Lamb et al. (2004) and Lamb and Parsons (2005) and also provide some notable differences. Their results support the definition of the two regimes described above; they also observe that no high concentration layer forms for low U_{orb} (corresponding to low Re_Δ) and suggest that density stratification is important for reducing the boundary layer thickness in sediment bed runs with higher U_{orb}. Lamb and Parsons (2005) describe ripple formation and their results, which are re-plotted in Figure 3.6, are consistent with the present results, also showing that ripple steepness decreases for high Re_Δ (Regime II). Lamb et al. (2004) report that turbulence suppression associated with density stratification resulted in wave boundary layers smaller than 3 mm, which approaches the thickness expected for laminarization of the boundary layer. This magnitude of boundary-layer reduction was not observed in our experiments. In fact, while we do observe a decrease in δ as stratification increases, δ is higher in almost all of the sediment bed runs than it is in the corresponding rough wall runs. We expect

that this difference in δ between our results and Lamb et al. (2004) is probably due to the increased resolution provided by the profiling ADV used in the present study compared with Lamb et al. (2004)'s point-wise velocity measurements. A central conclusion in Lamb et al. (2004) is that there is a large mismatch between the thickness of the mud layer and boundary layer, which requires that there is significant upwards transport of turbulence from the thin energetic boundary layer region to maintain suspension of sediment in the region above the boundary layer. We also observe that $h > \delta$, though the mismatch is only a factor of $3 - 4$ in our observations. However, we were not able to confirm the importance of the turbulent transport term with our measurements. Finally, Lamb and Parsons (2005) point to the important role that sorting of grains of different size may play in the dynamics of the mud layer as U_{orb} increases. In Section 3.5.3 we discuss the importance of the suspended sand fraction in our observations.

3.5.1 Ripples

Ripples were observed in most of the sediment bed experiments and appear to play an important role in generating turbulence, especially at low Re_{Δ}. Ripples emerge in systems with an active bedload layer, and thus require a minimum amount of sand on the bed (Wiberg and Harris, 1994). Although our initial sediment bed contained primarily silt-size particles, segregation of sand as a result of the suspension of clays and fine silts coarsened the sediment bed, resulting in a significant active bedload layer and supporting the formation of ripples. This process is described in more detail in Lamb and Parsons (2005). Ripples change the bottom roughness significantly, which can increase the turbulence in the wave boundary layer and the boundary layer thickness. In the present experiments steep ripples were observed in low Re_{Δ}

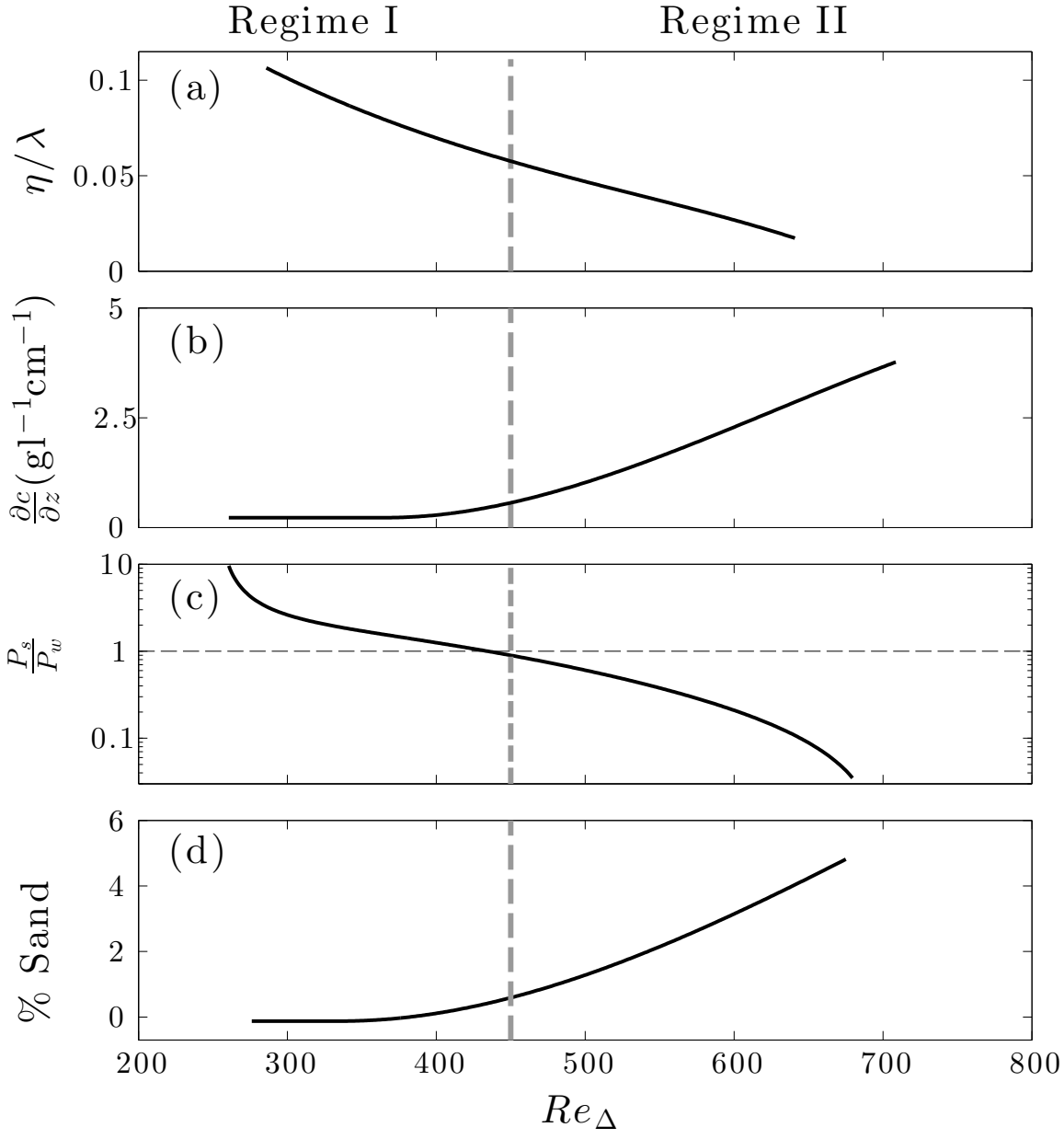

Figure 3.13 Fits to experimental data for (a) ripple steepness, (b) buoyancy, (c) average turbulent kinetic energy underneath the wave boundary layer and (d) % sand content from experimental results of Lamb and Parsons (2005)

conditions. As Re_Δ increases the ripples steepness decreases by an order of magnitude from 0.1 to 0.01. The existence of ripples can significantly change the vertical structure of the velocity field and turbulence in and outside of the wave boundary layer. Doering and Baryla (2002) showed that the velocity field is strongly influenced by the presence of ripples in their experimental wave flume. They concluded that ripples can strongly influence the velocity structure in a region above the ripples that is $2-4$ times the ripple height. In our low Re_Δ experiments, the observed boundary layer heights are $3-4$ cm compared with ripple heights of $0.1-1$ cm. This is consistent with the upward penetration of ripple-generated turbulence observed by Doering and Baryla (2002), and suggests that the enhanced thickness of the wave boundary layer in our low Re_Δ sediment bed experiments is a result of ripples.

We test this further by computing the predicted TKE production with and without ripples (Figure 3.14-a) and comparing this with our observations. The prediction uses only the observed wave orbital velocity and period and varies the bed roughness based on the observed ripple heights. It isolates the effect of the ripples on boundary layer turbulence and does not account for density stratification. The depth integrated production is estimated according to

$$P_k = \beta u_*^2 U_{orb} \tag{3.2}$$

in which β takes into account the temporal variations in wave period and is chosen to be 0.3 based on our experimental results. The shear velocity is $u_* = \sqrt{f_w/2}U_{orb}$, in which the wave friction coefficient is estimated following Nielsen (1992) from

$$f_w = \exp(5.5(r_h/A)^{0.2} - 6.3) \tag{3.3}$$

where $A = U_{orb}/\omega$ is the wave excursion amplitude of the interior flow immediately outside the boundary layer and r_h is the hydraulics roughness of the bed. For the rough wall experiments, r_h is chosen to be the size of the sand grains on the rough bottom, $D_{50} = 0.75$ mm. These results agree qualitatively with the average TKE and production measured in our experiment for $Re_\Delta < 450$ (Figure 3.12-b). For the sediment bed experiments, the observed ripple amplitudes and wavelengths were used to compute the roughness based on $r_h = 24\eta^2/\lambda$ (Thorne et al., 2002; Hay et al., 2012b). The predicted TKE production increases monotonically in rough wall experiments as expected (Figure 3.14-a). When ripples are present, the production is significantly higher than in the corresponding rough wall runs, as observed in our measurements (Figure 3.12). This comparison further confirms that the observed enhancement of turbulence for low Re_Δ is due to ripples. However, when $Re_\Delta > 450$ and the ripple steepness decreases, the predicted TKE production continues to increase in the ripple runs and is comparable to the production in the rough wall runs (Figure 3.14-a). This prediction is in contrast to the high Re_Δ measurements, in which the production is significantly lower in the sediment bed runs than in the rough wall runs (Figure 3.12-b). Thus the prediction shows that production should increase for high Re_Δ even though most of the ripples are washed out and another process is required to explain the observed suppression of turbulence. In the following section we discuss the role of density stratification in suppressing turbulence in the wave boundary layer.

3.5.2 Stratification

Density stratification associated with high near-bed sediment concentrations can suppress turbulence in highly stratified flows (Winterwerp, 2006). In oscillatory boundary

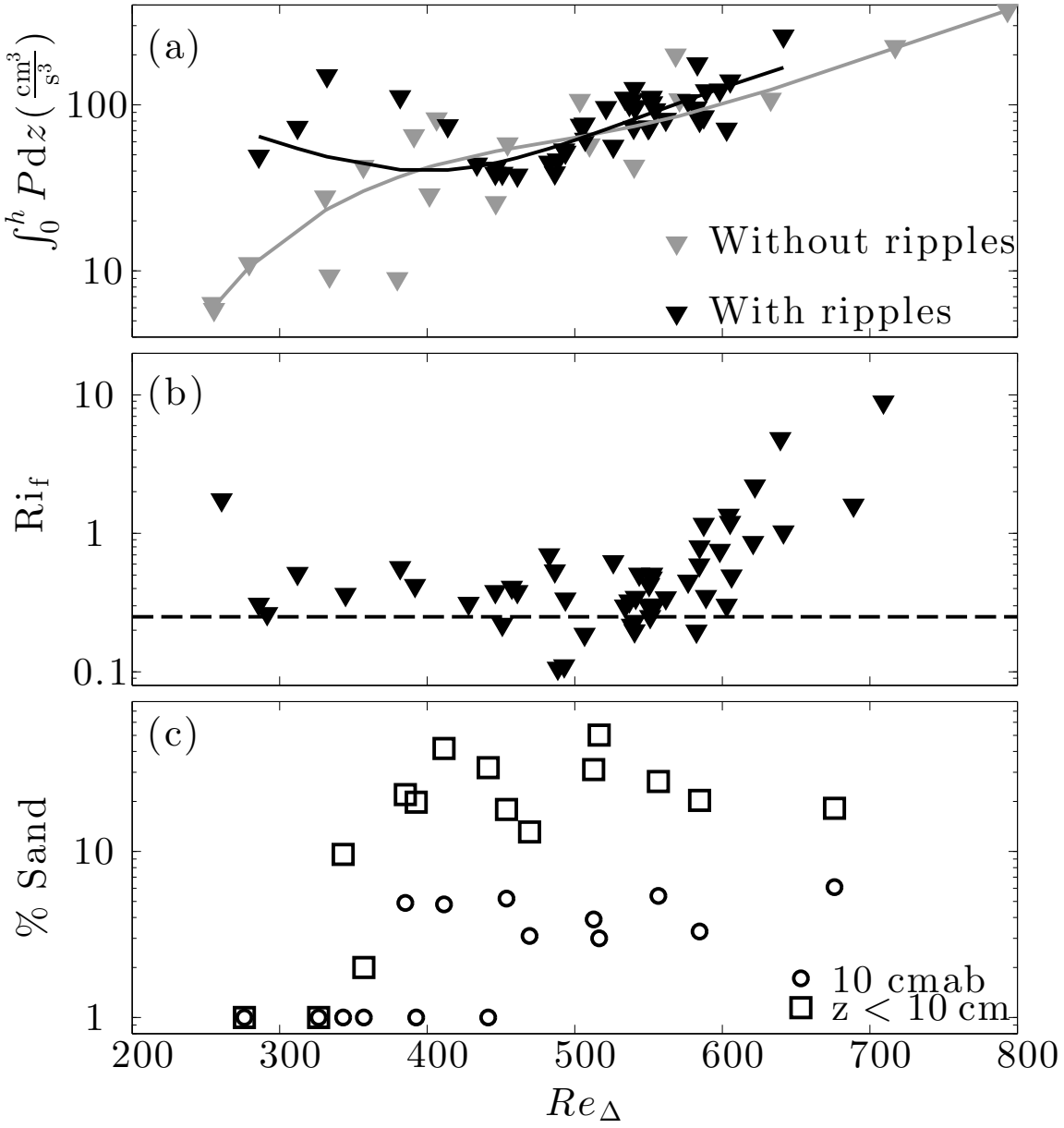

Figure 3.14 (a) Depth integrated production based on roughness scales observed in the rough wall (gray) and sediment bed (black) experiments. The values represent predictions of the production based on the observed U_{orb} and ripple steepness. The lines are spline fits intended to illustrate the overall trend. (b) Flux Richardson number defined as the ratio of buoyancy flux to TKE production rate where buoyancy was estimated using eddy diffusivity from Thorne et al. (2009) (c) Sand fraction at 10 cmab and the average sand fraction below 10 cmab from the experiments of Lamb and Parsons (2005)

layers, high density stratification may decrease the wave boundary layer thickness and turbulence intensity. Although the turbulence level is dramatically reduced, the turbulent energy is sufficient to maintain particle suspension in such highly stratified layers primarily due to hindered settling (Winterwerp, 2006).

The numerical model results of Ozdemir et al. (2010a) suggests that turbulence suppression associated with high concentration fluid muds may be sufficient to laminarize the wave boundary layer. They investigate the effects of fine sediment on turbulence in the vicinity of the river mouths where the amount of river borne sediment varies significantly. The wave conditions were the same for all their runs and similar to typical coastal settings; the wave orbital velocity and period were $56\,\mathrm{cm\,s^{-1}}$ and 8.6 s, respectively, resulting in $Re_\Delta \approx 1000$. They performed four runs with zero, low, medium and high sediment concentrations. In the low concentration runs, the near-bed sediment concentration was $10\,\mathrm{g\,l^{-1}}$, turbulence was attenuated near the top of the wave boundary layer due to density stratification but turbulence near the bed was unaffected. The maximum wave boundary layer was similar to the zero concentration run ($\delta = 2.8\,\mathrm{cm}$). For the medium concentration run, the near-bed sediment concentration was $50\,\mathrm{g\,l^{-1}}$, turbulence was attenuated in the entire wave boundary layer, wave boundary layer thickness was significantly reduced ($\delta = 0.7\,\mathrm{cm}$) and the velocity profile was very similar to that observed in a laminar flow. However, instabilities were observed near the lutocline and the flow was not completely laminarized. For the high concentration run, the near-bed sediment concentration was $100\,\mathrm{g\,l^{-1}}$ and the velocity structure and wave boundary layer thickness were similar to the medium concentration run. However, there were no instabilities and the flow was completely laminarized.

The present experiments span a similar parameter range to the simulations in Ozdemir et al. (2010a) and so they provide a good test of the model predictions. There are two important differences in the experimental setup; the background sediment concentration in the numerical model experiments is initially prescribed and independent of the wave settings since the model is designed to simulate direct input from rivers. However, the initial sediment conditions are identical in each of our laboratory experiments since the only source of suspended sediment is erosion from the bed and only the wave settings are varied. As a result, the near-bed sediment concentrations are determined entirely by the wave forcing. Also, the model runs consist of a single grain size equivalent to a silt-sized particle. This is expected to lead to a few possible differences in the behavior of the model and experiments, most notably that no bed roughness forms in the model.

There are a number of indications that density stratification is important in suppressing turbulence in our experiments. The wave boundary layer thickness decreases significantly when the flow becomes highly stratified at high Re_{Δ} (Figure 3.3). We also observe that turbulence in upper regions of the wave boundary layer is increasingly attenuated as stratification increases, as observed by Ozdemir et al. (2010a). TKE and its production rate in the wave boundary layer remain relatively constant and significantly lower than the corresponding rough wall values at high Re_{Δ} (Figure 3.12). Although the ripple steepness is significantly reduced in this regime, the bed roughness remains much higher than that in the rough wall experiments and so the turbulence intensity is expected to be as high or higher in the absence of stratification. Thus, these results also suggest that density stratification is effective at suppressing turbulence, by approximately an order of magnitude relative to the rough wall exper-

iments, at high Re_Δ.

In Figure 3.14-b, we show the flux Richardson number (Ri_f) results for the experiments where Ri_f is the ratio of buoyancy flux to TKE production. The buoyancy flux was estimated using a linear eddy diffusivity with the form of $\epsilon_s = \frac{3\sqrt{2}}{10}\kappa u_* z$ (Thorne et al., 2009) and SSC gradients. The coefficient was chosen to take into account the different approaches that this study and Thorne et al. (2009) use in shear velocity estimation. Turbulent shear flows collapse when Ri_f exceeds a critical value, Ri_c, where the energy required to mix sediment over the water column is more than the available kinetic energy provided by the flow (Turner, 1973; Winterwerp, 2006). As a result, the flow becomes more stratified and cannot mix. We observe that Richardson numbers maintain a critical value close to $\frac{1}{4}$ for $Re_\Delta < 550$. This critical value is consistent with the observations of Trowbridge and Kineke (1994) and close to 0.15, the prediction of Turner (1973) for critical flux Richardson number. When $Re_\Delta > 550$, the flux Richardson number exceed the critical value and the flow becomes more stratified. This region likely correspond to the super-saturated conditions described by Winterwerp (2006) where we anticipate a collapse of the concentration profile and of the turbulent flow field.

Despite the strong turbulence suppression, we do not observe any evidence of laminarization of the flow in our data, however. TKE was always significant in the wave boundary layer, even in highly stratified conditions and the wave boundary layer was always much thicker than what would be expected for laminar flow. One likely explanation for this is that there is always some roughness on the sediment bed in the experiments, whereas there is no perturbation except the initial condition in the Ozdemir et al. (2010a) simulations. Perhaps more importantly, the sediment concen-

tration is a result of the wave forcing in the experiments, instead of an independent prescribed parameter. Altering wave conditions can change the concentration threshold required for complete laminarization dramatically. Baas et al. (2009) showed experimentally that doubling the velocity increased the threshold sediment concentration necessary for laminarization eightfold. Although their experiments were not in wavy environments, one can assume that similar trends might be applicable to wave boundary layers. Thus, we expect that the threshold for laminarization will continue to increase as the wave forcing increases, even as the near-bed sediment concentration also increases.

3.5.3 Transitional behavior and the role of fine sand

The results summarized in Figure 3.13 and associated discussion indicate that the flow undergoes a transition when $Re_\Delta \approx 450$; high concentration layers can only form when Re_Δ exceeds this threshold. It is instructive to investigate the dynamics leading to this threshold behavior. Our results support the hypothesis that the threshold near $Re_\Delta = 450$ is a consequence of increases in the concentration of fine sand in suspension, which generate higher near-bed stratification, and decreases in ripple steepness.

In Figure 3.14-c, the average sand fraction in the water column is shown based on the measurements of Lamb and Parsons (2005) who performed very similar experiments in a modified version of the same facility as the present experiments. We show the average sand concentration 10 cmab and the average value below it. The fine sand concentration in the water column is close to zero for low Re_Δ. Above $Re_\Delta = 300$ the amount of sand suspended near the bed increases dramatically until it reaches close to 40% for $Re_\Delta > 450$. This shift results in a higher settling velocity and settling

flux in the high concentration layer, increasing the near-bottom stratification. Also, because turbulence is low above the boundary layer, fine sand particles are primarily limited to the boundary layer, further increasing the stratification, especially at the top of the layer. The intensified stratification likely suppresses turbulence, leading to a feedback that contributes to collapse of the layer thickness.

The sand dynamics may also influence the transition through their impact on ripple formation. Below $Re_\Delta = 450$, the prevalence and influence of ripples indicates that the bed dynamics are dominated by bedload transport. Although the initial sand fraction of the bed was only approximately 10%, Lamb and Parsons (2005) show that winnowing results in sand fractions of 30% to 70% (their Table 1) on the bed for $Re_\Delta < 450$. As Re_Δ increases above 300, more and more sand is entrained into the water column from the bedload layer. This corresponds to a decrease in ripple steepness, which likely contributes to the observed transition.

It is important to note that the dynamics are probably more complicated than the description above due to the complexity of the sediment interactions in clay-silt-sand mixtures. Even when the sediment bed consists primarily of sand the clay fraction can form a cohesive layer around the sand particles, resulting in significant cohesive forces (Van Rijn, 2007). When the sediment bed mixture consists primarily of finer particles, the exact mechanism for sediment suspension is also difficult to characterize since silt particles typically erode as aggregates in the form of chunks rather than individual particles (Roberts and Jepsen, 1998). Visual observations from our experiments are consistent with this description; sediment is initially suspended in chunks, although it is likely that the chunks disaggregate after erosion.

The details of the suspension process can not be fully resolved in our experiments.

However, the observed behavior strongly supports the conclusions that the threshold condition necessary for the generation of high concentration sediment layers is controlled largely by the character of the bed, and especially the fine sand content. It follows that the threshold value of Re_Δ, observed here to be 450, is probably a function of suspended sand concentration. As a result, the threshold conditions necessary for transport of sediment in wave-supported gravity currents will likely vary based on the grain size distribution in the bed deposit.

3.6 Summary and conclusions

1. No high concentration sediment layer forms in Regime I, which corresponds to $Re_\Delta < 450$. In this regime, ripples dominate the bed dynamics, enhancing near-bed turbulence and increasing the wave boundary layer thickness. Turbulent kinetic energy is 2-3 times higher than corresponding rough wall experiments with similar wave conditions.

2. A high concentration sediment layer forms in Regime II, corresponding to $Re_\Delta > 450$. In this regime, the ripple steepness is small and the stratification due to increased fine sand content in suspension suppresses the turbulence. Turbulent kinetic energy is lower than it is in corresponding rough wall experiments with similar wave conditions.

3. The Flux Richardson number maintains a critical value of $\simeq \frac{1}{4}$ for $Re_\Delta < 550$ and the mud layer likely becomes super-saturated for larger Re_Δ values where stratification is intensified.

4. The threshold conditions that differentiate between the low and high Re_Δ regimes appear to result from washout of ripples and the increase in fine sand concentration in the mud layer. The latter results in an increase in settling flux and stratification in the high concentration sediment layer, which may further contribute to the reduction in

the layer thickness. However, other variables that contribute to sediment availability not tested in this study are also likely to be important, such as the degree of bed consolidation.

Chapter 4

RICHARDSON NUMBER

4.1 Introduction

The key to predict the sediment transport mechanism due to WSGCs is to find the interaction of the stress applied to sediment bed and suspended sediment in the water column. This interaction is often addressed with Richardson number. Different forms of Richardson numbers might be applied to these flows. For instance, in order to solve the Navier-Stokes Equations to get the velocity and concentration fields one can close the model with flux Richardson number at the seabed. The bulk Richardson number on the other hand has been used to close the simplified linear Chezy equation model by Wright et al. (2001) and Scully et al. (2002). In most of these models, the assumption of a constant and critical Richardson number is necessary. The constant Richardson number assumption is widely used in atmospheric and oceanic literature. If the Richardson number is smaller than critical value, additional turbulence suspends more sediment resulting in more buoyancy and if the Richardson number is larger than a critical number, decreased turbulence causes the sediment particles to settle and the flow maintains its critical Richardson value. Unfortunately, there are not many field observations of WSGCs due to the unpredictive nature of these flows. Instead, the results of tidally driven currents are mostly used and applied to these currents. One of the studies that is widely used is field observations of Trowbridge and Kineke (1994) from the inner portion of the Amazon continental shelf. They

showed that the vertical transport in fully turbulent stratified flows is controlled by holding a critical gradient Richardson number near $\frac{1}{4}$ for concentration between 1 and 100 $\mathrm{g\,l^{-1}}$ where there is a balance between turbulent mixing and stratification. However, these results corresponded to times when the flow speed 5 m above bottom had a reached a maximum that resulted in the bottom stress actively extracting momentum throughout the near-bottom sediment-laden portion of the flow. These conditions might not be applicable to short period waves in WSGCs where the stress might not be extracted completely from the energetic portion of the wave boundary layer due to the short wave period (seconds) compared to hours-long variation in tidally driven flows.

In this chapter, experimental results for bulk, gradient and flux Richardson numbers are shown. The results include the vertical profiles of these Richardson numbers and averaged values in the mud layer. In addition, scaling for each Richardson number is provided. Finally, the different bulk Richardson numbers than can be used is investigated and discussed and the critical value for each of them is shown.

4.2 Concentration and velocity profiles

Suspended sediment concentrations (SSC) in wave dominated environments have their highest values close to the sediment bed and decreases with distance from bottom to a level where there is a sharp discontinuity of SSC in the water column. The SSC profiles have the form of Equation 4.1 in which C_a is the naer-bed concentration and h is the height of lutocline defined where the concentration is roughly 5% of the close to bed sediment concentration.

$$c(z) = C_a e^{-3z/h} \tag{4.1}$$

We assume a velocity profile shown in Equation 4.2 for the maximum velocity profile during the wave cycle. In this equation, δ is the average wave boundary layer thickness during the phase period. This equation fits well in the wave boundary layer region with the velocity amplitude ratio proposed by Sleath (1970) and Lambrakos (1982):

$$u_{max}(z) \approx \frac{U_{orb}}{\delta} z e^{1-z/\delta} \tag{4.2}$$

4.3 Scaling for Richardson numbers

Three types of Richardson numbers are used in wave-supported gravity currents: bulk, gradient and flux Richardson numbers.

4.3.1 Bulk Richardson number

Bulk Richardson number is typically defined as the ratio of buoyancy force to inertia force and for a continuously stratified flow is:

$$Ri_b = \frac{N_{max}^2 l^2}{U^2} \tag{4.3}$$

in which N_{max}^2 is the maximum buoyancy frequency in different heights, l is the length scale, and U is velocity (Kundu and Cohen, 2008). When sediment is present, the buoyancy frequency is defined as:

$$N^2(z) = -\frac{g}{\rho_0}\frac{\partial c}{\partial \rho} \approx -\frac{gs}{\rho_s}\frac{\partial c}{\partial z} \tag{4.4}$$

in which $s = \frac{\rho_s - \rho_w}{\rho_w}$ is the submerged weight of the sediment in water (1.65 for siliceous material), ρ_s is sediment density (2650 kg/m^3 for silica) and c is the suspended sed-

iment concentration. The maximum buoyancy frequency happens near the sediment bed where the concentration gradient is the largest. Combining Equations 4.1, 4.3 and 4.4 we define bulk Richardson as:

$$Ri_b \approx \frac{gs}{\rho_s}\frac{3C_a h}{U_{orb}^2} \tag{4.5}$$

If one calculates the average value of buoyancy frequency in the lutocline layer, bulk Richardson number is $\frac{1}{3}$ of the Richardson number introduced in Equation 4.5 . Another form that can be used was suggested by Wright et al. (2001) and Scully et al. (2002) where the average buoyancy frequency is defined as $\frac{gs}{\rho_s}\frac{\int_0^h c\mathrm{d}z}{h^2}$ that results in bulk Richardson numbers almost an order of magnitude smaller than the one introduced in Equation 4.5. Notice that this simplification is almost one order of magnitude smaller than the Richardson number defined in Equations 4.3 and 4.5.

Parameter M shows up not only in bulk Richardson number, but also in other forms of Richardson numbers. In Figure 4.1, our experimental results for parameter M have been shown. The lutocline layer forms for wave orbital velocities greater than 25 cm/s and a dilute mix of sediments exists for velocities lower than that. The field observations of Traykovski et al. (2007) in Po Prodelta and experimental work of Lamb et al. (2004) and Hooshmand et al. (2015) in the same wave flume are also shown in this figure and agree relatively well with our results. Although the values are highly scattered (standard deviation of 0.19), they remarkably have an average value of 0.25.

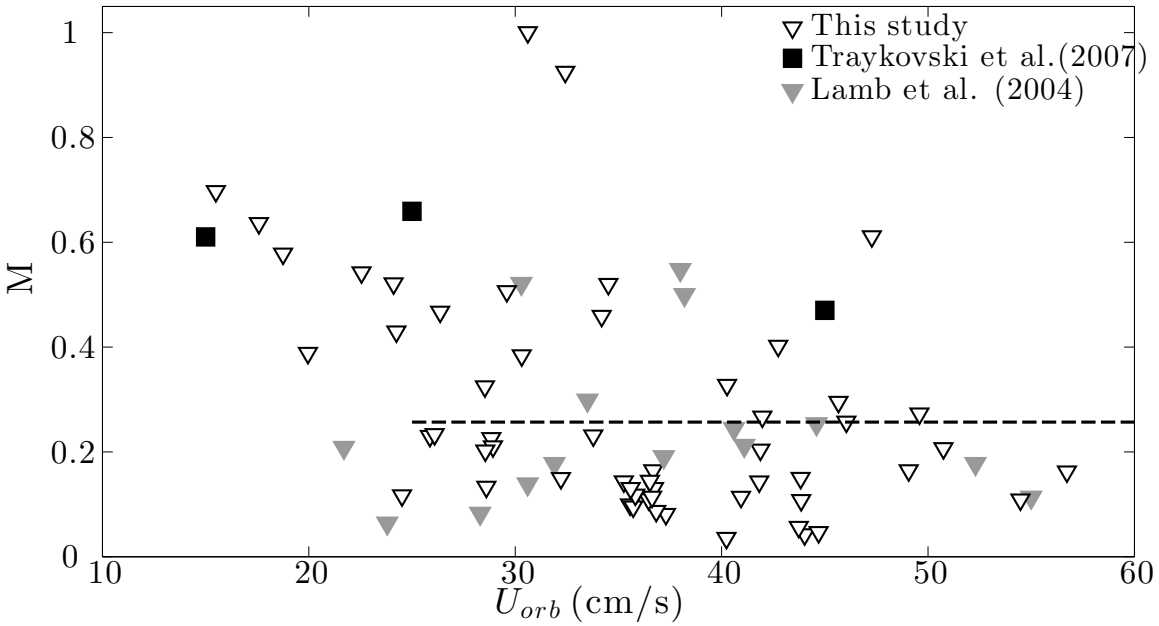

Figure 4.1 Parameter M for this study (white triangles), Lamb et al. (2004) (gray triangles) and Traykovski et al. (2007) (black squares). The dashed line shows the mean value of these three sets of data for wave orbital velocities higher than 25 cm/s when lutocline is formed.

4.3.2 Gradient Richardson number

Gradient Richardson number is defined in terms of local values for stratification and velocity gradients at certain depths (Kundu and Cohen, 2008) and is ratio of the buoyancy frequency to the square of the vertical gradient of the horizontal velocity defined below:

$$Ri_g = \frac{N^2}{(\partial u/\partial z)^2} \approx \frac{gs}{\rho_s}\frac{\partial c/\partial z}{(\partial u/\partial z)^2} \tag{4.6}$$

Gradient Richardson number is defined as a function of vertical distance from the bottom. Combing Equations 4.1, 4.2 and 4.6 results in the gradient Richardson number,

$$Ri_g(z) = \frac{e^{-3z/h}(\delta/h)^2}{e^{2(1-z/\delta)}(1-z/\delta)^2} \times Ri_b \tag{4.7}$$

Although gradient Richardson numbers are meant to be local values, however, if one assumes $\frac{C_a}{h}$ and $\frac{U_{orb}}{\delta}$ for the average SSC and velocity gradients in the lutocline and boundary layer, we can compute average gradient Richardson number.

$$Ri_g = \frac{1}{3}(\delta/h)^2\frac{gs}{\rho_s} \times Ri_b \tag{4.8}$$

4.3.3 Flux Richardson number

Flux Richardson number is the ratio of buoyancy destruction to shear production. Flux Richardson number is extremely hard to directly calculate since we need simultaneous measurements of density and velocity. As a result, we use our estimation for buoyancy to calculate this number. We assume that the average production over the

wave period has the form in Equation 4.9, the coefficients have been derived from fitting experimental data ($a = 8$ and $c = 5$)

$$P(z) = au_*^2 \frac{U_{orb}}{\delta}[\frac{z}{\delta} - (\frac{z}{\delta})^2]e^{(1-cz/h)} \tag{4.9}$$

The buoyancy flux can be estimated with an eddy diffusivity assumption as shown below:

$$B(z) = \frac{gs}{\rho_s}\epsilon_s \frac{\partial c}{\partial z} \tag{4.10}$$

If we combine Equation 4.9 and 4.10, we have production as a function of z:

$$Ri_f(z) = \frac{\alpha\kappa(z/\delta)(\delta/h)^2 e^{-3z/h}}{a\sqrt{C_d}(z/\delta - (z/\delta)^2)e^{1-cz/\delta}} \times M \tag{4.11}$$

in which eddy diffusivity is $\epsilon_s = \frac{3\sqrt{2}}{10}\kappa u_* z$ based on Thorne et al. (2009) experiments with fine sand.

If we integrate buoyancy and production over the lutocline height separately and form an average flux Richardson number, we will have the flux Richardson number as in Equation 4.12. In this equation, the integral of production over the lutocline is scaled as $P = \beta u_*^2 U_{orb}$ and $\beta = 0.35$ for our experiments.

$$Ri_f = \frac{\alpha\kappa\frac{e^3-4}{9e^3}}{\beta\sqrt{C_d}}\frac{gs}{\rho_s} \times M \tag{4.12}$$

4.4 Vertical structure of Richardson numbers

Vertical structure of wave-supported gravity currents are dictated by very short wave periods and wave boundary layers are in the range of few centimeters. However, the suspended sediments exist above the wave boundary layer in the lutocline layer due to

turbulence leakage from the wave boundary layer, likely in the form of the transport term in the TKE budget (Lamb et al., 2004). As a result, although there is suspended sediment outside of the wave boundary layer, we focus on the vertical structure of the gradient Richardson numbers inside this layer.

In Figure 4.2, the vertical structures of different gradient Richardson numbers for a surface wave event in the Po prodelta recorded by Traykovski et al. (2007) have been shown. The parameters of this event (called HC1 in their paper) are wave orbital velocity $45\,\mathrm{cm\,s^{-1}}$, wave period 8 s, mean wave boundary layer 3.5 cm, lutocline height of 10 cm and near-bed sediment concentration of $50\,\mathrm{g\,l^{-1}}$. The vertical structure of flux and gradient Richardson numbers vary in the wave boundary layer, starting with very small values near the bottom and approaching values close to one near the wave boundary layer height. The gradient Richardson number is basically the ratio of frequency of buoyancy - that is how fast sediment particles come back to their initial positions when slightly disturbed - to velocity gradients. For instance, in the HC1 event in the Po prodelta the time scale for buoyancy is around 0.6 seconds from Equation 4.4. Considering that the wave period is just 10 seconds, the flow is not uniform and varies in the frequency time scale. As a result, the time scale of the wave events might not be appropriate for calculating gradient Richardson numbers. The same argument might be applicable to flux Richardson number since the production and buoyancy destruction are not in the same phase. The bulk Richardson number derived from Equation 4.3 is around 0.45 and seems to be the most reliable Richardson number for this event.

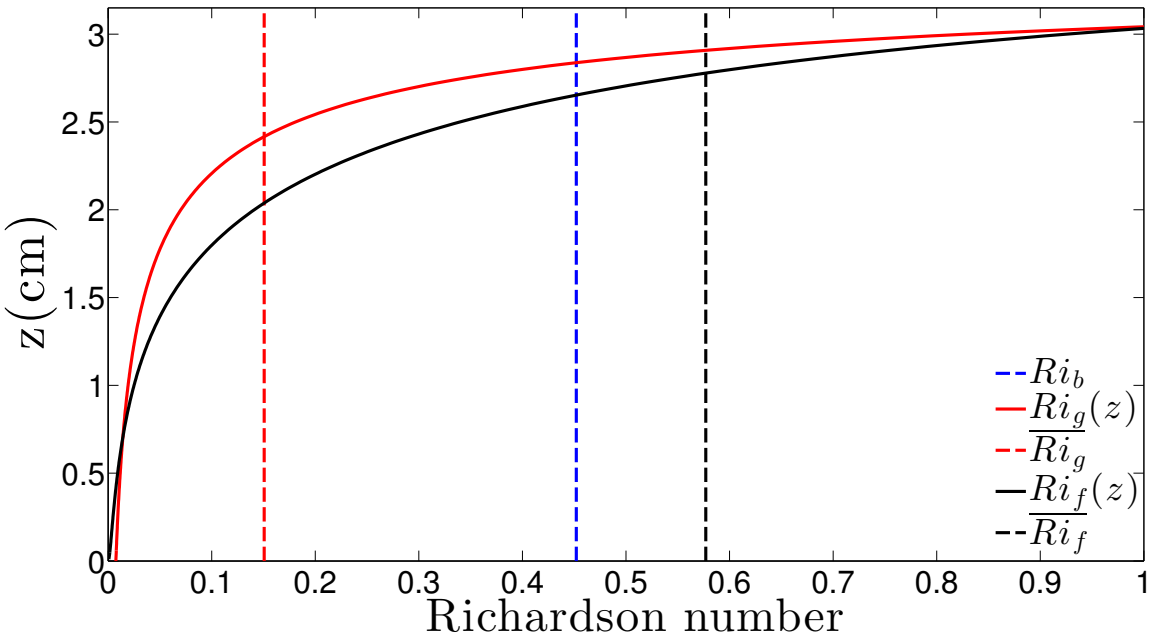

Figure 4.2 The vertical structure of different Richardson numbers for the wave event of HC1 in the Po prodelta from Traykovski et al. (2007). The dashed lines show the average values and solid lines show Richardson numbers as a function of distance from the bottom

4.5 Comparison and discussion

Based our calculations and the models of Wright et al. (2001) and Scully et al. (2002), the bulk Richardson number has a critical value if and only if $C_a h \propto U_{orb}^2$, i.e. close to bed sediment concentration and lutocline should both increase as the wave orbital velocity increases. As shown in Chapter 3, while C_a increases as wave orbital velocity increases, the hight of lutocline decreases due to turbulence suppression because of stratification. As a result, bulk Richardson numbers might not reach a critical value although their mean value was $\frac{1}{4}$ (Figure 4.1) when lutocline is formed.

The Gradient Richardson number is believed to maintain a critical value so that turbulence is enhanced if $Ri_g < Ri_{cr}$ and turbulent mixing is suppressed if $Ri_g > Ri_{cr}$. If gradient Richardson number is greater than $\frac{1}{4}$, linear stability is guaranteed. However, the flow is not necessarily unstable if $Ri_g < \frac{1}{4}$ somewhere in the flow. In other words, $Ri < \frac{1}{4}$ is a necessary but not sufficient condition for instability (Kundu and Cohen, 2008). Since Ri_g is easier to calculate in the field, it has been widely used to evaluate the relationship between stratification and bottom shear stress in stratified flows. Trowbridge and Kineke (1994) showed that Ri_g is highly scattered but having mean of $\frac{1}{4}$ for steady tidal boundary layers high above the bottom (5 m) when SSC is between $1 - 100\,\mathrm{g\,l^{-1}}$ as in the Amazon river continental shelf. While critical values can be applied for tidal currents, the small WBL in WSGCs in addition to its short wave period makes Ri_g an order of magnitude smaller than those values depending on how the layer thickness is defined.

Turbulence collapses if the flux Richardson number is higher than a critical number assumed to be 0.15 (Turner, 1973; Winterwerp, 2002). In the under-saturated suspension region ($Ri_f < Ri_{cr}$) a balance exists between production and buoyancy

destruction. For super-saturated suspension ($Ri_f > Ri_{cr}$) turbulence starts to collapse and vertical mixing is suppressed (Winterwerp, 2006). The flux Richardson number increases vertically in the wave boundary layer monotonically for the average SSC profile fit equation. For different wave conditions, as it was shown in Chapter 3, the flux Richardson number might maintain a critical value close to $\frac{1}{4}$ until the turbulence starts to collapse around $Re_\Delta = 600$. For Reynolds numbers bigger than this value, the flux Richardson numbers starts to increase since the production is suppressed and the flow might be super-saturated (Winterwerp, 2006).

Chapter 5

MODELING WAVE-SUPPORTED GRAVITY CURRENTS

A series of analytical models have been developed to investigate sediment transport due to WSGC in continental shelves. These models are based on a linearized form of the Chezy equation (van Kessel and Kranenburg, 1996; Traykovski et al., 2000) where the friction force is due to both across-shelf velocity and wave velocities (Wright et al., 2001; Scully et al., 2002; Traykovski et al., 2007). The unknown sediment-induced pressure gradient in these models can be replaced with a Richardson number concept with the value of $\frac{1}{4}$, based on observations of Trowbridge and Kineke (1994) in the Amazon River continental shelf, and across-shelf velocity can be predicted. In addition, a number of numerical simulations have been done to test factors such as supply of unconsolidated fine sediment (Hsu et al., 2009), turbulence suppression (Ozdemir et al., 2010a) and settling velocity (Ozdemir et al., 2011), and these have been incorporated into the dynamics of these currents. However, there is no dataset of experimental observations with detailed measurements of WSGCs to test these models.

In this chapter, we show experimental results for down-slope velocity due to gravity for different slopes. The results include detailed measurements of velocity and suspended sediment concentration profiles. We build an analytical model for predicting velocity across the shelf using the Navier-Stokes Equations and predict across-shelf velocity for turbulent and laminar conditions. Finally, we show how the model pre-

dictions compare to the experimental results.

5.1 Theoretical development

The motions of wave-supported gravity currents in the absence of an external current are often modeled using Navier-Stokes Equations. The simplified Navier-Stokes Equation in which non-linear convective acceleration terms are simplified is shown in Equation 5.1

$$\rho\frac{\partial u}{\partial t} = \frac{-\partial p}{\partial x} + g\rho\sin(\theta) + \frac{\partial}{\partial z}(\mu\frac{\partial u}{\partial z} - \rho\overline{u'w'}) \tag{5.1}$$

where $\rho(z)$ is the density of the mud layer, $\sin(\theta) \approx \theta$ is the bottom slope, μ is the viscosity and $-\overline{u'w'}$ is Reynolds stress per unit mas. Outside of the wave boundary layer, Reynolds stress and velocity gradient are zero and velocity field is horizontal in the form of $u_\infty = U_{orb}\sin(\omega t)$, where U_{orb} is wave orbital velocity, $\omega = \frac{2\pi}{T}$ is wave frequency and T is wave period. The density and sediment concentration of turbid water are related with $\rho = \rho_w + (1 - \frac{\rho_w}{\rho_s})C$ in which s is submerged weight of sediment defined by $s = \frac{\rho_s - \rho_w}{\rho_w}$ where ρ_s and ρ_w are densities of sediment particles and water. Converting the densities to concentration and using the velocity condition outside of the wave boundary layer, the pressure gradient term can be replaced with other terms that results in:

$$\frac{\partial(u - u_\infty)}{\partial t} = \frac{\partial}{\partial z}(\nu\frac{\partial u}{\partial z} - \overline{u'w'}) + \frac{s}{\rho_s}C(z)g\sin(\theta) \tag{5.2}$$

We assume that $\frac{s}{\rho_s}C(z) << 1$ which is a valid assumption for sediment concentrations smaller than 160 $\mathrm{g\,l^{-1}}$. For zero slope conditions, the general form of solution to Equation 5.2 is in the form of $u(z,t) = A(z)U_{orb}\sin(\omega t + \phi)$ where ϕ and $A(z)$ are

phase lead and velocity defect function inside of the wave boundary layer. For laminar flow, using no slip condition at the bottom and uniform sine wave outside of the wave boundary layer, ϕ and $A(z)$ have analytical solutions, as shown below (Nielsen, 1992):

$$\begin{aligned} A(z) &= \sqrt{1 + e^{-2a} - 2e^{-a}\cos a} \\ \phi(z) &= \arctan\left(\frac{\sin a}{e^{a} - \cos a}\right) \\ a &= \frac{z}{\sqrt{2\nu/\omega}} \end{aligned} \tag{5.3}$$

However, turbulence always exists in the field and one cannot use laminar conditions except for smooth wall experiments in the lab or when the turbulence is completely suppressed due to stratification (Ozdemir et al., 2010a). We assume that $u(z,t) = u_0(z,t) + u_g(z)$ has two components where $u_0(z,t)$ is the solution to zero slope condition and u_g is the across shelf velocity due to gravity. If we apply $u(z,t)$ to Equation 5.2, many terms are simplified since we already know that $u_0(z,t)$ satisfies the no slope condition. Since $u_g(z)$ is not a function of time, the PDE is simplified to an ODE and with using eddy viscosity assumption for Reynolds stress, $\overline{-u'w'} \approx \nu_T \frac{\partial u}{\partial z}$, we will have:

$$[\nu + \nu_t]\frac{\partial^2 u_g}{\partial z^2} + \frac{\partial \nu_t}{\partial z}\frac{\partial u_g}{\partial z} = -\frac{s}{\rho_s} g \sin(\theta) C(z) \tag{5.4}$$

The suspended sediment concentrations in our experiments have an exponential form similar to experimental results of Lamb et al. (2004) and field observations of Traykovski et al. (2007). Thus, we define SSC profiles as $C(z) = C_a e^{-\beta z/h}$ in which h is the height of lutocline. Based on our laboratory results, $\beta = 3$ is a good fit to SSC profiles in which $C(h) \approx 0.05 C_a$. Notice that we do not see a sharp discontinuity in sediment concentration profile as observed by Traykovski et al. (2000). We make the

following assumptions that will be tested in the following sections. These assumptions are: 1) eddy viscosity has the linear form of $\nu_T = \alpha\kappa u_* z$ where κ is Von Karman's constant ($\kappa = 0.41$) and α is a coefficient, 2) kinetic viscosity is negligible compared to the eddy viscosity via scaling, 3) suspended sediment concentration profiles are the same for no slope and tilted conditions. In section 5.1.1, we investigate the results of the suspended sediment concentration changes after adding slope velocities to the model. After applying these assumptions, we get the following ODE:

$$z u_{g,zz} + u_{g,z} = -\frac{sg\theta}{\rho_s \alpha\kappa u_*} C_a e^{-\beta z/h} \tag{5.5}$$

where we need two boundary conditions to solve the ODE. We choose gravity driven velocity, u_g, to be zero at the height of lutocline (h) and at z_0 in which z_0 is the roughness of the bed. The bottom roughness, z_0, can be derived from $z_0 = k_b/30$ where $k_b = 27.7\eta(\eta/\lambda)$ (Grant and Madsen, 1982). In this equation, η and λ are ripple height and wavelength. The solution to Equation 5.5 with these two boundary conditions is:

$$u_g(z) = \frac{sg\theta C_a h}{\beta\rho_s\alpha\kappa u_*}[\mathrm{Ei}(\frac{-\beta z}{h}) - C_1 \ln(\frac{z}{h}) - \mathrm{Ei}(-\beta)] \tag{5.6}$$

in which Ei is the exponential integral function defined as $\mathrm{Ei}(x) = \int_{-x}^{\infty} \frac{e^{-t}\mathrm{d}t}{t}$ and C_1 is:

$$C_1 = \frac{\mathrm{Ei}(-\beta) - \mathrm{Ei}(\frac{-\beta z_0}{h})}{\ln(h/z_0)} \tag{5.7}$$

where C_1 ranges from 0.55 to 0.75 for our experimental results with a mean of 0.63. We can a use constant bulk Richardson number formulation which is often used in

the field where a balance is assumed between the kinetic force and buoyancy force, as shown in Equation 5.8

$$\mathrm{Ri}_{cr} = \frac{B}{U_{orb}^2} \tag{5.8}$$

where B is the depth integrated buoyancy of the mud layer and is defined by:

$$B = \frac{gs}{\rho_s} \int_0^h c(z)\mathrm{d}z \tag{5.9}$$

For our proposed suspended sediment concentration profile, we get $B \approx \frac{C_a g s h}{\beta \rho_s}$. Using the critical Richardson number concept, the drag coefficient $C_d = (\frac{u_*}{U_{orb}})^2$, and $\alpha = 1$ for eddy viscosity model, we will have:

$$u_g(z) = \frac{\theta \mathrm{Ri}_{cr} U_{orb}}{\kappa\sqrt{C_D}} [\mathrm{Ei}(\frac{-\beta z}{h}) - C_1 \ln(\frac{z}{h}) - \mathrm{Ei}(-\beta)] \tag{5.10}$$

The average value for u_g can be derived by integrating Equation 5.10. Using $z_0 \approx 0.8\,\mathrm{mm}$, based on our experimental results, we will have:

$$\overline{u_g} = \frac{(C_1 - 0.3)\theta \mathrm{Ri}_{cr} U_{orb}}{\kappa\sqrt{C_D}} \tag{5.11}$$

5.1.1 Variable SSC profile with slope

In section 5.1, it was assumed that SSC profile would not change when the slope is added to the model. In this section, we do not use this assumption consider changing the suspended sediment concentration using $U_{orb} + u_g$ instead of U_{orb} in Richardson number. In other words, we add to the shear stress to account for added SSC due to across shelf velocity. The modified ODE is:

$$zu_{g,zz} + u_{g,z} + \frac{\beta\theta \mathrm{Ri}_{cr}}{h\kappa\sqrt{C_D}} e^{-\beta z/h} u_g = -\frac{\beta\theta \mathrm{Ri}_{cr} U_{orb}}{h\kappa\sqrt{C_D}} e^{-\beta z/h} \tag{5.12}$$

There is no analytical solution to this ODE. In Section 5.3, it will be shown that the numerical solution to this ODE is just 5% different from solution in Equation 5.10. As a result, it is concluded that solutions in Equations 5.10 and 5.11 are accurate enough and there is no need to use Equation 5.12 to predict wave-supported gravity currents.

5.1.2 Laminar solution

Density stratification can suppress the turbulence in the mud layer to the point of pure laminarization (Winterwerp, 2006; Ozdemir et al., 2010a). As it was shown in Chapter 3, a complete laminarization was not observed in the flume experiments, however, turbulence suppression was seen. Thus, it is of value to investigate the across shelf velocity in laminar conditions. In this section we investigate what the solution is when we have pure laminar flow due to strong stratification. We apply $u(z,t) = u_{0,l}(z,t) + u_g(z)$ to Equation 5.2 where $u_{0,l}(z,t)$ is the laminar solution to no-slope condition as described in Equation 5.3. Notice that the Reynolds stress term is zero since we assume the flow is laminar. We can simplify the PDE to an ODE as shown below:

$$u_{g,zz} = -\frac{s}{\rho_s \nu} C(z) g\theta \tag{5.13}$$

Using the same boundary conditions for velocity as we used in Equation 5.5, we get the solution for laminar conditions as follows

$$u_g(z) = \frac{sg}{9\rho_s}\frac{C_a h^2}{\nu}\theta(-e^{-3z/h} + 1 - (1 - e^{-3})\frac{z}{h}) \tag{5.14}$$

Notice that we cannot use the critical bulk Richardson number here since a complete laminarization happens. Furthermore, viscosity significantly increases with higher suspended sediment concentrations. The new viscosity can be derived from $\nu = \nu_w(1 + \alpha_r C^{\beta_r})$ (Ross, 1988) in which $\alpha_r = 1.68$ and $\beta_r = 0.346$ have been determined for a kaolinite in fresh water (Engelund and Zhaohui, 1984). The average velocity can be derived from the equation below:

$$\overline{u_g} \approx \frac{sg}{54\rho_s}\frac{C_a h^2}{\nu_w(1 + \alpha_r(\frac{C_a}{3})^{\beta_r})}\theta \tag{5.15}$$

5.1.3 Fixed SSC in the mud layer

Wave supported gravity currents have been often reported to have a mixed layer of SSC inside the mud layer, with a sharp discontinuity called a lutocline. Although our experimental results and some field observations (Traykovski et al., 2007) show an exponential form in SSC, other studies indicate a possibility of a mixed layer with constant SSC profiles(Cacchione et al., 1995; Ogston et al., 2000). If we use a constant SSC profile in the form of $C(z) = \bar{C}$ for $z < h$, using Equation 5.4m we will have

$$u_g(z) = \frac{sg\theta\bar{C}}{\rho_s\alpha\kappa u_*}(h - z_0)\left[\frac{h - z}{h - z_0} + \frac{\ln(\frac{z}{h})}{\ln(\frac{h}{z_0})}\right] \tag{5.16}$$

for u_g profile. If we assume that $h - z_0 \approx h$, then combining Equations 5.8 and 5.9, we will have:

$$u_g(z) = \frac{\theta \mathrm{Ri}_{cr} U_{orb}}{\kappa\sqrt{C_D}}\left[\frac{h - z}{h - z_0} + \frac{\ln(\frac{z}{h})}{\ln(\frac{h}{z_0})}\right] \tag{5.17}$$

The average u_g inside the lutocline layer will be:

$$\overline{u_g} = \left[\frac{1}{2} - \frac{1}{\ln(\frac{h}{z_0})}\right] \frac{\theta \mathrm{Ri}_{cr} U_{orb}}{\kappa\sqrt{C_D}} \tag{5.18}$$

5.1.4 Fixed SSC under lutocline with laminar conditions

A mixed layer of SSC with high concentrations can possibly suppress the turbulence in the mud layer and laminaries the flow. In this case, we use the same SSC profiles as Section 5.1.4 but with laminar conditions. Therefor, $u_g(z)$ can be found as below:

$$u_g(z) = \frac{s\bar{C}g\theta}{2\rho_s\nu} z(h-z) \tag{5.19}$$

The average u_g inside the lutocline layer will be:

$$\overline{u_g} = \frac{sg}{12\rho_s} \frac{\bar{C}h^2}{\nu_w(1+\alpha_r\bar{C}^{\beta_r})}\theta \tag{5.20}$$

5.2 Experiments

We performed 32 experiments with different slopes and wave conditions. These experiments have been summarized in Table 5.1

5.3 Experimental results

The shear stress due to waves suspended the unconsolidated sediment particles in a mud layer above the sediment bed. In Figure 5.1, our SSC experimental results for four different experiments with different velocity settings have been shown. The SSC profiles have an exponential form similar to observations of Traykovski et al. (2007) and an SSC profile in the form of $C(z) = C_b + C_a e^{-\beta z/h}$ has been fitted to them as

Table 5.1 Experiments parameters

	Experiments															
	1	2	3	4	5	6	7	8	9	10	11	12	13	14	15	16
$\theta(^\circ)$	0	1	2	3	0	1	2	3	0	1	0	0	2	1	3	0
$U_{orb}(\mathrm{cm\,s^{-1}})$	25	24	25	24	32	33	32	31	42	42	40	29	29	29	29	37
$T(\mathrm{s})$	12.5	12.5	12.4	12.6	9.9	9.8	9.8	9.7	7.7	7.6	7.8	10.8	10.8	10.9	10.8	8.4
$u_*(\mathrm{cm\,s^{-1}})$	0.8	0.9	0.8	1.1	1.1	1.1	1	1.2	1	1.1	1.1	1	1.1	1	1.2	1.2
$\delta(\mathrm{cm})$	3.4	4.2	5.2	4.6	3.4	2.8	3.4	2.5	3.3	2.8	3.7	3.4	3.1	2.8	3.3	2.5
	17	18	19	20	21	22	23	24	25	26	27	28	29	30	31	32
$\theta(^\circ)$	2	1	3	0	1	1	3	2	3	3	3	0	0	2	1	3
$U_{orb}(\mathrm{cm\,s^{-1}})$	37	37	37	37	36	35	36	37	37	36	36	41	44	44	45	44
$T(\mathrm{s})$	8.4	8.4	8.4	8.4	8.5	8.5	8.4	8.4	8.4	8.5	8.5	7.4	6.6	6.6	6.6	6.7
$u_*(\mathrm{cm\,s^{-1}})$	0.9	1.1	1.1	1.5	1.8	1.1	1	1	1.1	1	1.2	1.3	1.1	0.9	1	0.8
$\delta(\mathrm{cm})$	2.5	2.3	2.5	2.1	2.6	3	2.8	2.4	2.3	2.2	2.6	2.9	1.5	1.5	1.9	2.8

a result where the lutocline, h, is defined where $C(z) = 0.05C_a$. Notice that we do not observe a mixed mud layer with a sharp discontinuity on top of this layer. The difference in the form of SSC profiles might be mostly due to events other than waves that happen in the field, while in the lab, we are separating out the effects due to waves. In addition, we do have a background concentration in the water column, C_b, that can potentially change the SSC profile in the mud layer. Finally, the sediment particles that we use for our experiments are artificially made and we lack natural grain interaction and biological processes that are present in the field.

The down-slope velocity (u_g) can be calculated by averaging the horizontal velocity over the wave period. However, we have other background flows in the wave flume mostly due to the pump action. As a result, we subtract the background flow of zero-slope condition from slope experiments. This zero-slope background velocity that is

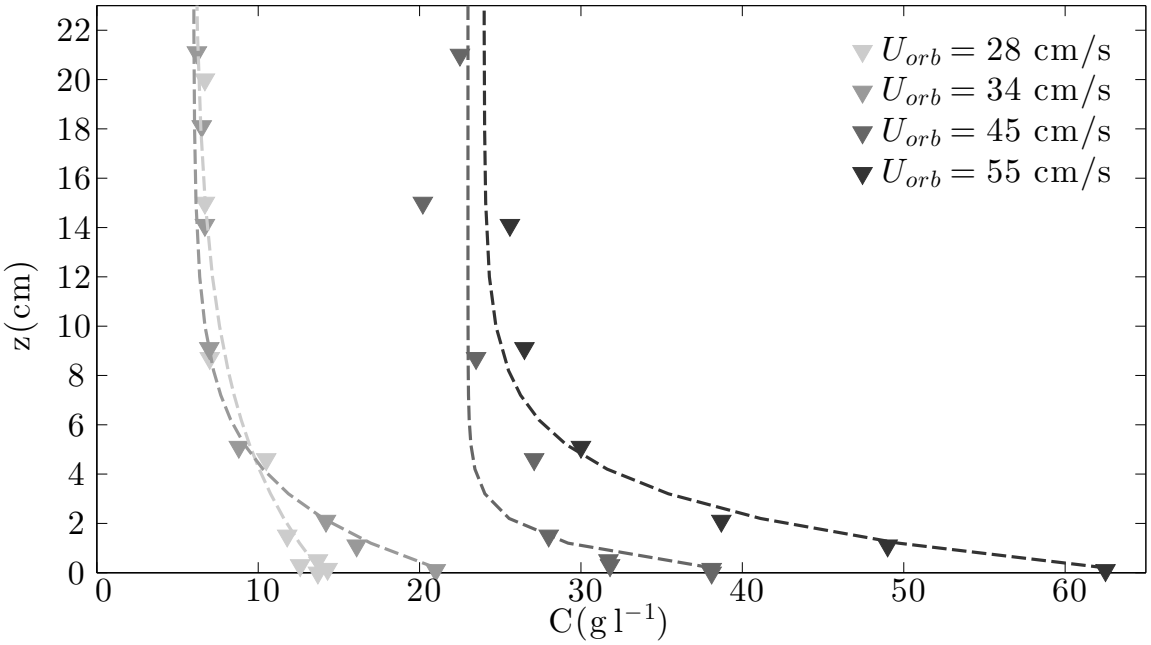

Figure 5.1 Suspended sediment concentration profiles for four experiments: $U_{orb} = 28, 34, 45 \,\&\, 55$ cm s^{-1}. The symbols show the raw SSC data from siphons and the dashed lines show the fit to the data in the form of $C(z) = C_b + C_a e^{-\beta z/h}$

subtracted varies with wave conditions. The residual velocity is considered to exist as a result of gravity.

In Figure 5.2, u_g, Reynolds stress ($-\overline{u'w'}$) and suspended sediment concentrations for slopes 1°, 2° and 3° for three runs with similar wave orbital velocity and wave frequencies. In the left column, u_g is shown where it increases as the slope increases. The u_g profiles have zero velocity near the bottom, reach a maximum in the lutocline layer and go to zero at the top of the mud layer. Outside of the mud layer, the velocity should be zero. The middle column shows SSC profiles where changing the slope does not affect them since the wave conditions are the same in the three experiments. Finally, in the right column, averaged Reynolds stress profiles at the maximum velocity phase ($\pi/2$) is shown where we can see that the changes in Reynolds stress due to slope is insignificant.

In Figure 5.3, the changes of u_g, $\overline{u'w'}$ and SSC vs. slope haven been shown for all experiments. For each slope, there is variation in the values which is due to different wave conditions. The box shows the middle 50-th percentile and the horizontal line is the median. The two vertical lines on the top and bottom of the box show maximum and minimum values for each slope. In Figure 5.3-a, the changes of averaged Reynolds stress is shown for different slopes. There is no obvious change or trend in Reynolds stress values with increasing slope. In Figure 5.3-b, the average SSC in the mud layer is shown where again no obvious change or trend due to changing slopes is seen. In Figure 5.3-c, changes in u_g due to slope is shown where a monotonically increasing pattern is observed. We will show that this increase matches well with our theoretical prediction.

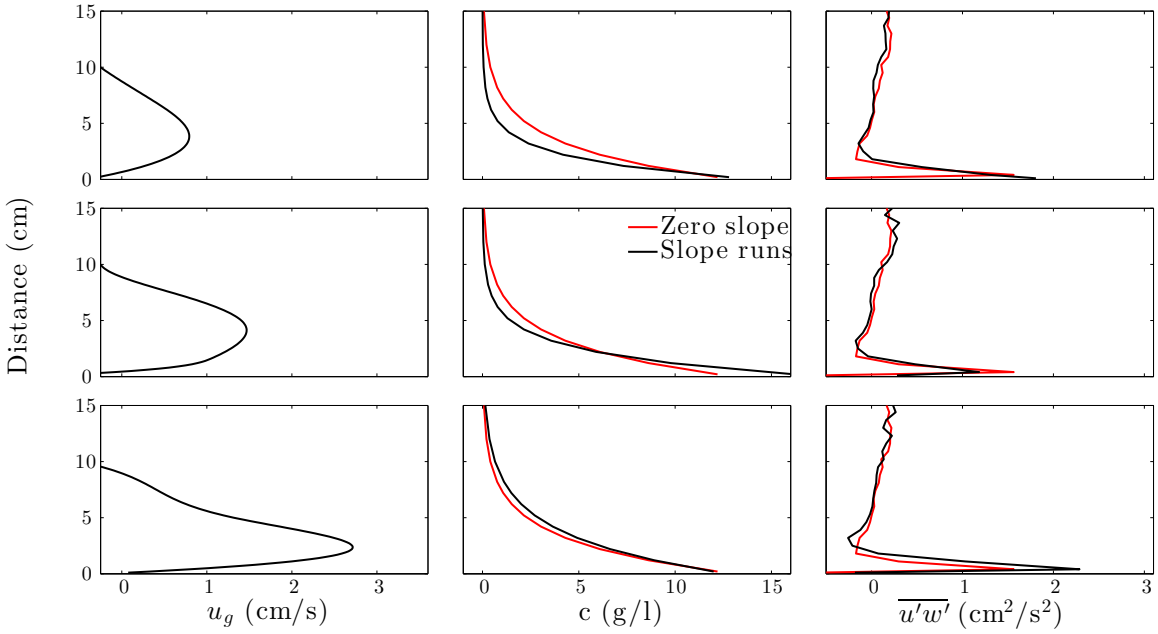

Figure 5.2 u_g (left column), SSC (middle column) and Reynolds stress (right column) for slopes 1° (upper row), 2° (middle row) and 3° (lower row) for three experiments with $U_{orb} = 40$ cm s^{-1} and $T = 8$ s

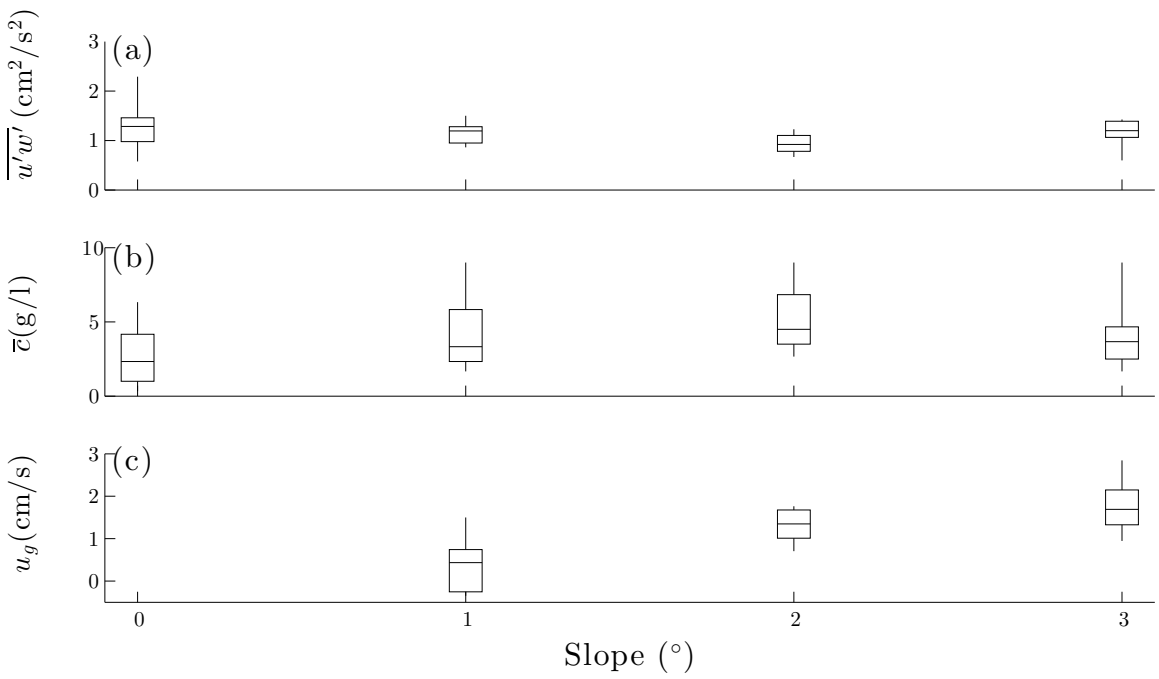

Figure 5.3 (a) Reynolds stress, (b) averaged SSC in the mud layer and (c) u_g for different slopes. The vertical lines in the box plot show maximum and minimum values for each slope. The box shows the 50% percentile and the horizontal line in the box plot is the median value for each slope.

5.4 Comparison to models

In Figure 5.4, u_g is shown for an experiment with $U_{orb} = 35$ cm s^{-1} and $T = 8$ s with slope of 3°. As mentioned before, we find this velocity by averaging the velocity over the wave period and subtracting the zero slope runs. The experimental profile shown in Figure 5.4 (black triangles) are created from five experiments with the same wave conditions and have been averaged to make a smooth profile. The net transport velocity is close to zero near the sediment bed, reaches its maximum in the lutocline layer at 3 cm distance from the bottom and finally reaches zero at the top part of the mud layer (12 cm for this experiment). The predicted net transport velocity for Equation 5.10 (solid black line) matches well with this profile although it reaches its maximum at 2 cm above the bed rather than 3 cm. We can see that u_g profile from solving Equation 5.12 matches experimental results only slightly better (5%). As a result, we can conclude that the assumption for having the same shear stress for varying slopes is a good assumption and we will use Equation 5.10 for the rest of the results in this paper.

In Figure 5.5, the average transport velocity for all experiments vs. the model is shown. For the model, we have used average values for drag coefficient ($C_d = 0.001$), and $Ri_{cr} = \frac{1}{9} \times 0.25$ and $C_1 = 0.7$ based on our experimental results. For the experiments, the average velocity is derived from averaging velocity profiles in the mud layer. The model and experiments show a good agreement although the model tends to underestimate the transport velocity especially at the higher predicted velocities related to higher slope experiments.

In Figure 5.6, the ratio of u_g to U_{orb} is shown for different slopes. This ratio is proportional to slope and therefor we expect to see a linear trend. Although the

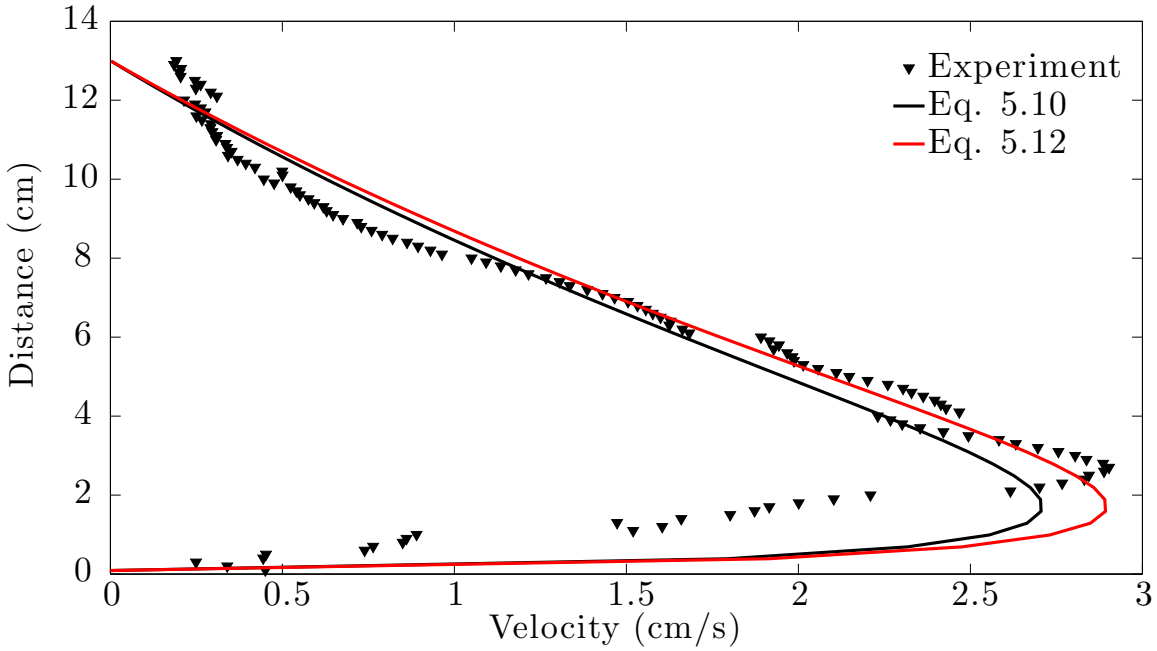

Figure 5.4 Net transport velocity profile for $U_{orb} = 35$ cm s^{-1}, $T = 8$ s and $\theta = 3°$. Experimental results (black triangles), predicted u_g profile from Equation 5.10 (solid black line), and predicted u_g profile from Equation 5.12 (solid red line)

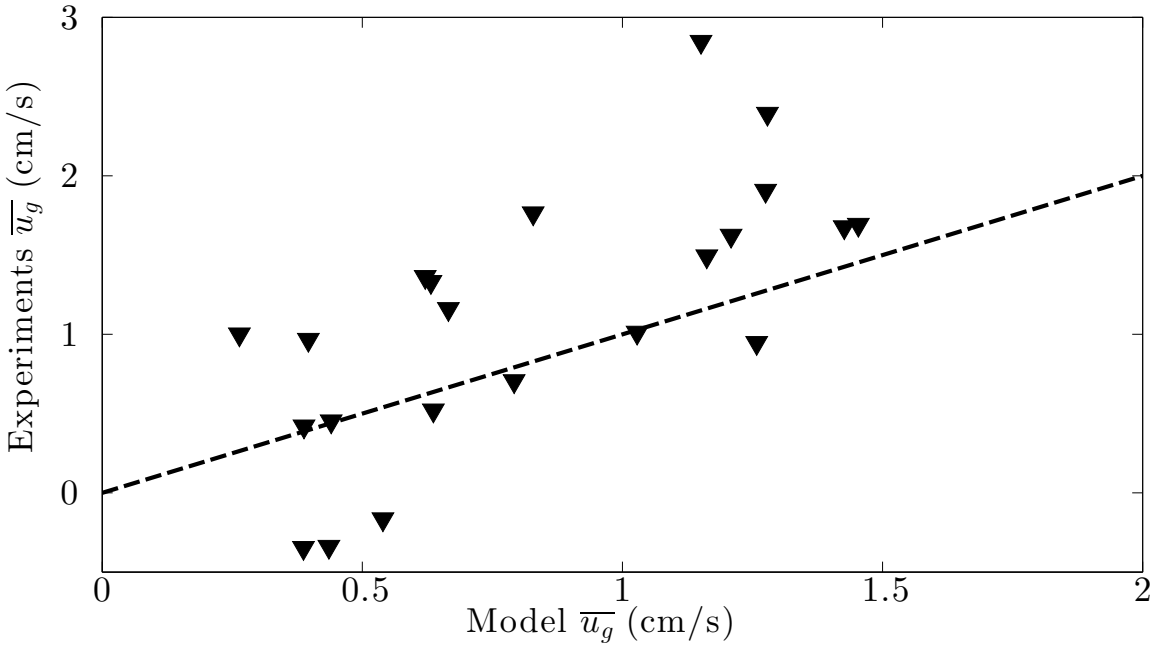

Figure 5.5 Average u_g in the lutocline for model (Equation 5.11) and experiments where the dashed line shows 1-1 ratio. The R^2 value is 0.32.

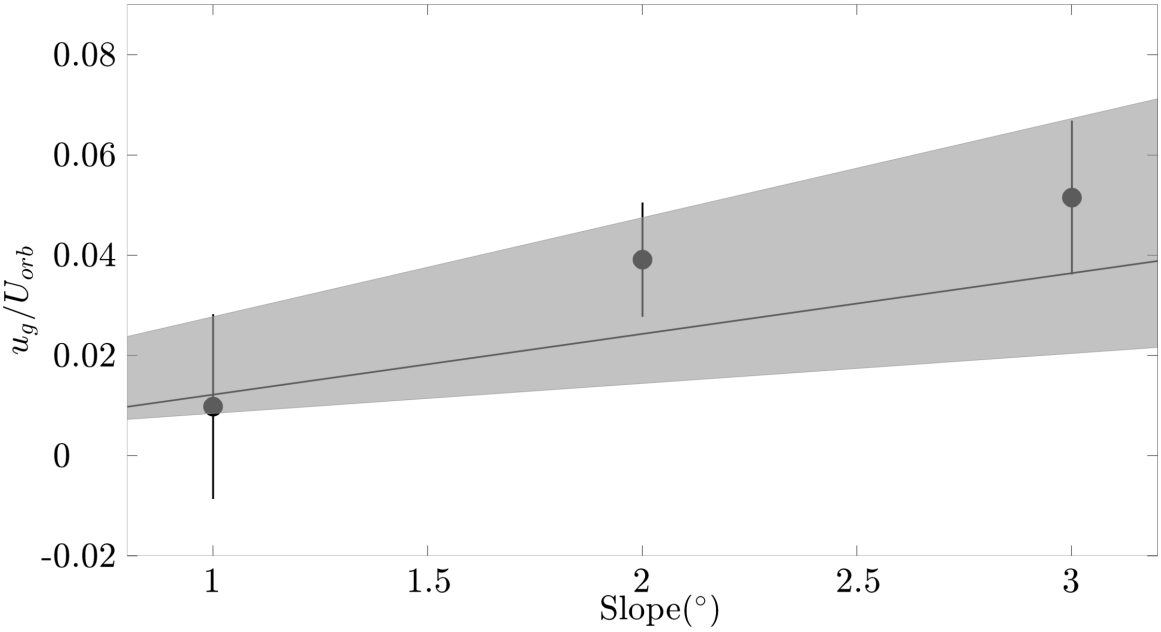

Figure 5.6 Non-dimensionalized across shelf velocity to wave orbital velocity for different slopes. The vertical lines show the standard deviation for each slope. The gray area shows 95% confidence interval for the model prediction where the lower region uses $Ri = 0.2$ and $C_1 = 0.55$ and upper region uses $Ri = 0.35$ and $C_1 = 0.75$

Richardson number averages to $\frac{1}{9} \times 0.25$, it has a exponential distribution and the 95% confidence interval is $\frac{1}{9} \times [0.2, 0.35]$. The two values determine the upper bound and lower bound of the predicted areas for $\frac{u_g}{U_{orb}}$ and the average of experimental results are within this area although they show a good amount of variation (vertical lines show the standard deviation for each slope).

5.5 Discussion

In this chapter, the details behind the analytical model for predicting down-slope velocity due to waves was described. The are several assumptions about turbulence and concentration properties in wave-supported gravity currents that were used to

derive the analytical model. In this section, these assumptions are discussed and validated.

5.5.1 Eddy viscosity model

Numerous eddy viscosity models have been developed for oscillatory boundary layers, divided into two basic models: time-varying and time-independent. Time-independent eddy viscosity models can be a simple linear from ($\nu_t = \kappa u_* z$) as suggested by Grant and Madsen (1979) to more complicated models such as linear exponential models ($\nu_t = \kappa u_* z e^{-z/\Delta}$) where Δ is a length scale dependent on wave boundary layer height (Hsu and Jan, 1998; Absi, 2001; Puleo and Mouraenko, 2003; Absi, 2004). Time-varying eddy viscosity models can include more complicated models such as time-varying linear-exponential forms and $k-\epsilon$ or $k-\omega$.

In Figure 5.7 we show velocity profiles and wave boundary layer heights for different eddy viscosity models in comparison with experimental results. In Figure 5.7-a, the wave boundary layer height, defined the location of maximum velocity from the bed, is shown for different models over a wide range of wave orbital velocities. It seems that the linear eddy viscosity model performs similar to $k-\epsilon$ model, although both of them have errors in capturing the experimental wave boundary layer. The error can be due to ripples, stratification and other features that are not captured with models. In Figure 5.7-b, velocity profiles at maximum velocity phase for a case of $U_{orb} = 35\,\mathrm{cm\,s^{-1}}$ and $T = 8.8\,\mathrm{s}$ has been shown. The experimental data show a thick wave boundary layer, around 2 cm. The linear eddy viscosity model captures the location of the wave boundary layer peak, however, it underestimates the velocity at the wave boundary layer.

Overall, the linear eddy viscosity model seems to perform well for modeling Reynolds

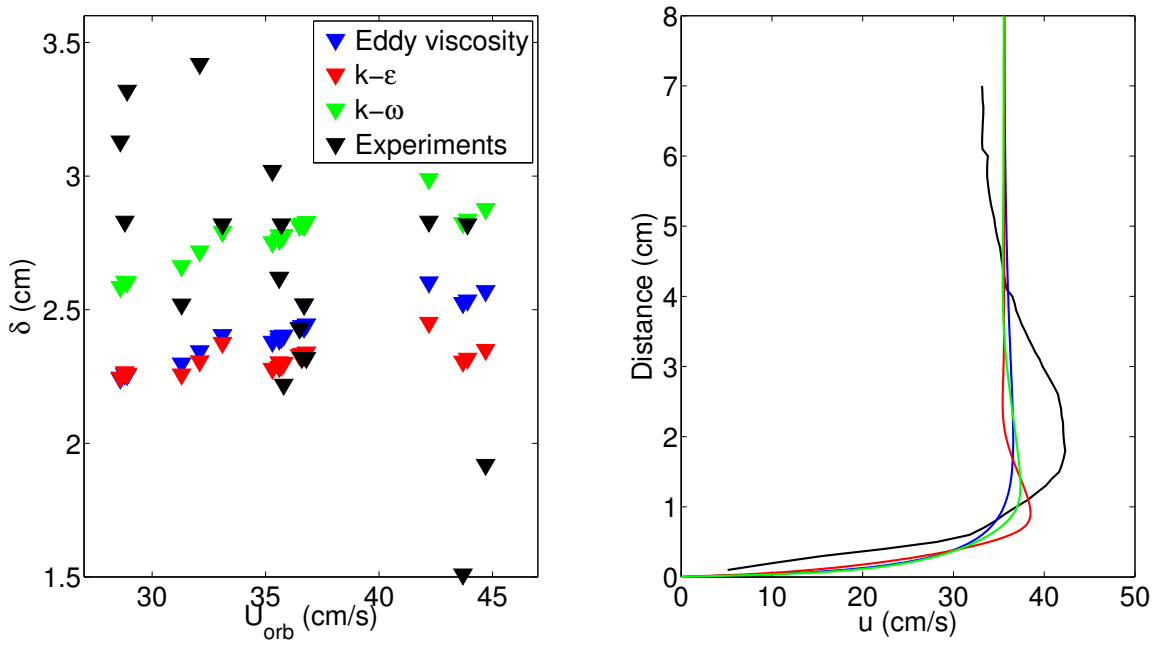

Figure 5.7 (a) Maximum wave boundary layer for different experiments and (b) velocity profiles at maximum velocity phase for experimental (black), $k-\epsilon$, $k-\omega$ and linear eddy viscosity for the same wave conditions.

stress in comparison with other more sophisticated eddy viscosity models and was used as the eddy viscosity model in this study.

5.5.2 Turbulent and laminar conditions.

The stratified mud layer in wave supported gravity currents can suppress the turbulence and possibly laminarizes the flow completely (Ozdemir et al., 2010a). The reduced turbulence might cause the suspended sediment particles to settle down and make this situation temporary. However, hindered settling can maintain the sediment particles in suspension for a while. As shown before in Section 5.1, the physics behind turbulent and fully laminarized WSGS is significantly different resulting in different

down-slope velocities.

In Figure 5.8, the solutions for laminar and turbulent conditions are shown as derived in Section 5.1. In this plot, we are not using the Richardson number concept and are assigning different SSC profiles inside the mud layer, as C_{avg} in the x-axis varies. The values that were used in this figure are from field observations of Traykovski et al. (2007) in the Eel River continental shelf where $U_{orb} = 56\,\mathrm{cm\,s^{-1}}$ and $\theta = 0.0003$. The height of lutocline, h, is assumed to be 10 cm. The bottom and top gray areas show turbulent and laminar conditions where the lines are associated with $h = 10\,\mathrm{cm}$ and the upper and lower limits correspond to $h = 15\,\mathrm{cm}$ and $h = 5\,\mathrm{cm}$ as the lutocline height changes based on different SSC inside the mud layer. We observe that the values are an order of magnitude different from turbulent to laminar conditions. If the laminar conditions happen for high SSC inside the mud layer, sediment particles can potentially move across the shelf due to waves with high velocity as observed by Traykovski et al. (2000) and Ogston et al. (2000).

5.5.3 SSC profiles

The suspended clay, silt and fine sand particle due to surface waves form a mud layer on the vicinity of the sediment bed. In this study, we observe that the SSC profiles inside this mud layer have an exponential form. This observation is consistent with experimental observations of Lamb et al. (2004), Lamb and Parsons (2005), and field observations of Traykovski et al. (2007). However, a series of field studies such as observations of Traykovski et al. (2000), Cacchione et al. (1995), and Hale and Ogston (2015) report a more uniform SSC layer and sharp discontinuity in the water column. These differences might be due to different instrumentation used in the field and experiments, other currents and sediment interactions in the field such as hindered

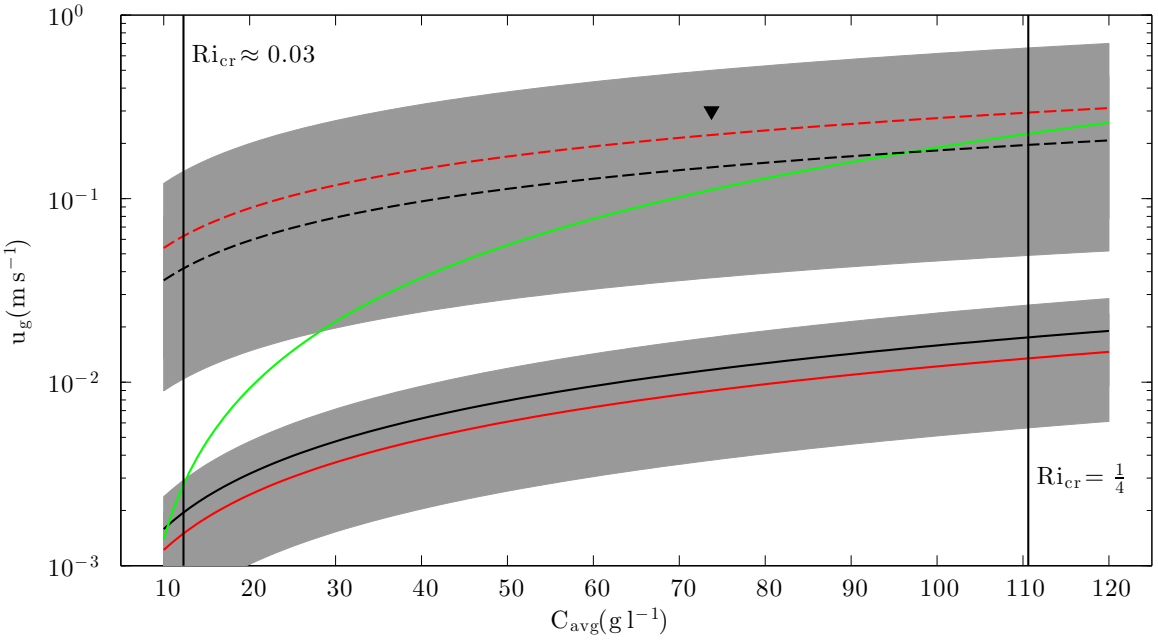

Figure 5.8 Across shelf velocity prediction for $U_{orb} = 56\,\mathrm{cm\,s^{-1}}$ and $\theta = 0.0003$ from field observations of Traykovski et al. (2007) on Eel river continental shelf. The X-axis shows the average SSC inside the mud layer. The black lines show the exponential SSC form and the red lines show the uniform SSC inside of the mud layer. The solid and dashed lines show the turbulent and laminar solutions. In all of 4 lines, $h = 10\,\mathrm{cm}$. The bottom and top gray areas show the turbulent and laminar solution range for $h = 5\,\mathrm{cm}$ and $h = 15\,\mathrm{cm}$. The green line is an imaginary transition from turbulent to laminar conditions.

settling or flocculation or the background concentrations we had in our wave flume that does not exist in the field. In Section 5.1 we derived the solution for both cases of exponential or fixed SSC for laminar and turbulent conditions. In Figure 5.8, we show these results in black and red lines for exponential and fixed SSC profiles where solid lines and dashed lines correspond top turbulent and laminar conditions. We observe that based on our analytical solutions, u_g derived from both cases are very similar.

5.6 Summary and conclusions

In this chapter, the results for sloped experiments were presented and the effects of different slopes on down-slope velocities were investigated. The down-slope velocities can go up to $3\,\mathrm{cm\,s^{-1}}$ for relatively high wave orbital velocities and incline of 3°. An analytical model was introduced based on the Navier-Stokes equations for predicting down-slope velocity due to waves where the bulk Richardson number was assumed to have a critical value of 0.03 based on the observed concentration profiles. The model captures the experimental results of down-slope velocity well. The solutions of the model includes laminar and turbulent conditions with exponential or constant SSC profiles in the mud layer. Finally, a schematic was proposed that predicts laminar and turbulent regimes based on Reynolds number for any wave event.

Chapter 6

COMPARISON WITH PREVIOUS STUDIES

6.1 Introduction

During the past two decades numerous studies have been conducted on wave-supported gravity currents. The studies include field observations, analytical models, numerical simulations and experimental studies. While in all of these studies the importance of WSGCs in cross-shelf sediment transport have been emphasized, there are differences in observed velocity, turbulence, suspended sediment concentrations, expected values for down-slope velocity due to these currents and sediment transport.

In this chapter we compare our experimental results and analytical model results to the data from the field, numerical simulations and other analytical models. The differences and similarities between these observations are explained and the reasons behind behind them provided. At the end, the limitations of the experimental works are stated.

6.2 Velocity profiles

Velocity profiles in WSGCs have three regions as was mentioned in Chapter 3: wave boundary layer, overshoot and free stream velocity regions. There are two parameters that can be used in order to compare velocity profiles for different studies. The first one is the wave boundary layer thickness, as defined in Chapter 3, at the height of maximum velocity. The second parameter is the ratio of maximum velocity to free

stream velocity (overshoot ratio). Notice that both of these values change during the wave period and here their maximum values during the wave period is considered for comparison purposes.

In Figure 6.1, the velocity profiles for sediment bed and rough wall experiments from this study and numerical simulations of Ozdemir et al. (2010a) are shown. Ozdemir et al. (2010a) performed numerical simulations for $U_{orb} = 56\,\mathrm{cm\,s^{-1}}$ and $T = 8.6\,\mathrm{s}$ ($Re_\Delta = 1000$) for different suspended sediment concentrations in the mud layer. They reported laminar conditions in the wave boundary layer for $C = 50 - 100\,\mathrm{g\,l^{-1}}$ and somewhat turbulent flow for $C < 50\,\mathrm{g\,l^{-1}}$. They used the stokes length, $\tilde{\Delta}= \sqrt{\frac{2\nu}{\omega}}$, for non-dimensionalizing depth where $\Delta = 1.6\,\mathrm{mm}$ for their simulations. They reported maximum wave boundary layer height of $2\tilde{\Delta}$ and $7\tilde{\Delta}$ (3 mm and 11 mm) for laminar and turbulent conditions in their experiments. Based on their results, the overshoot ratio was 5% and 7.5% for turbulent (low SSC) and laminar (high SSC) cases. As it can be seen in Figure 6.1-a, in our experiments these values were much higher. The wave boundary layer heights in almost all experiments were bigger than 20 mm and the overshoot velocity could go up to 13%. These may be due to the effects of ripples in these experiments since the numerical simulations do not take the ripple effects into account and simulations are conducted on a smooth sediment bed. Hay et al. (2012a) report similar overshoot velocity ratios to these experiments from their experimental studies on a gravel bed (roughnesses closer to rippled sediment beds). As a result, the roughness might be playing an important role. However, the effects of roughness might decrease as the ripples disappear for higher velocities when the flow switches dynamics from Regime I to Regime II, as mentioned in Chapter 3.

The across shelf velocity due to waves was addressed in Chapter 5 where each

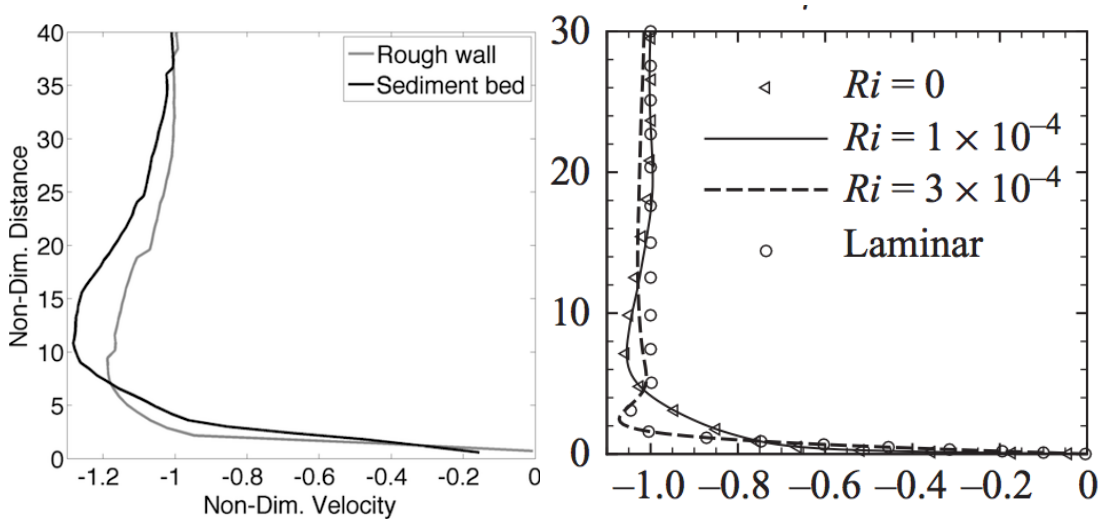

(a) This study (b) Ozdemir et al. (2010a)

Figure 6.1 Non-dimensionalized velocity profiles for (a) this study and (b) Ozdemir et al. (2010a). Distances has even non-dimensionalized to Stokes Length scale ($\sqrt{\frac{2\ni}{\omega}}$). Velocities have been non-dimensionalized to free stream velocity.

profile is derived from averaging velocity time-series over time. In Figure 6.2, the across shelf velocities for field and experimental observations are shown. The left and middle panels show cross-shelf velocity in the Po prodelta from observations of Traykovski et al. (2007) where they observed across-shelf velocities up to $5\,\mathrm{cm\,s^{-1}}$ for a shelf slope of 0.1° (red curves). In this study, however, similar across shelf velocities were only observed for much higher tank slopes around 3°. The shape of the profiles were also different and the experimental down-slope velocities reach around $2-3\,\mathrm{cm}$, while in the field, this maximum happens at $+10\,\mathrm{cmab}$. One of the reasons behind this difference might be that in this study waves are the only factor in maintaining a sediment gravity flow layer and the down-slope velocity induced by the layer is purely a function of waves. However, other events such as external currents exist

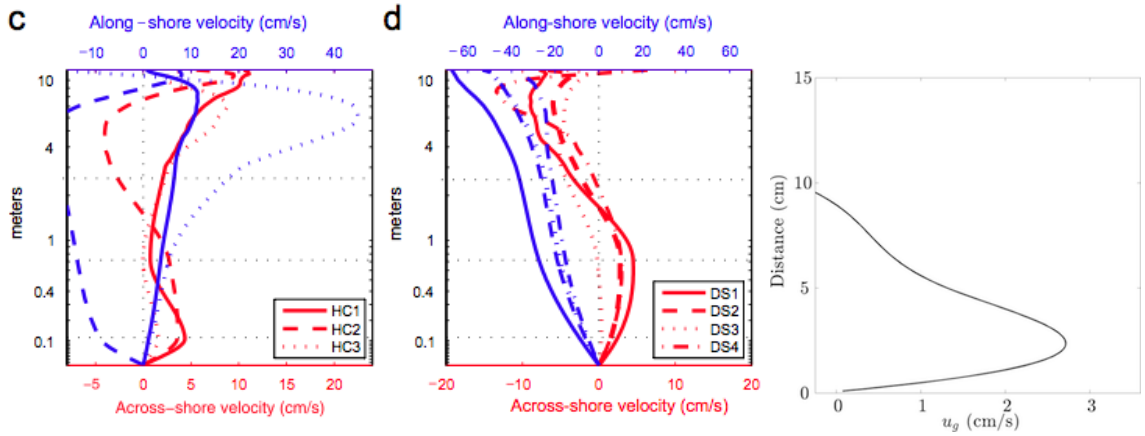

(a) Traykovski et al. (2007) (b) This study

Figure 6.2 Across shelf velocities for (a) Traykovski et al. (2007) in the Po prodelta ($\theta = 0.1°$, $U_{orb} = 15 - 45\,\mathrm{cm/s}$) and (b) this study ($\theta = 3°$, $U_{orb} = 45\,\mathrm{cm/s}$).

in the field that might cause the difference. Furthermore, most of our experimental measurements were carried out inside of the mud layer ($z < 10\,\mathrm{cm}$) while the field measurements were mostly above or at the upper limit (typically+30 cmab).

6.3 Reynolds stress and shear velocity

There are three methods that can be used to estimate shear velocity (u_*) for oscillatory currents: 1) direct estimates of the horizontal components of turbulent shear stress, 2) law of wall, and 3) estimates of shear using wave friction factor (f_w) (Sherwood et al., 2006). These three approaches result in different estimates of shear velocity in the wave boundary layer.

In our experiments, we used temporal maximum of vertically averaged Reynolds stress to estimate shear velocity in the wave boundary layer. The magnitude of average Reynolds stress inside of the wave boundary layer is consistent with experimental observations of Lamb et al. (2004) and Hay et al. (2012a). This method uses active

components of turbulent shear stress and shows the effects of both ripples and density stratification. As a result, this method might result in higher shear velocity in Regime I (ripple dominated) and lower shear velocity in Regime II (stratification dominated) compared to other methods.

In field observations, it is impossible to measure Reynolds stresses inside of the wave boundary layer due to limitations in measuring instruments and the episodic nature of WSGCs. As a result, wave friction factor is often used to estimate shear velocity. In this method, shear velocity can be estimated from:

$$u_* = a\, U_{orb} \tag{6.1}$$

where a is a parameter that can be estimated from $a = \sqrt{0.5 \exp\left(5.5(\frac{r_h}{A})^{0.2} - 6.3\right)}$ similar to Equation 3.3 in Chapter 3. The exponential component in this equation is wave friction factor.

In Table 6.1, shear velocity calculations from direct measurements of $u'w'$ and estimates from wave friction factor (f_w) based on Equation 6.1 is shown for both rough wall and sediment bed experiments along with the field observations of Traykovski et al. (2007) in the Po Prodelta. Different roughnesses have been used for rough wall (roughness of glued sand) and sediment bed experiments (roughness due to ripples) for f_w method. Overall, shear velocity estimates using wave friction factor is larger than direct measurements of $u'w'$. Observations of Traykovski et al. (2007) show higher shear stress during similar wave conditions in the Po Prodelta. One reason might be the wave friction factor that is used in this dissertation (Equation 6.1) versus $f_w = 0.04(\frac{U_{orb}}{\omega_r k_n})^{-0.025}$ used by Traykovski et al. (2007). For instance, rough wall experiments in this study will have shear velocity of 3.5 - 5.7 cm/s if the latter

Table 6.1 Shear velocity from experiments and the field

Study	Location	$U_{orb}(\mathrm{cm\,s^{-1}})$	T (s)	$u_*\,(\mathrm{cm\,s^{-1}})$	Method
This study (RW)	Wave flume	25 - 45	6 - 10	0.7 - 1.1	$\overline{-u'w'}$
This study (SB)	Wave flume	25 - 45	6 - 10	1	$\overline{-u'w'}$
This study (RW)	Wave flume	25 - 45	6 - 10	1.8- 2.9	f_w
This study (SB)	Wave flume	25 - 45	6 - 10	2.8	f_w
Traykovski et al. (2007)	Po Prodelta	25 - 45	8	5.2 - 7.5	f_w

wave friction factor is used. Most importantly, there might be external currents in the field that might contribute to more shear stress for similar wave conditions.

6.4 Concentration profiles

Unconsolidated sediment particles become suspended due to the shear stress may from surface waves and may form a mud layer in WSGCs. While some studies result in a high density mud layer, there are differences in the shape of SSC profiles in different studies. The two most common forms that are reported are constant SSC inside the mud layer with a sharp discontinuity in SSC in water column called lutocline and an exponential SSC profile with the maximum SSC near the sediment bed.

In this study, exponential SSC profiles were observed and SSC profile was formulated as $C(z) = C_a e^{-3z/h}$ where C_a is near-bed SSC and h is the defined lutocline despite the lack of a sharp discontinuity in SSC. Based on this definition, SSC at the lutocline is approximately $0.05C_a$. This experimental result is consistent with experimental observations of Lamb et al. (2004) and Lamb and Parsons (2005). Traykovski et al. (2007) also reports exponential SSC profiles for WSGCs in the Po prodelta although there was a lack of detailed measurement of SSC close to the sediment bed

and some extrapolation was applied to estimate the SSC profile. On the other hand, several field observations suggest completely mixed SSC profiles inside the mud layer. For example, Traykovski et al. (2000) implies such observations of WSGCs in the Eel River continental shelf. Cacchione et al. (1995) reports smiler observations in Amazon subaqueous deltas. More recently, Hale and Ogston (2015) reports mixed SSC in the mud layer during wave events in Waipaoa River shelf in New Zealand. Note that measuring SSC is very challenging in the field due to periodic nature of the waves and is often conducted using Acoustic Backscatter Sensors (ABS). Correction algorithms often applied to convert sensor data to SSC are sensitive to unknown sediment particle size that may not be well constrained.

In Figure 6.3, the observations of wave-supported mud layers from Waipaoa River Shelf in New Zealand have been shown (Hale and Ogston, 2015). The SSC data in this figure is from ABS field measurements and the ABS has been calibrated in the lab. As can be seen, before and after the wave event, there is a very thin mixed layer of SSC near the sediment bed and the SSC profile have an exponential form above this region. However, during the wave event, this mixed mud layer grows in size and reaches to 15 cm and the exponential SSC profile on top disappears. This is different from experimental observations in the wave flume. The difference might be due to the artificial sediment that is used in the tank that does not have the same particle interaction as the natural sediment particles in salinity-zero experimental settings. The other factor might be that waves are the only driving factor in the present experiments whereas there are other driving factors in the field that might contribute to this difference.

In Figure 6.4, experimental results of SSC profiles from this study and field ob-

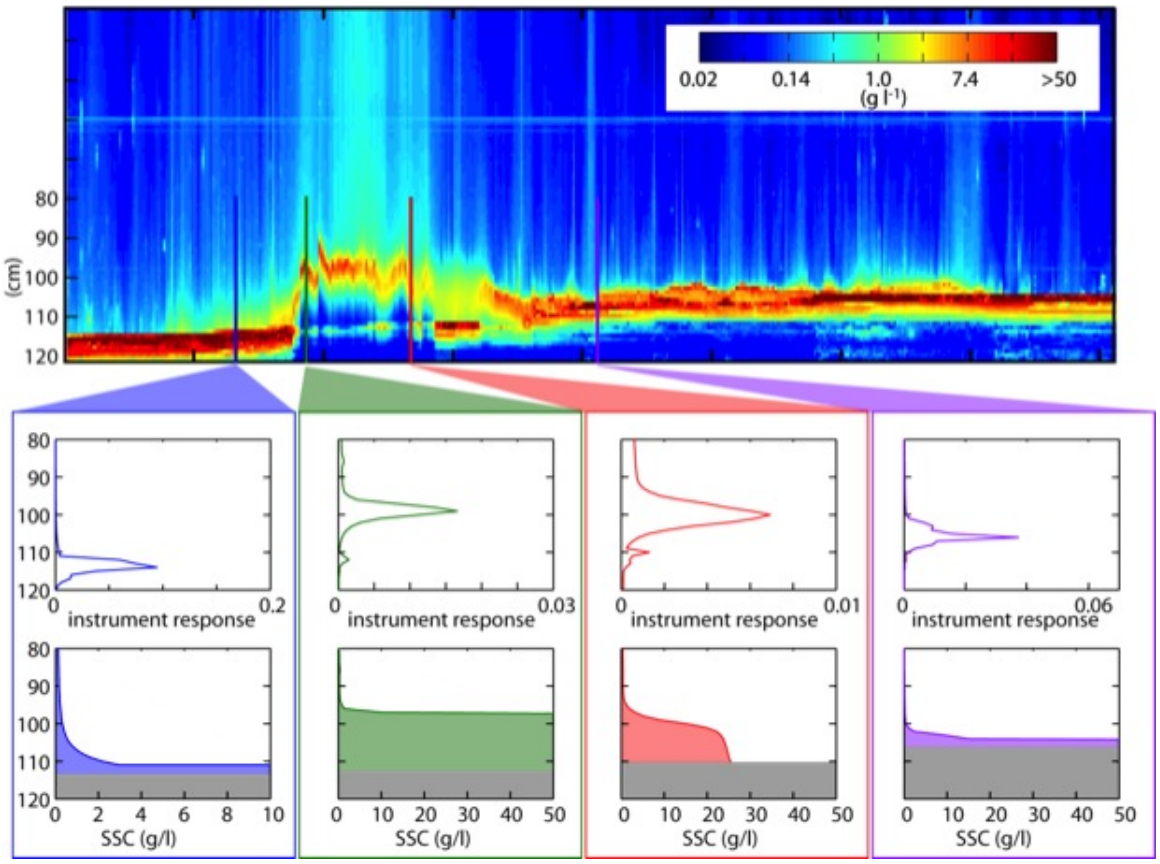

Figure 6.3 SSC profiles from ABS data in Waipaoa River Shelf in New Zealand from Hale (2014)

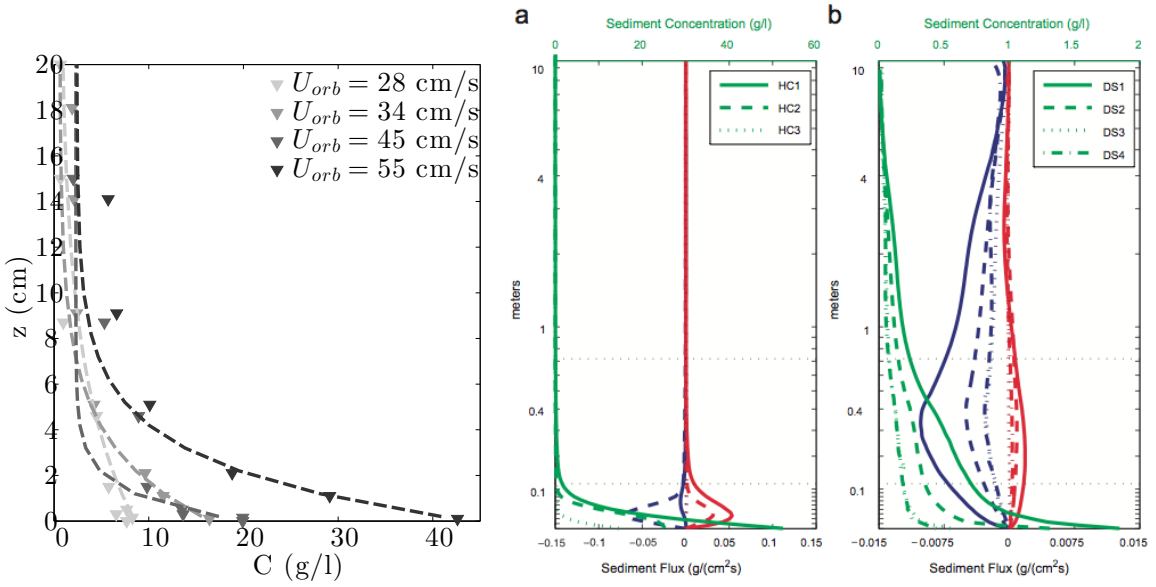

(a) This study (b) Traykovski et al. (2007)

Figure 6.4 SSC profiles for (a) this study and (b) Traykovski et al. (2007) from Po Prodelta

servations of Traykovski et al. (2007) in the Po prodelta have been shown. In Figure 6.4-a, the experimental results for four different wave orbital velocities are shown where the SSC profiles have an exponential form. In Figure 6.4-b, SSC profiles from SSC observations using ABS data is shown where SSC increases monotonically close to sediment bed. Note that some extrapolation has been performed on these data near the sediment bed.

6.5 Comparison of the current models

In Chapter 5, an analytical model was proposed that estimates across-shelf velocity due to surface waves in WSGCs. The results of that model are compared to analytical models of Wright et al. (2001) and Scully et al. (2002) in this section. Then, the

assumption behind these models are provided and compared. In Section **??**, the results are compared to previous field studies in Waipaoa River Shelf in New Zealand (Hale et al., 2014).

6.5.1 Assumptions behind the models

Both models use the same parameters in predicting average across-shelf velocity in the mud layer (u_g). These four parameters are:

- Wave orbital velocity (U_{orb})
- shelf slope (θ)
- Drag coefficient (C_D)
- Critical Richardson number (Ri_{cr})

The analytical model in this study is derived from the Navier-Stokes equations. Several assumption are made to arrive at the final model result. These assumptions are:

1. The density of fluid outside of WBL is water density
2. Linear eddy viscosity model is valid
3. Velocity due to gravity is time-independent
4. SSC does not change for non-zero conditions
5. Viscosity is negligible in the presence of turbulence
6. SSC profile is exponential
7. $Ri_{cr} \approx 0.03$
8. $C_D = 0.001$

While some of these assumptions are tested and verified for experimental settings, some of these assumptions such as exponential form of SSC profiles might not hold for the field conditions. The analytical model of Wright et al. (2001) and Scully et al. (2002) makes the following assumptions:

1. Linearized Chezy equation is a valid force balance for WSGC
2. $Ri_{cr} \approx \frac{1}{4}$
3. $C_D = 0.001$

The model introduced in this study predicts velocities two orders of magnitudes smaller than prediction from Wright et al. (2001) and Scully et al. (2002). Here we try to address this difference. Both models predict the average velocity in the mud layer (u_g) in the form Equation 6.2 in the absence of external currents,

$$u_g = bU_{orb} \tag{6.2}$$

where $b = \frac{0.35\theta Ri_{cr}}{\kappa\sqrt{C_d}}$ for our model is proposed in Chapter 5 and $b = \frac{\theta Ri_{cr}}{C_d}(1 - \frac{\theta Ri_{cr}}{C_d})^{-0.5}$ for Scully and Wright's model. One of the major differences between the two models is the critical Richardson number that is used. The critical Richardson number in this study is almost one order of magnitude smaller than $\frac{1}{4}$ as explained in detail in Chapter 4. Considering that $u_g \propto R_{cr}$, this results in one order of magnitude difference. The other order of magnitude of difference is more fundamental and is the result of different analytical approaches in deriving the models.

In Figure 6.5, the sensitivity of both models to critical bulk Richardson number and bottom drag coefficient have been shown for Site S60 from Scully et al. (2002) data. The slope of site S60 is 0.0043. For a wave orbital velocity of $U_{orb} = 40\,\mathrm{cm\,s^{-1}}$,

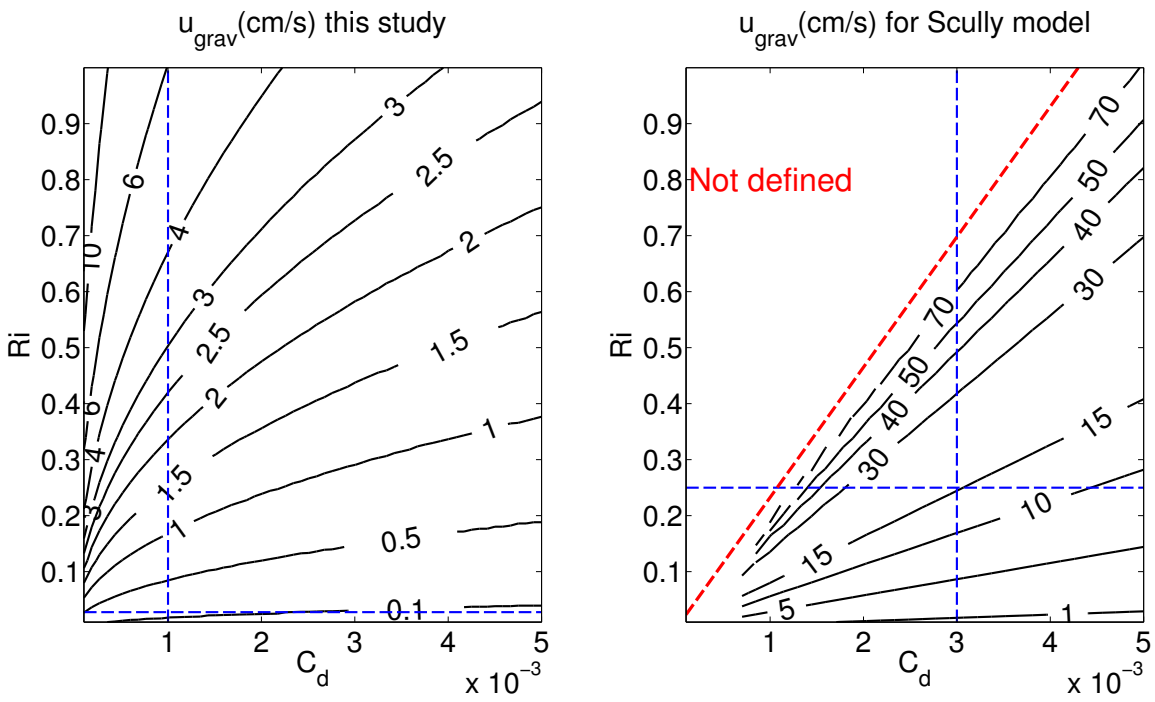

Figure 6.5 Contours for across-shelf velocity due to wave supported gravity currents for different drag coefficients and bulk Richardson numbers for $U_{orb} = 40$cm/s and $\tan(\theta) = 0.0043$ based on Site S60 from Scully et al. (2002). The dashed vertical and horizontal lines show the values that the models use.

this study's model predicts $0.1\,\mathrm{cm\,s^{-1}}$ while the Scully's model predicts $15\,\mathrm{cm\,s^{-1}}$ (the intersection of blue lines). One major difference that two models have is an undefined region where the predicted velocities approach infinity. No velocity beyond this lines is predicted as it is considered the auto-suspension zone where the gravity can initiate the down-slope movement of sediment particles.

6.6 Conclusions

In this chapter, the differences between different studies of wave-supported gravity currents were presented. There are differences between velocity and concentration

profiles in experimental results and field observations. Specifically, there is a large difference between predicted down-slope velocity from different models. There might be several reasons behind these differences. First, an experimental setup cannot have every detail that exists in field conditions. For example, biological processes are missing in the experiments, and the salinity of water is zero so particle interactions are not simulated. The sediment particles that were used in these experiment were similar to that observed in the field but are artificially created, so that clay particles may not have some of the characteristics of natural sediment. The waves in the field are not perfectly symmetrical the way it is in experimental setup. In experimental setting, waves are the only effects that are being considered and the flood effects do not exists which can have huge impacts in the field

Then, there were technical difficulties involved in the wave flume. For example, there was a background concentration due to inlet turbulence in the tank. That background concentration does not exist in the field. Third, the waves are separated from other drivers in our experimental settings while in the field other currents might contribute. Most importantly, Scully et al. (2002) and Wright et al. (2001) models should be used when there is already sediment in suspension due to a prior flood or sediment resuspension. The experimental setting does not consider any prior event and specifically investigates the effects of waves on suspending sediment particles. So there might not be enough supply of sediment in the experimental setting and effects such as hindered settling and consolidation can also makes significant differences Overall, This model is great for exploring wave resuspension mechanisms and details that cannot be evaluated in the field.

Chapter 7

SUMMARY AND OUTLOOK

7.1 Summary

In this dissertation, we investigated the dynamics of Wave-supported Gravity Current (WSGC)—andrea, which are an important process driving cross shelf sediment transport. We made high-resolution measurements of velocity, turbulence and suspended sediment concentration in a wave flume specifically built to simulate WSGC. The experiments were designed to determine how different surface wave forcing conditions alter the sediment transport in the inner continental shelves. There were three principal goals in our experimental program. The first was to investigate the dynamics of WSGC and important turbulence properties in these flows. We conducted experiments with a wide range of wave orbital velocity and period both on a rough wall bed (without sediment) and sediment bed. Comparing rough wall and sediment experiments enables us to tease out the effects of suspended sediment and sediment bed on the flow dynamics. The second goal was to investigate different critical Richardson numbers. We calculated flux, gradient and bulk Richardson numbers with detailed measurements of velocity, turbulence and suspended sediment concentration and formulated these numbers. The third goal was developing an analytical model that predicts down-slope velocity due to WSGC across the shelf. Using an analytical solution to the Navier-Stokes equations, we developed the model and validated it using experimental results.

This dissertation makes several key contributions to our understanding of the Wave-Supported Gravity Currents.

Our experimental results show that the presence of the sediment bed can significantly alter the turbulence structure in WSGC. The turbulent kinetic energy (TKE) increases by more than a factor of three at low wave orbital velocities and is suppressed by density stratification at the highest velocities. In the low velocity regime, the flow is significantly influenced by the formation of ripples, which enhance the TKE and Reynolds stress and increase the wave boundary layer thickness. In the high velocity regime, the ripples are significantly smaller, the near-bed suspended sediment concentrations are significantly higher and density stratification due to suspended sediment concentration becomes important. In this regime, the TKE and Reynolds stress are lower in the sediment bed runs than in comparable runs with no sediment. The transition between regimes appears to result from washout of the ripples and increased concentrations of fine sand suspended in the boundary layer, which increases the settling flux and stratification near the bed.

We present experimental results for bulk, gradient and flux Richardson numbers and propose proper scaling for them. Bulk Richardson numbers with maximum buoyancy frequency in the nominator has a critical value of $\frac{1}{4}$. However, the bulk Richardson number with the average buoyancy frequency in the nominator has a critical value of $Ri_{cr} \approx 0.03$. This value is nearly one order of magnitude smaller than the assumed critical number of $\frac{1}{4}$ from steady tidally driven currents. Scaling bulk Richardson number enables us to close our analytical model for predicting down-slope velocities.

We develop an analytical solution to the Navier-Stokes equations. The solution of the model is provided for laminar and turbulent conditions, and for exponential and

a constant suspended sediment concentration profiles in the mud layer. The model shows very good agreement with experimental results. However, the predicted down-slope velocity suspended and moved by surfaces waves is 1-2 orders of magnitude smaller than that observed in the field correlated with similar wave conditions.

7.2 Outlook

In this dissertation, an analytical model was developed that can be used to predict sediment transport across the shelf due to surface waves. The model works very well for exploring wave resuspension mechanisms and sediment transport in experimental conditions. However, the model should to be verified in the field conditions in the future.

Although the experimental setting was designed very carefully, there were some limitations in the wave flume. For example, there were some effects from the end tanks that brought turbulence to the test section of the tank. In addition, there was a mean flow above the wave boundary layer due to pump work that might have affected the results. Particle interactions were not simulated in the experiments, but are seen in field conditions because clay particles might not have some characteristics of the natural clay in the field. Because of all these reasons, a field work verification seems necessary to validate the model.

The role of particles size in the dynamics of WSGC is significant based on the finding of this dissertation. Detailed experiments in a modified longer wave flume with varied sediment bed will enable us to evaluate the importance of sand fraction in the sediment bed on suspended sediment dynamics in WSGC. In addition, using sediment particles collected from the field with saline water will insure to minimize the difference between laboratory settings and field conditions.

BIBLIOGRAPHY

Absi, R. (2001). Time-dependent eddy viscosity models for wave boundary layers. In *Coastal Engineering Conference*, pages 1268–1281, Sydney. American Sciety of Civil Engineers.

Absi, R. (2004). Discussion of One-Dimensional Wave Bottom Boundary Layer Model Comparison: Specific Eddy Viscosity and Turbulence Closure Models. *Journal of waterway, port, coastal, and ocean*, 130(April):322–325.

Baas, J. H., Best, J. L., Peakall, J., and Wang, M. (2009). A Phase Diagram for Turbulent, Transitional, and Laminar Clay Suspension Flows. *Journal of Sedimentary Research*, 79(4):162–183.

Cacchione, D., Drake, D., and Kayen, R. (1995). Measurements in the bottom boundary layer on the Amazon subaqueous delta. *Marine Geology*, 125(3-4):235–257.

Colney, D. C., Falchetti, S., Lohmann, I. P., and Brocchini, M. (2008). The effects of flow stratification by non-cohesive sediment on transport in high-energy wave-driven flows. *Journal of Fluid Mechanics*, 610:43–67.

Doering, J. and Baryla, A. (2002). An investigation of the velocity field under regular and irregular waves over a sand beach. *Coastal Engineering*, 44(4):275–300.

Downing, J. (2006). Twenty-five years with OBS sensors: The good, the bad, and the ugly. *Continental Shelf Research*, 26(17-18):2299–2318.

Engelund, F. and Zhaohui, W. (1984). Instability of Hyperconcentrated Flow. *Journal of Hydraulic Engineering*, 110(3):219–233.

Falcini, F., Fagherazzi, S., and Jerolmack, D. (2012). Wave-supported sediment gravity flows currents: Effects of fluid-induced pressure gradients and flow width spreading. *Continental Shelf Research*, 33:37–50.

Geyer, W. R., Hill, P., Milligan, T., and Traykovski, P. (2000). The structure of the Eel River plume during floods. *Continental Shelf Research*, 20:2067–2093.

Goring, D. and Nikora, V. (2002). Despiking acoustic Doppler velocimeter data. *Journal of Hydraulic Engineering*, 128(January):117–126.

Grant, W. and Madsen, O. (1986). The continental-shelf bottom boundary layer. *Annual Review of Fluid Mechanics*, 18:265–305.

Grant, W. D. and Madsen, O. S. (1979). Combined wave and current interaction with a rough bed. *Journal of Geophysical Research*, 84(C4):1797–1808.

Grant, W. D. and Madsen, O. S. (1982). Movable bed roughness in unsteady oscillatory flow. *Journal of Geophysical Research*, 87(C1):469.

Hale, R. (2014). *Investigating sediment transport on the Waipaoa margin: linking in situ processes with preserved deposits*. PhD thesis, University of Washington.

Hale, R., a.S. Ogston, Walsh, J., and a.R. Orpin (2014). Sediment transport and event deposition on the Waipaoa River Shelf, New Zealand. *Continental Shelf Research*, pages 1–14.

Hale, R. P. and Ogston, A. S. (2015). In-situ observations of wave-supported fluid-mud generation and deposition on an active continental margin. *Journal of Geophysical Research: Earth Surface*.

Hamblin, A. P. and Walker, R. G. (1979). Storm-dominated shallow marine deposits: the Fernie-Kootenay (Jurassic) transition, southern Rocky Mountains. *Canadian Journal of Earth Sciences*, 16(9):1673–1690.

Hanes, D. M., Alymov, V., and Chang, Y. S. (2001). Wave-formed sand ripples at Duck , North Carolina. *Journal of Geophysical Research: Oceans*, 106(2000):22575–22592.

Hare, J., Hay, A., Zedel, L., and Cheel, R. (2014). Observations of the spacetime structure of flow, turbulence, and stress over orbitalscale ripples. *Journal of Geophysical Research: Oceans*, 119(3):1876–1898.

Hay, A. E., Zedel, L., Cheel, R., and Dillon, J. (2012a). Observations of the vertical structure of turbulent oscillatory boundary layers above fixed roughness using a prototype wideband coherent Doppler profiler: 2. Turbulence and stress. *Journal of Geophysical Research*, 117(C3).

Hay, A. E., Zedel, L., Cheel, R., and Dillon, J. (2012b). On the vertical and temporal structure of flow and stress within the turbulent oscillatory boundary layer above evolving sand ripples. *Continental Shelf Research*, 46:31–49.

Hooshmand, A., Horner-Devine, A. R., and Lamb, M. P. (2015). Structure of turbulence and sediment stratification in wave-supported mud layers. *Journal of Geophysical Research*, 120(4):2430–2448.

Hsu, T. and Jan, C.-D. (1998). Calibration of Businger-Arya type of eddy viscosity model's parameters. *Journal of waterway, port, coastal, and ocean*, 124(5):281–284.

Hsu, T.-J., Ozdemir, C. E., and Traykovski, P. a. (2009). High-resolution numerical modeling of wave-supported gravity-driven mudflows. *Journal of Geophysical Research*, 114(C5):1–15.

Hurther, D. and Lemmin, U. (2001). A correction method for turbulence measurements with a 3D acoustic Doppler velocity profiler. *Journal of Atmospheric and Oceanic Technology*, 18(3):446–458.

Jaramillo, S., Sheremet, a., Allison, M. a., Reed, a. H., and Holland, K. T. (2009). Wavemud interactions over the muddy Atchafalaya subaqueous clinoform, Louisiana, United States: Wavesupported sediment transport. *Journal of Geophysical Research*, 114(C4):C04002.

Kineke, G., Woolfe, K., Kuehl, S., Milliman, J., Dellapenna, T., and Purdon, R. (2000). Sediment export from the Sepik River, Papua New Guinea: evidence for a divergent sediment plume. *Continental Shelf Research*, 20(16):2239–2266.

Kundu, P. K. and Cohen, I. M. (2008). *Fluid Mechanics*. Elsevier Inc., Burlington, MA, fourth edition.

Lamb, M. P., Asaro, E. D., and Parons, J. D. (2004). Turbulent structure of high-density suspensions formed under waves. *Journal of Geophysical Research*, 109(C12):1–14.

Lamb, M. P. and Parsons, J. D. (2005). High-Density Suspensions Formed Under Waves. *Journal of Sedimentary Research*, 75(3):386–397.

Lambrakos, K. F. (1982). Seabed wave boundary layer measurements and analysis. *Journal of Geophysical Research*, 87(C6):4171.

Liang, H., Lamb, M. P., and Parsons, J. D. (2007). Formation of a sandy near-bed transport layer from a fine-grained bed under oscillatory flow. *Journal of Geophysical Research*, 112(C2):C02008.

Ma, Y., Wright, L. D., and Friedrichs, C. T. (2008). Observations of sediment transport on the continental shelf off the mouth of the Waiapu River, New Zealand: Evidence for current-supported gravity flows. *Continental Shelf Research*, 28(4-5):516–532.

McPhee-Shaw, E. E., Siegel, D. a., Washburn, L., Brzezinski, M. a., Jones, J. L., Leydecker, A., and Melack, J. (2007). Mechanisms for nutrient delivery to the inner shelf: Observations from the Santa Barbara Channel. *Limnology and Oceanography*, 52(5):1748–1766.

Milliman, J. and Meade, R. (1983). World-wide delivery of river sediment to the oceans. *The Journal of Geology*, 91(1):1–21.

Mori, N., Asce, M., Suzuki, T., and Kakuno, S. (2007). Noise of Acoustic Doppler Velocimeter Data in Bubbly Flows. *Journal of Engineering Mechanics*, 133(1):122–125.

Myrhaug, D., Lambrakos, K. F., and Slaattelid, O. H. (1992). Wave boundary layer in flow measurements near the seabed. *Coastal Engineering*, 18(1-2):153–181.

Nielsen, P. (1981). Dynamics and geometry of wavegenerated ripples. *Journal of Geophysical Research: Oceans*, 86(C7):6467–6472.

Nielsen, P. (1992). *Coastal Bottom Boundary Layers and Sediment Transport*. Advanced Series on Ocean Engineering.

Nittrouer, C. a. (1999). STRATAFORM: overview of its design and synthesis of its results. *Marine Geology*, 154(1-4):3–12.

Nittrouer, C. A. and Wright, L. D. (1994). Transport of particles across continental shelves. *Reviews of Geophysics*, 32(1):85–113.

O'Donoghue, T., Doucette, J., van der Werf, J., and Ribberink, J. (2006). The dimensions of sand ripples in full-scale oscillatory flows. *Coastal Engineering*, 53(12):997–1012.

Ogston, A., Cacchione, D., Sternberg, R., and Kineke, G. (2000). Observations of storm and river flood-driven sediment transport on the northern California continental shelf. *Continental Shelf Research*, 20(16):2141–2162.

Ogston, A. and Sternberg, R. (1999). Sediment-transport events on the northern California continental shelf. *Marine Geology*, 154(1-4):69–82.

Ozdemir, C. E., Hsu, T.-J., and Balachandar, S. (2010a). A numerical investigation of fine particle laden flow in an oscillatory channel: the role of particle-induced density stratification. *Journal of Fluid Mechanics*, 665:1–45.

Ozdemir, C. E., Hsu, T.-J., and Balachandar, S. (2010b). Simulation of fine sediment transport in oscillatory boundary layer. *Journal of Hydro-environment Research*, 3(4):247–259.

Ozdemir, C. E., Hsu, T.-J., and Balachandar, S. (2011). A numerical investigation

of lutocline dynamics and saturation of fine sediment in the oscillatory boundary layer. *Journal of Geophysical Research*, 116(C9):C09012.

Ozdemir, C. E., Hsu, T.-J., and Balachandar, S. (2014). Direct numerical simulations of transition and turbulence in smooth-walled Stokes boundary layer. *Physics of Fluids*, 26(4):045108.

Parsons, J., Bush, J., and Syvitski, J. (2001). Hyperpycnal plume formation from riverine outflows with small sediment concentrations. *Sedimentology*, 48(2):465–478.

Puig, P., Ogston, A., Mullenbach, B., Nittrouer, C., and Sternberg, R. (2003). Shelf-to-canyon sediment-transport processes on the Eel continental margin (northern California). *Marine Geology*, 193(1-2):129–149.

Puleo, J. and Mouraenko, O. (2003). Wave Bottom Boundary Layer Models for Smooth and Rough Beds. Technical report, DTIC Document.

Roberts, J. and Jepsen, R. (1998). Effects of particle size and bulk density on erosion of quartz particles. *Journal of Hydraulic Engineering*, 124(12):1261–1267.

Ross, M. A. (1988). *Vertical structure of estuarine fine sediment suspensions*. PhD thesis, University of Florida.

Ruessink, B. G., Michallet, H., Abreu, T., Sancho, F., Van der A, D. a., Van der Werf, J. J., and Silva, P. a. (2011). Observations of velocities, sand concentrations, and fluxes under velocity-asymmetric oscillatory flows. *Journal of Geophysical Research*, 116(C3):C03004.

Safak, I., Allison, M., and Sheremet, a. (2013). Floc variability under changing turbulent stresses and sediment availability on a wave energetic muddy shelf. *Continental Shelf Research*, 53:1–10.

Scully, M., Friedrichs, C., and Wright, L. (2002). Application of an analytical model of critically stratified gravity-driven sediment transport and deposition to observations from the Eel River continental shelf, Northern California. *Continental Shelf Research*, 22(14):1951–1974.

Sherwood, C. R., Lacy, J. R., and Voulgaris, G. (2006). Shear velocity estimates on the inner shelf off Grays Harbor, Washington, USA. *Continental Shelf Research*, 26(17-18):1995–2018.

Sleath, J. F. a. (1970). Velocity measurements close to the bed in a wave tank. *Journal of Fluid Mechanics*, 42(01):111.

Sternberg, R. and Cacchione, D. (1996). Observations of sediment transport on the Amazon subaqueous delta. *Continental Shelf Research*, 16(5):697–715.

Thorne, P., Williams, J., and Davies, A. (2002). Suspended sediments under waves measured in a large-scale flume facility. *Journal of Geophysical Research*, 107(C8).

Thorne, P. D., Davies, A. G., and Bell, P. S. (2009). Observations and analysis of sediment diffusivity profiles over sandy rippled beds under waves. *Journal of Geophysical Research*, 114(C2):C02023.

Traykovski, P., Geyer, W., Irish, J., and Lynch, J. (2000). The role of wave-induced density-driven fluid mud flows for cross-shelf transport on the Eel River continental shelf. *Continental Shelf Research*, 20(16):2113–2140.

Traykovski, P., Wiberg, P., and Geyer, W. (2007). Observations and modeling of wave-supported sediment gravity flows on the Po prodelta and comparison to prior observations from the Eel shelf. *Continental Shelf Research*, 27(3-4):375–399.

Trowbridge, J. H. and Kineke, G. C. (1994). Structure and dynamics of fluid muds on the Amazon. *Journal of Geophysical Research*, 99(C1):865–874.

Turner, J. (1973). *Buoyancy effects in fluids*. Cambridge University Press, New York.

van Kessel, T. and Kranenburg, C. (1996). Gravity current of fluid mud on sloping bed. *Journal of Hydraulic Engineering*, 122:710–717.

Van Rijn, L. (1993). *Principles of sediment transport in rivers, estuaries and coastal seas*. Aqua Publications, Amsterdam.

Van Rijn, L. (2007). Unified view of sediment transport by currents and waves. II: Suspended transport. *Journal of Hydraulic Engineering*, 133(6):668–689.

Vongvisessomjai, S. (1984). Oscillatory Ripple Geometry. *Journal of Hydraulic Engineering*, 110(3):247–266.

Walsh, J., Nittrouer, C., Palinkas, C., a.S. Ogston, Sternberg, R., and Brunskill, G. (2004). Clinoform mechanics in the Gulf of Papua, New Guinea. *Continental Shelf Research*, 24(19):2487–2510.

Wheatcroft, R. A., Stevens, A. W., and Johnson, R. V. (2007). In situ time-series measurements of subseafloor sediment properties. *Oceanic Engineering, IEEE Journal of*, 32(4):862–871.

Wiberg, P. and Smith, J. D. (1983). A comparison of field data and theoretical models for wave-current interactions at the bed on the continental shelf. *Continental Shelf Research*, 2(2-3):147–162.

Wiberg, P. L. and Harris, C. K. (1994). Ripple geometry in wave-dominated environments. *Journal of Geophysical Research*, 99(C1):775.

Winterwerp, J. (2002). On the flocculation and settling velocity of estuarine mud. *Continental shelf research*, 22(October 2001):1339–1360.

Winterwerp, J. C. (2006). Stratification effects by fine suspended sediment at low, medium, and very high concentrations. *Journal of Geophysical Research*, 111(C5):C05012.

Wright, L. and Friedrichs, C. (2006). Gravity-driven sediment transport on continental shelves: A status report. *Continental Shelf Research*, 26(17-18):2092–2107.

Wright, L., Friedrichs, C., Kim, S., and Scully, M. (2001). Effects of ambient currents and waves on gravity-driven sediment transport on continental shelves. *Marine Geology*, 175(1-4):25–45.

Wright, L., Kim, S.-C., and Friedrichs, C. (1999). Across-shelf variations in bed roughness, bed stress and sediment suspension on the northern California shelf. *Marine Geology*, 154(1-4):99–115.

Wright, L., Sherwood, C., and Sternberg, R. (1997). Field measurements of fair-weather bottom boundary layer processes and sediment suspension on the Louisiana inner continental shelf. *Marine Geology*, 140(3):329–345.

Yan, B., Zhang, Q., and Lamb, M. (2010). Time-Averaged Turbulent Mixing and Vertical Concentration Distribution of High-Density Suspensions Formed Under Waves. *Coastal Engineering*, 32:1–8.